

DISS. ETH NO. 22339

**FULLY INTEGRATED CMOS MICROELECTRODE ARRAY
FOR ELECTROCHEMICAL MEASUREMENTS**

A thesis submitted to attain the degree of

DOCTOR OF SCIENCES of ETH ZURICH

(Dr. sc. ETH Zurich)

presented by

JÖRG ROTHE

Master of Science ETH in Electrical Engineering and Information Technology

born on 07.09.1978

citizen of Altbüren, LU, Switzerland

accepted on the recommendation of

Prof. Dr. Andreas Hierlemann, examiner

Prof. Dr. Roland Thewes, co-examiner

Dr. Olivier Frey, co-examiner

2014

ABSTRACT

This thesis reports on the design and application of a fully integrated complementary-metal-oxide semiconductor (CMOS) microelectrode array (MEA) for performing electroanalytical methods on a large number of electrodes.

Microelectrodes have been widely used to electrochemically monitor concentrations of chemical species. Using arrays of microelectrodes allows for highly parallel measurements to acquire redundant measurements for improved statistics, or for functionalizing electrodes in different ways in order to make various and complementary measurements of a single sample.

Several advantages arise from combining MEAs and CMOS technology: Large sensing areas with high spatial resolution can be realized, as the problem of routing of a large number of electrodes is overcome by the many metal layers that standard CMOS process technology offers. By using electronic switches, even more electrodes can be accessed and read out by means of multiplexing techniques. The integration of analog-to-digital converters (ADCs) on the same substrate with the electrodes, enables robust data transmission by reducing the parasitic effects of off-chip connections and the electromagnetic interference, both of which degrade signal quality. Moreover, the number of pins can be significantly reduced, since the signals can be read out by time-division multiplexing.

The chip presented in this thesis features a large sensing area of $3.2\text{ mm} \times 3.2\text{ mm}$, including 1024 electrodes placed at a center-to-center pitch of $100\text{ }\mu\text{m}$. The platinum sensing electrodes of the array are realized in diameters of 5 to $50\text{ }\mu\text{m}$. An analog switch matrix is used to connect the 64 available current readout units to a selectable subset of electrodes. The 64 current readout units can cover a range of $10\text{ }\mu\text{A}$ down to 100 pA . The current is digitized by sigma-delta converters at a maximum resolution of 13.3 bits (effective, for a bandwidth of 1 kHz and a full-scale range of $1\text{ }\mu\text{A}$). The integrated noise is 220 fA for a bandwidth of 100 Hz, allowing for detection of pA currents. Currents can be continuously acquired at up to 1 kHz bandwidth, or the whole array can be read out rapidly at a frame rate of up to 90 Hz. All analog reference signals are generated on the chip by nine 10-bit digital-to-analog converters (DACs).

The resulting system meets the requirements of a wide range of electrochemical methods including amperometric images, voltammetric measurements, cyclic voltammetry, square wave voltammetry and differential pulse voltammetry and the use of galvanostatic methods. Bi-potentiostatic or multi-potentiostatic (4 potential levels plus reference electrode) measurements can be performed by simultaneously applying different potentials to different sets of working electrodes.

Packaging methods were developed for protecting the electronic circuits against the liquid environment.

A robust functionalization method was developed, which uses voltage-pulse based electrode-

position to allow for uniform and reproducible layer deposition that is suitable for large electrode arrays.

The system potential to monitor concentrations of biologically relevant species involved in signaling, such as neurotransmitters and neuromodulators, and molecules involved in cell metabolism is demonstrated. The measurement system has been used to measure analyte concentrations from all electrodes of the array at high spatial and temporal resolution.

ZUSAMMENFASSUNG

Diese Dissertation beschreibt das Design und die Anwendung eines voll integrierten complementary metal-oxide-semiconductor (CMOS) Mikroelektrodenarrays (MEA) um elektroanalytische Methoden auf einer grossen Anzahl an Elektroden gleichzeitig durchführen zu können. Mikroelektroden sind weit verbreitet, um Konzentrationen von chemischen Substanzen mittels elektrochemischer Techniken zu messen. Elektrodenarrays ermöglichen es, gleichzeitige Messung an vielen Punkten, zum Beispiel vieler Zellen einer Zellkultur durchzuführen. Redundante Messungen von Elektrodenarrays erlauben es, verbesserte statistische Daten zu erheben. Mit unterschiedlich funktionalisierten Elektroden eines Arrays können verschiedene oder komplementäre Daten von einzelnen Proben gemessen werden. Durch die Kombination von MEAs und CMOS Technologie entstehen mehrere Vorteile: Flächen mit einer hohen Dichte an Messpunkten werden durch die vielen Metallisierungsschichten eines Standard-CMOS Prozesses ermöglicht. Mittels elektronischer Schalter können viele Elektroden durch Multiplexing ausgelesen werden. Die Integration von Analog-Digital-Wandlern (ADCs) mit Sensorelektroden erlaubt eine robuste Datenübertragung: parasitäre Effekte der Chip-Kontaktierung und elektromagnetische Störungen, welche die Signalqualität verschlechtern können, werden vermindert. Ausserdem kann die Anzahl der benötigten Kontakte zum Chip mittels Zeitmultiplexverfahren stark verringert werden. Der Chip, welcher in dieser Dissertation präsentiert wird, besitzt eine Array-Fläche von $3.2 \text{ mm} \times 3.2 \text{ mm}$, auf welcher 1024 Elektroden im Abstand von $100 \text{ }\mu\text{m}$ platziert sind. Die Platinelektroden haben einen Durchmesser von 5 bis $50 \text{ }\mu\text{m}$. Eine analoge Schaltmatrix erlaubt es, die Strommessschaltungen mit ausgewählten Elektroden zu verbinden. Die 64 Strommessschaltungen verschiedene Messbereiche zwischen $10 \text{ }\mu\text{A}$ und 100 pA abdecken. Sigma-Delta Modulatoren digitalisieren die Ströme mit einer maximalen Auflösung von 13.3 Bit (effektiv, bei einer Bandbreite von 1 kHz und im Messbereich von $1 \text{ }\mu\text{A}$). Das integrierte Rauschen beträgt in einer Bandbreite von 100 Hz 220 fA , was es ermöglicht Ströme im pA -Bereich zu messen. Ströme können entweder kontinuierlich mit bis zu 1 kHz Bandbreite erfasst werden oder Ströme von allen Elektroden des Arrays können mit einer Rate von 90 Hz ausgelesen werden. Alle analogen Signale werden mittels neun 10-bit Digital-Analog-Wandlern auf dem Chip generiert.

Das resultierende System erfüllt die Anforderungen einer Reihe elektrochemischer Methoden, wie z.B. amperometrische und voltametrische Messungen, Cyklovoltammetrie, Rechteckvoltammetrie und differentielle Puls-Voltammetrie, sowie galvanostatische Methoden. Bipotentiotatische und mehr-potentiostatische (4 Spannungslevel sowie die der Referenzelektrode) können durchgeführt werden, indem gleichzeitig mehrere Elektroden mit unterschiedlichen Potentialen versorgt werden.

Techniken zum Verpacken des Chips wurden entwickelt um die elektronischen Schaltungen gegen die flüssigen Substanzen zu schützen.

Eine zuverlässige Elektrodenfunktionalisierung wurde entwickelt, welche, auf Basis von Spannungspulsen mittels elektrochemischer Abscheidung gleichmässige und reproduzierbare Schichten auf den Elektroden grosser Arrays ermöglicht.

Die Möglichkeit Konzentrationen biologisch wichtiger Stoffe zu überwachen, welche an der Signalübertragung (z.B. Neurotransmitter oder Neuromodulatoren) oder welche am Metabolismus einer Zelle beteiligt sind, wird gezeigt. Schliesslich wird das Messsystem verwendet, um Konzentrationen eines chemischen Stoffes mit hoher örtlicher und zeitlicher Auflösung auf dem gesamten Array zu erfassen.

CONTENTS

1	INTRODUCTION	1
1.1	Electroanalytical methods	1
1.2	Biosensors	2
1.3	Microelectrode arrays for electroanalytical methods	3
1.4	Integrated CMOS sensors	3
1.5	Scope of the thesis	4
1.6	Structure of the thesis	5
1.7	Major results	6
2	ELECTROCHEMICAL BASICS AND REQUIREMENTS	9
2.1	Electrodes in an electrolyte	9
2.2	Electrode Potentials	9
2.2.1	The metal-ion electrode	10
2.2.2	The redox electrode	10
2.2.3	The reference electrode	11
2.2.4	The electrode-electrolyte interface	11
2.2.5	Equivalent circuit	12
2.3	Electrodes and current	13
2.3.1	Electrochemical instrumentation	13
2.3.2	Voltage-current relation	14
2.3.3	Diffusion limited currents	15
2.3.4	Diffusion at microelectrode arrays	16
2.3.5	Faradaic currents expected at microelectrodes	17
2.3.6	Equivalent circuit	17
2.4	Summary	18
3	CIRCUIT DESIGN	21
3.1	Array of working electrodes	21
3.1.1	Parameters	21
3.1.2	Considerations	21
3.1.3	Realization	22
3.1.4	Discussion	22
3.2	The potentiostat	22
3.2.1	Parameters	22
3.2.2	Considerations	22
3.2.3	Realization	24

Contents

3.2.4	Discussion	25
3.3	Current readout	26
3.3.1	Parameters	26
3.3.2	Considerations	26
3.3.3	Realization	27
3.3.4	Discussion	32
4	SYSTEM DESCRIPTION AND CHARACTERIZATION	35
4.1	CMOS chip	36
4.1.1	Switching matrix	36
4.1.2	Master potentiostat	38
4.1.3	Current readout	39
4.1.4	Auxiliary circuit blocks	41
4.1.5	Digital interface	42
4.1.6	Full frame readout	42
4.1.7	Power consumption	42
4.1.8	Discussion	43
4.2	FPGA and circuit board	45
4.2.1	Decimation filters	46
4.2.2	Real-time engine	47
4.2.3	Data communication	48
4.2.4	Discussion	48
4.3	Software	48
5	MICROFABRICATION AND PACKAGING SOLUTIONS	51
5.1	Electrodes for electrochemistry	52
5.1.1	Counter and reference electrodes	52
5.1.2	The array of working electrodes	53
5.1.3	Electrode fabrication	55
5.2	Packaging solutions	55
5.2.1	Package variations	56
5.2.2	Packaging procedure	56
5.3	Microfabrication	58
5.4	Discussion	58
6	ELECTROCHEMICAL TECHNIQUES AND CHARACTERIZATION	61
6.1	Electroanalytical techniques	61
6.1.1	Amperometry	61
6.1.2	Cyclic voltammetry	62
6.1.3	Pulse voltammetry	63
6.1.4	Galvanostatic methods	66
6.1.5	Bipotentiostat	66

6.2	Electrochemical characteristics of the microelectrodes	66
6.2.1	Redox couple	67
6.2.2	Surface properties	68
6.3	Circuit implementations and electrochemistry	69
6.3.1	Comparison of the current readout circuits	69
6.3.2	Polarization of electrodes - multiplexing effects	71
6.4	Discussion	72
7	ELECTRODE FUNCTIONALIZATION	73
7.1	Drop coating	74
7.2	Electrochemically aided adsorption	74
7.3	Electrodeposition	75
7.3.1	Voltage-pulse based deposition scheme	76
7.3.2	Pt black	77
7.3.3	Gold	79
7.3.4	Conducting polymers	81
7.3.5	Non-conducting polymers	82
7.4	Discussion	84
8	MEASUREMENTS OF BIOLOGICALLY RELEVANT SPECIES	87
8.1	Neurotransmitters	87
8.1.1	Dopamine	87
8.1.2	Choline	89
8.2	Metabolites	91
8.2.1	Glucose	91
8.2.2	Lactate	92
8.3	Electrochemical images	94
8.3.1	Hydrogen peroxide	94
8.3.2	Specific functionalization to detect glucose	97
8.3.3	Monitoring glucose on the whole array	99
8.4	Discussion	99
9	CONCLUSION	103
9.1	Considerations for improvements	104
9.2	Outlook	105
	BIBLIOGRAPHY	107

1

INTRODUCTION

Cells constantly exchange molecules with the extra-cellular environment. Metabolites are taken up, converted, and the byproducts released into the environment. Cell signaling is used to remote-control cell activity. The endocrine system in organisms releases hormones into the circulatory system to regulate the metabolism of other cells. Neuromodulators, neurotransmitters that diffuse over large areas in the nervous system, modulate the response of multiple neurons.

Detecting molecules in the extra-cellular space and measuring their concentrations is of paramount interest: (i) Differences in the metabolism of cells can be used to differentiate healthy cells from cancer cells. (ii) Malfunctions in cell signaling are involved in many diseases, i.e. diabetes. (iv) Inflammatory markers can help to diagnose diseases. (v) Concentration changes of neurotransmitters are very important for understanding the function of the nervous system and the link to various neurological diseases, such as epilepsy, Alzheimer's and Parkinson's. (vi) Finally, the extra-cellular molecular environment can help to unravel different cell functions.

Cells are individuals and even in a monoclonal cell culture, differences between individual cells can be seen. Organs consist of different cell types, having different functions and a different molecular "footprint".

Ideally, one would want to monitor the analyte of interest from individual cells in a massively parallel manner at high spatial resolution and in real-time.

A different, but nevertheless equally large field of applications is found in diagnostics. Microarrays and immunoassays are the gold standard in laboratories utilized for expression profiling, to detect diseases and to test drug efficacy. The sample is tested against numerous probes in parallel via fluorescence and optical detection. If instead of optical measurements electrical measurements could be employed to realize the detection, the measurement device could be miniaturized, and the sensors could be rendered cheap and disposable. The availability of such sensor systems could open routes to personal diagnostics and point-of-care applications.

1.1 ELECTROANALYTICAL METHODS

Electrochemistry offers methods to detect and monitor concentration variations of a plethora of analytes. Especially concentrations of electroactive molecules can be measured directly through faradaic currents by using amperometry or voltammetry (Bakker 2004). Electro-

1 INTRODUCTION

chemical methods are widely used to investigate signaling in the brain (Robinson et al. 2008), to measure many different kinds of molecules involved in the metabolism of biological cells (Yotter and Wilson 2004), to detect selected sequences of DNA (Sassolas et al. 2008), and to perform diagnostics by detection of DNA (Wang 2006), or are employed with immunoassays (Warsinke et al. 2000).

Various electrochemical techniques have been developed to increase selectivity or sensitivity to a specific analyte. Electrochemical sensor systems have prevalingly advanced in two directions in the past years: (i) modification of the electrodes to detect non-electroactive molecules, and (ii) miniaturization and parallelization of electrodes and readout schemes.

1.2 BIOSENSORS

Many biologically relevant molecules are non-electroactive so that the sensing electrodes have to be modified by using, e.g., enzymes that produce electroactive species from originally uncharged biomolecules. The bio-sensitive elements usually feature a high selectivity to recognize a specific analyte (Ronkainen et al. 2010).

Since the fabrication of the first glucose sensor from Clark and C. Lyons (1962), the tendency in electrochemical biosensors was to create devices, which are smaller, faster, more integrated, and which can perform a larger number of functions in parallel (Reddy et al. 1994). While the sensing/recognition, which is almost exclusively based on biological affinity, has not changed much since then, the transduction and signal processing and, of course, the sensors themselves have evolved dramatically (Ronkainen et al. 2010). Large-diameter electrodes have evolved into 1 – 100 μm or even submicron-sized electrodes, custom-fabricated sensor interfaces have grown into fully integrated measuring systems, and the capabilities of these systems have become more sophisticated going from current and/or voltage readings to three-electrode electrochemical measurements.

The first obvious features of these miniaturized sensors are the much smaller electrodes, resulting in smaller volumes that can be investigated. Microelectrode behavior has been studied more systematically in the last years revealing useful effects: a decreased ohmic drop in the electrolyte, a high current density accompanying small measured current, and rapid establishment of a steady-state potential, as compared to macroelectrodes (Heinze 1993). Clearly, there is a large number of potential applications for micron-scale electrochemical biosensors in biology and medicine (Vo-Dinh and Cullum 2000; Bashir 2004). Prominent examples include measuring neurotransmitter levels in the brain (Robinson et al. 2008; Heien et al. 2004; Hochstetler et al. 2000), monitoring secretion of single cells (Wightman 2006; Ino et al. 2014; Amatore et al. 2008; Liu et al. 2011; Zhang et al. 2008; Picollo et al. 2013; Kisler et al. 2012), detection of DNA strands (Drummond et al. 2003; Wang 2002; Kalantari et al. 2010), or immunoassays (Warsinke et al. 2000).

1.3 MICROELECTRODE ARRAYS FOR ELECTROANALYTICAL METHODS

The real advantages and opportunities of microelectrodes can be exploited by incorporating them into arrays. Arrays can be configured into planar or needle arrays for *in vitro* or *in vivo* studies (Harrison et al. 2007; Herwik et al. 2009; Wise et al. 2004). They offer the advantage of many identically processed/fabricated sensors that can be read out simultaneously or sequentially. These can provide redundant measurements for improved statistics, or they can be functionalized in different ways in order to make variable and complementary measurements on a single sample. As aforementioned for single microelectrodes, arrays can be made very compact so that only small reagent volumes are needed, which enables the investigation of small structures.

Miniaturization and parallelization are mainly enabled by advancements in microtechnology. Sensors can be scaled down to the size of single cells and smaller. Besides a better spatial resolution, the temporal resolution is also improved due to the smaller time constants in miniaturized systems.

However, miniaturization and parallelization entail design challenges for devising sensors for bio-measurements: (i) When sensors are miniaturized, the background currents due to charging and discharging of the electrode-electrolyte interface are reduced, however, the signal levels are lower as well. Thus, acquisition electronics have to be designed to resolve the small signals and to handle the large capacitances. (ii) Parallelization requires a very compact connection scheme, to provide access to all sensors, without reducing the available sensor area.

1.4 INTEGRATED CMOS SENSORS

Fabricating the electrodes on glass or polymer substrates and using external equipment for readout is possible and sometimes adequate (Fritz et al. 2002; Dharuman et al. 2005). Due to the small signals involved, however, and the required sensitivity of the measurements, it becomes beneficial or even necessary to use integrated complementary-metal-oxide semiconductor (CMOS) electronics close to the signal source (Joo and Brown 2008). Moreover, thousands of electrodes can be arranged within a few square millimeters, and the signals can be digitized on chip so that the signal fidelity is preserved and a superior signal-to-noise ratio is maintained.

For larger arrays, it is not feasible to directly connect external readout electronics or a separate chip to the individual electrodes through wiring.

By integrating microtechnology with CMOS circuits one can efficiently address this issue: (1) sensors and readout circuits can be integrated in a compact device, (2) arrays with a lot of electrodes can be realized through integration of addressing schemes, (3) many devices can be fabricated in parallel on wafer level, (4) lengthy signal paths and resulting noise interference can be avoided, as the signals are amplified and digitized right at the source, and the signal fidelity is preserved. The increased immunity to noise allows for using the devices

1 INTRODUCTION

in experiments without additional shielding and without Faraday cages.

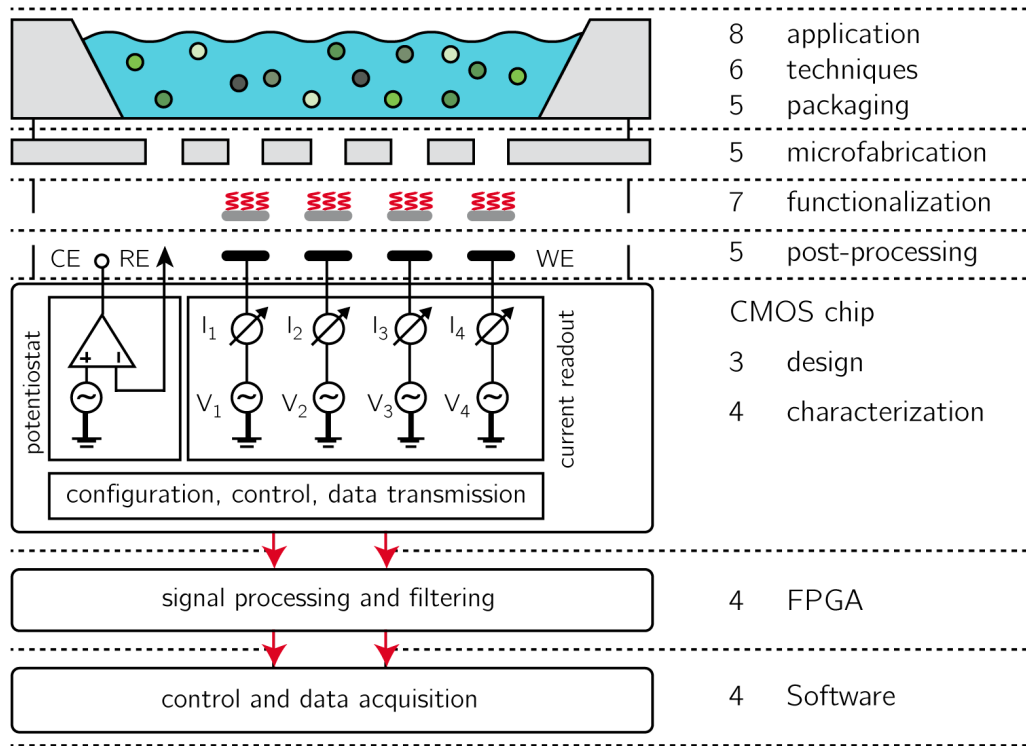
These benefits come along with several challenges: High frame rates for arrays require rapid acquisition and processing of the currents from all electrodes; the sensor front-end, the analog-to-digital converter (ADC), and the data transmission chain need to be synchronized and need to provide enough signal bandwidth. Metal pads of the standard CMOS process are made of non-noble metals, like copper and aluminum, which are neither compatible with biological applications nor usable for electrochemical methods. Custom post-processing steps are required to produce, e.g., stable gold or platinum electrodes.

The devices have to be placed in a long-term-biocompatible package to protect the electronics against the harsh biological and chemical liquid environment. Finally, a measurement system is required, which can perform the signal processing, handle the data transmission, control the CMOS device and record and analyze the acquired data.

1.5 SCOPE OF THE THESIS

This thesis describes the design of an integrated CMOS chip, which can perform various electroanalytical methods on an integrated microelectrode array of 1024 platinum electrodes. The primary application of the CMOS chip is to measure different analytes in the extracellular space secreted from cells using electroanalytical techniques. The cells can be individual cells in suspension, cell cultures grown on the chip, or tissue slices placed atop the chip. The target analytes are molecules involved in signaling, like neurotransmitters and neuromodulators, and molecules involved in the metabolism of cells. The CMOS chip is intended to acquire the concentrations of these analytes from the whole array multiple times per second. The spatial resolution (i.e. the number of electrode and their pitch) should be high enough to make a map of concentrations across the cell culture. There are a number of different electroanalytical techniques, which are advantageous for different scenarios. The specifications of the measurement system, e.g., the bandwidth, measurement range and the necessary controls, have to enable these techniques. Furthermore, the circuitry used for operation and readout is supposed to also enable the functionalization of the sensing electrodes. To reduce influences by external noise sources, the currents are digitized near the signal source. For the same reason circuits are provided to generate analog signals near the location where they are needed, i.e. on the CMOS chip.

1.6 STRUCTURE OF THE THESIS



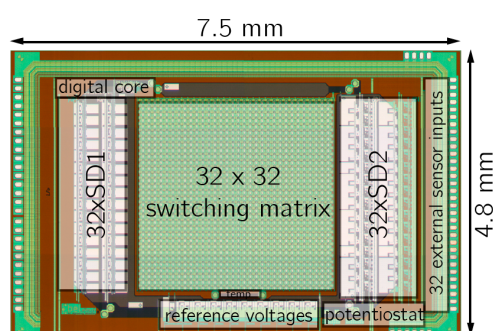
The figure above is used to illustrate the structure of the thesis: The chapter numbers are given at the right as they relate to the different components of the developed measurement system.

To explain design decisions and certain effects in the experiments Chapter 2 starts with electrochemical basics. The integrated circuits designed to realize the system are described in Chapter 3. The description of the complete system together with electrical characterizations is included in Chapter 4. Chapter 5 explains the design and fabrication process of the sensing array, the different solutions to packaging and the usage of microfabrication to add wells to the array. The measurement techniques, which can be realized by the system are demonstrated in Chapter 6. Surface modifications to improve certain characteristics of the electrodes or to make the system a biosensor array are explained in Chapter 7. Measurement results for different applications are shown in Chapter 8. Finally the thesis ends with conclusions and considerations for future improvements.

Parts of this thesis were published in Rothe, Lewandowska, et al. (2011), Rothe et al. (2012), Rothe et al. (2014), and Rothe, Madangopal, et al. (2014).

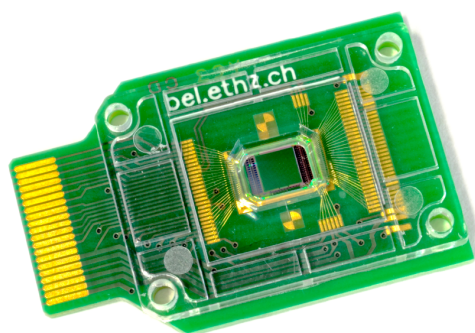
1 INTRODUCTION

1.7 MAJOR RESULTS



A **fully integrated CMOS chip** for performing electroanalytical measurements was designed. The chip features an array of 32x32 platinum electrodes. 64 analog-to-digital converters, a master potentiostat, and 9 digital-to-analog converters are implemented on the chip. Currents in the range from 10 μA down to pA can be measured. The current is digitized by sigma-delta converters at a maximum resolution of 13.3 bits (effective, for a bandwidth of 1 kHz and a full-scale range of 1 μA). The integrated

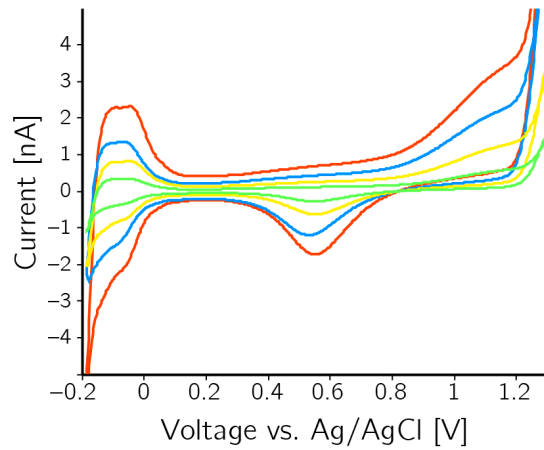
noise is 220 fA for a bandwidth of 100 Hz, allowing for detection of pA currents. Currents can be continuously acquired at up to 1 kHz bandwidth, or the whole array can be read out rapidly at a frame rate of up to 90 Hz.



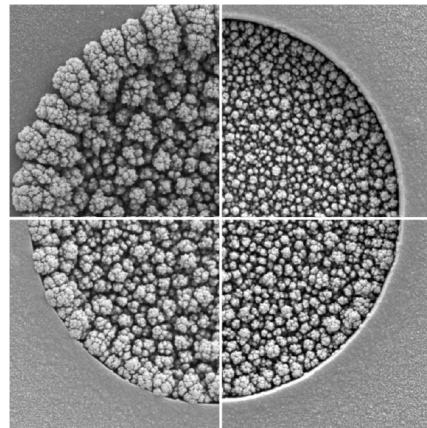
Packaging options have been evaluated, and finally, a robust and efficient **packaging method** has been found. The electronics are protected by a biocompatible injection-molded polycarbonate package, and various accessories can be attached to the assembly, i.e., to provide a perfusion system for the cells or additional sample volume.

1.7 Major results

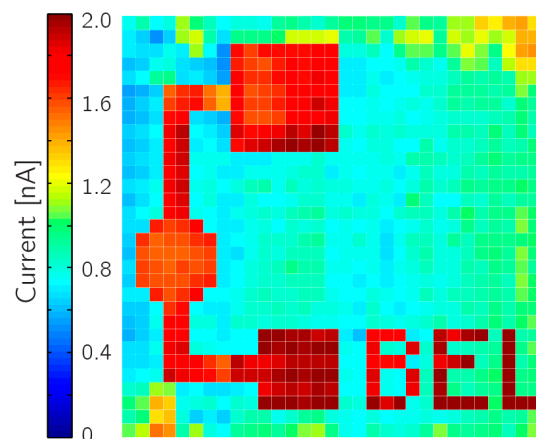
A broad variety of **measurements** are demonstrated with the very same system, including amperometry, voltammetric measurements, cyclic voltammetry, square wave voltammetry or differential pulse voltammetry as well as galvanostatic methods.



A new **functionalization method** has been developed, which allows for deposition of various materials (i.e. metals, polymers) on large microelectrode arrays. The method reliably produces uniform and predictable modifications of the electrode surface. Surface properties can be tuned by modifying the protocol parameters. The method scales very well and can be adapted to new materials.



The measurement system can be used to acquire **amperometric electrochemical images** at a frame rate of up to 90 frames per second. Measurements demonstrate the capabilities of measuring concentrations of metabolites (lactate, glucose), as well as neurotransmitters (i.e. dopamine and (acetyl-)choline).



2

ELECTROCHEMICAL BASICS AND REQUIREMENTS

This chapter will explain basic electrochemical concepts, which are relevant for determining specifications for the circuit design, the electrode layout, and to explain some analytical electrochemical techniques. More explanations and details can be found in the standard textbooks (Hamann et al. 2007; Bockris et al. 2000; Bard and Faulkner 2001).

2.1 ELECTRODES IN AN ELECTROLYTE

The chemical potential of an ion in an electrolyte depends on the chemical environment and the electrostatic field. The so-called electrochemical potential $\bar{\mu}_i$ of species i is given in in J/mol and can be described as:

$$\bar{\mu}_i = \mu_i + z_i F \phi = \mu_i^* + RT \ln a_i + z_i F \phi \quad (2.1)$$

μ_i is the chemical potential, z_i is the valency (charge) of the ion i , F is the Faraday constant ($96485 C/mol$), ϕ is the local electrostatic potential, R the universal gas constant ($8.3145 J/(molK)$) and T the absolute temperature. The chemical potential can be split into a sum of μ_i^* the chemical potential of species i at unit activity, and the deviation from this potential due to activity a_i . When two phases are brought in contact, the electrochemical potentials across the phase boundary of phases I and II have to equilibrate:

$$\sum_i \bar{\mu}_i(I) = \sum_j \bar{\mu}_j(II) \quad (2.2)$$

When an electrode is immersed into an electrolyte this equilibrium is achieved by movement of charges (ions resp. electrons). There are several mechanisms, which can contribute to equilibrating the electrochemical potential: (i) a metal can be dissolved (by oxidation) or deposited (by reduction). (ii) A redox pair from solution can change the ratio of reduced vs. oxidized species. (iii) The orientation of dipoles can generate a net charge at the phase boundary. (iv) Charge can be supplied externally, e.g., by applying a voltage.

2.2 ELECTRODE POTENTIALS

The so-called electromotoric force can be calculated through applying Equation 2.2. The resulting equation is termed the Nernst equation. The Nernst equation can be formally set

2 ELECTROCHEMICAL BASICS AND REQUIREMENTS

up only if the entities that are responsible for the charge transfer are known. Two important examples are (a) a metal electrode in a solution of its ions and (b) an inert electrode with a redox couple in solution.

2.2.1 The metal-ion electrode

A metal electrode in contact with a solution of its ions will be dissolved, or metal will be deposited to reach electrochemical equilibrium. The reaction can be written as $\text{Me} \rightleftharpoons \text{Me}^{z+} + ze^-$. The reactions will charge up the phase boundary and continue until the electrostatic forces prohibit further reactions. Equation 2.2 will look like:

$$\mu_{\text{Me}}^* + RT \ln a_{\text{Me}} + zF\phi_{\text{Me}} = \mu_{\text{Me}^{z+}}^* + RT \ln a_{\text{Me}^{z+}} + zF\phi_L \quad (2.3)$$

The difference of the potentials in the metal phase ϕ_{Me} and in the liquid phase ϕ_L is:

$$E = \phi_{\text{Me}} - \phi_L = \frac{\mu_{\text{Me}^{z+}}^* - \mu_{\text{Me}}^*}{zF} + RT \ln \frac{a_{\text{Me}^{z+}}}{a_{\text{Me}}} \quad (2.4)$$

The activity in the metal is $a_{\text{Me}} = 1$ and therefore can be discarded.

The potential difference under standard conditions (i.e. $a_{\text{Me}} = a_{\text{Me}^{z+}} = 1$) is the standard electrode potential:

$$E_0 = \frac{\mu_{\text{Me}^{z+}}^* - \mu_{\text{Me}}^*}{zF} \quad (2.5)$$

The values of E_0 are tabulated for different chemical species and their reactions. Since one cannot determine absolute potentials, the standard electrode potentials are tabulated, by convention, with respect to the standard hydrogen electrode (SHE).

The values of E_0 can be used to give an idea, which reactions may happen in an electrochemical cell. Equation 2.4 and 2.5 can be used to obtain an equation for a metal electrode in a solution of its ion:

$$E = E_0 + \frac{RT}{zF} \ln a_{\text{Me}^{z+}} \quad (2.6)$$

The activity $a_{\text{Me}^{z+}}$ is the activity of the metal ions in the solution. The standard electrode potentials are dependent on temperature and concentrations.

2.2.2 The redox electrode

Upon immersion of an inert electrode (i.e. a platinum electrode) into a solution containing a redox couple (i.e. $\text{Fe}_2^+ \rightleftharpoons \text{Fe}_3^+ + e^-$) redox reactions across the phase boundary are leading to an electrochemical equilibrium as it has been the case for the metal electrode. As before Equation 2.6 can be rewritten:

$$E = E_0 + \frac{RT}{zF} \ln \frac{a_{\text{ox}}}{a_{\text{red}}} \quad (2.7)$$

z is the number of electrons which is exchanged due to the reaction. a_{ox} is the activity of the oxidized, a_{red} the activity of the reduced species. It is interesting to notice that the relation between the concentration of a species and the measured potentials is logarithmic. Potentiometry is the measurement of potential changes upon changes in ion concentrations (i.e. ion selective electrodes, pH measurements).

Redox pairs that can easily transit from oxidized to reduced state or vice versa are commonly used for testing and characterizing an electrochemical cell (see Section 6.1.3) or as electrochemical labels (i.e. ferrocene) to allow for sensing of non-electroactive molecules (Drummond et al. 2003; Odenthal and Gooding 2007).

2.2.3 The reference electrode

To measure the potential of an electrode under test, or a working electrode (WE), a second electrode is required to connect with the electrolyte. The second electrode itself develops an electrochemical potential upon immersion in solution, which is then included in the measured overall potential difference. A solution to that dilemma is to use reference electrodes with defined electrochemical potential, such as the silver/silver chloride (Ag/AgCl) or Kalomel electrode. The open circuit potential (OCP) of an electrochemical cell can then be assessed with respect to the type of reference electrode used.

Commonly used reference electrodes (REs) (e.g. Ag/AgCl/KCl 3M) are electrodes of the second kind. They consist of a metal electrode, where the activity of the metal ions in solution is in equilibrium with a second solid phase of a sparsely soluble salt of the metal (i.e. AgCl), the solubility product of which is constant. The RE is separated from the electrochemical cell via a glass frit, which allows charge carrier transfer with minimal leakage. With the help of such a reference electrode, a certain potential (voltage) can be applied to an electrode under test and the electrolyte, under the condition that no net current flows through the reference electrode. Controlling the potential is crucial for applying electroanalytical methods, since the measured current strongly depends on the applied voltage (see below).

2.2.4 The electrode-electrolyte interface

Figure 2.1 shows a possible distribution of charge carriers at an electrode-electrolyte interface. We consider again the situation of a metal ion electrode in solution: if the chemical potential of the metal is smaller than that of the metal ions in solution ($\mu_{Me} < \mu_{Me^{z+}}$), then metal ions (cations) from solution will be deposited on the electrode by taking up electrons from the metal electrode. The electrode charges up positively and anions will be pulled towards the electrode surface (see Figure 2.1 a left panel). The electric field stops further reduction processes and deposition of metal.

In the opposite case ($\mu_{Me} > \mu_{Me^{z+}}$) metal will be dissolved and positive ions will be released into the solution. The electrode charges up negatively and cations are pulled to the interface

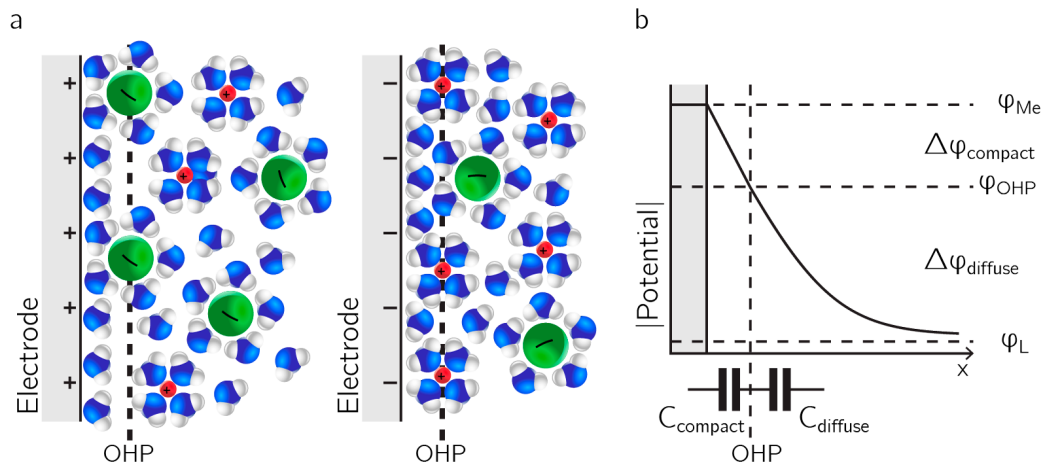


Figure 2.1: Electrode in electrolyte - Schematic representation of the structure of the electrode-electrolyte interface. (a) distribution of molecules in the vicinity of the electrode for $\mu_{Me} < \mu_{Me^{z+}}$ (left panel) and $\mu_{Me} > \mu_{Me^{z+}}$ (right panel). (b) Linear potential drop due to separation of charges. A layer of electrons in the metal electrode, and a layer of solvated ions at the Outer Helmholtz Plane (OHP) form the electric double layer (DL).

(see Figure 2.1 a right panel). But ions can not come infinitely close to the surface, since they have a certain radius. All ions usually are solvated (i.e. they carry water molecules with them), which increases their effective radius even more. The centers of the attracted solvated ions is denoted the outer Helmholtz plane (OHP), whereas the centers of ions that have shed off their solvation shell in the position of closest approach is called inner Helmholtz plane (IHP). The layer of charges at the electrode surface and the layer of oppositely charged ions in the solution form the double layer (DL). It is more common to use the notion of a Stern double layer that includes stationary and diffuse layers of oppositely charged ions at the electrode surface. The potential first drops linearly across the mostly immobile charges of opposite sign and then drops exponentially into the solution, whereat this exponential drop is depending on the ion concentration or activities in the solution: the higher the concentrations the faster the drop. (see Figure 2.1 b).

2.2.5 Equivalent circuit

The electrode-electrolyte interface can be modeled by a series of capacitors. The overall capacitance stems from all different sources of charge separation: from the compact and the diffuse layer and also from the dipoles of the water molecules. The total capacitance of a series of capacitors is:

$$\frac{1}{C_{dl}} = \sum_i \frac{1}{C_i} \quad (2.8)$$

If one of the contributing capacitances is much larger than all others ($C_i \ll C_{j \neq i}$) this capacitance can be neglected. A metal-electrode interface is usually represented by using an arrangement of a capacitor and a resistor in parallel (see 2.6 below). As long as no chemical reaction occurs at the electrode, i.e. no faradaic current flows, the double layer acts mostly like a capacitor which can be charged and discharged. The metal solution interface capacitance per area in aqueous solution is very large (i.e. Pt electrode: $20 - 50 \mu F/cm^2$ Franks et al. (2005)) and technically utilized in supercapacitors. The capacitance of the diffuse layer changes with the applied voltage (Bockris et al. 2000). If a low electrolyte concentration is used this capacitance will get smaller. An electrode in aqueous solution is commonly modeled by a constant-phase element (CPE). The impedance of the CPE is $Z_{CPE} = \frac{1}{Q(\omega i)^n}$, where Q is the measure of the magnitude, n ($0 \leq n \leq 1$) describes how well it matches a capacitor ($n = 1$) or a resistor ($n = 0$). The CPE was introduced to allow for a better fit to measured data. However, the physical meaning of the CPE is not clear, but might be due to fringing effects of the electric field (Jorcin et al. 2006).

2.3 ELECTRODES AND CURRENT

The considerations up to now were all in a dynamic equilibrium, i.e., no net current was flowing. As soon as current flows through the electrode the compact and diffuse layers are perturbed and the electrode potentials are altered.

An electrode, where independent of the applied voltage no reaction occurs, is called ideally polarizable. Changing the applied potential only results in charging or discharging the electrode-electrolyte interface. The current involved in charging is called non-faradaic current. On the other hand there is the ideally non-polarizable electrode; an electrode where charge-transfer is completely unhindered. This means that all current is due to reactions happening at the electrode and not due to charging effects. The current involved in chemical reactions is called faradaic current. Both non-polarizable and polarizable electrodes do not exist in reality. Any electrode will have a polarization layer and any electrode will, upon applying a certain potential, allow for charge transfer.

2.3.1 Electrochemical instrumentation

If charge transfer occurs (i.e. a net current is flowing) due to the application of a voltage, the current is flowing through the WE and the same current will have to pass through the reference electrode (RE) in a two-electrode setup. The current will then alter the polarization of the RE, hence the electrode potential of the RE will change. This in turn will modify the effective voltage between WE and RE that the current will change.

To avoid this situation a three-electrode electrochemical setup is commonly employed (see Figure 2.2 a). The current is routed through a counter or auxiliary electrode (CE), and no current is allowed to pass through the RE so that the voltage between WE and RE is defined

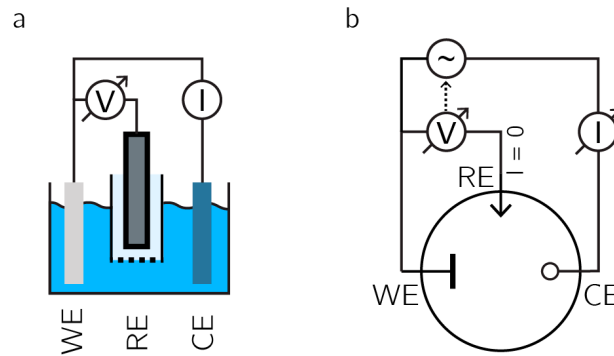


Figure 2.2: Three-electrode setup - (a) By introducing a counter or auxiliary electrode (CE), to provide the current to the cell, an electrode voltage can be measured with respect to the RE, without current passing through the RE, which would upset the electrode potential of the RE. (b) A potentiostat regulates the current through the counter electrode to define a voltage between WE and RE (the circle shows the electric symbol for the electrochemical cell).

and can be measured.

To define the voltage between WE and RE a potentiostat is used (Figure 2.2 b). The potentiostat controls the voltage between WE and RE and adjusts the current applied to the CE accordingly.

2.3.2 Voltage-current relation

In the case of an electrochemical half-cell, where electron transfer reactions occur at the electrode and where both, cathodic and anodic reactions can happen at the same electrode, the potential at the electrode will settle to a reduction potential as indicated by the Nernst equation. Oxidative and reductive currents are equal but opposite (no net current). Upon applying a potential, which is different from the reduction potential at equilibrium, a certain reaction will prevail over the other and a net current will flow. The deviation of the applied potential from equilibrium is called overpotential $\eta = (E - E_{eq})$. The net current density j due to the overpotential can be described by the concentration-dependent Butler-Volmer equation:

$$j = j_0 \cdot \left\{ \frac{c_R^{el}(t)}{c_R^{bulk}} \exp \left[\frac{\alpha n F}{RT} \eta \right] - \frac{c_O^{el}(t)}{c_O^{bulk}} \exp \left[-\frac{(1 - \alpha) n F}{RT} \eta \right] \right\} \quad (2.9)$$

where j_0 is the exchange current density (current per area), T the absolute temperature, n the number of electrons involved in the electrode reaction, F the Faraday constant and R the universal gas constant. α is the so-called charge transfer coefficient, which describes in which relation both reactions occur. The concentration of the reduced form of the species in the bulk solution is c_R^{bulk} , at the electrode surface $c_R^{el}(t)$, for the oxidized form of the

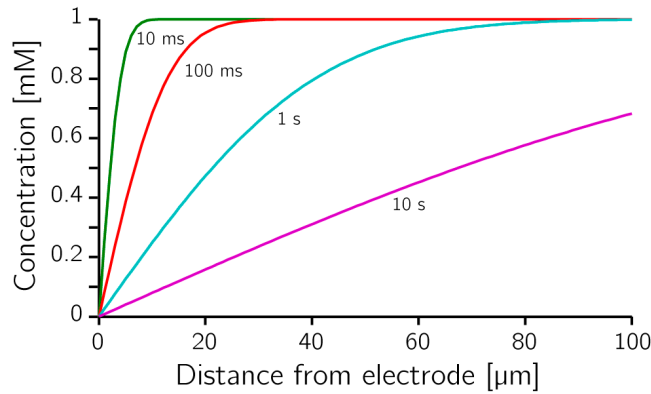


Figure 2.3: Concentration profile at electrode - Concentration profile due to diffusion at different points in time. ($c = 1 \text{ mM}$, $D = 5 \times 10^{-10} \text{ m}^2/\text{s}$)

species c_O^{bulk} and $c_O^{\text{el}}(t)$ respectively. The first term describes the anodic contribution, the second the cathodic. Please notice the polarities: as a positive overpotential is applied to the electrode, the reduced form of the species is oxidized. Electrons transfer into the electrode, the technical current is a positive current (out of the electrode). Tabulated values of the exchange current density j_0 can help to estimate currents that are expected at electrodes (see Chapter 3). Exchange current densities due to oxidation or reduction on platinum electrodes range from $1 \frac{\mu\text{A}}{\text{cm}^2}$ to $1 \frac{\text{mA}}{\text{cm}^2}$ ($10 \frac{\text{fA}}{\mu\text{m}^2} - 10 \frac{\text{pA}}{\mu\text{m}^2}$) (Hamann et al. 2007; Spiro 1964). To increase the current, the overpotential can be increased, however, if a certain potential is reached, secondary reactions may take place.

2.3.3 Diffusion limited currents

Upon increasing the overpotential, the reaction at the electrode surface will consume significant reactant, and the current becomes limited by the rate of transport of the reactant towards the electrode. The concentrations at the electrode will diminish until each arriving reactant will be converted immediately. The current is said to be "diffusion controlled".

Planar electrode

The Cottrell equation describes the chronoamperometric (current vs. time) response for a planar electrode. It is important to notice that, in contrast to the Nernst equation (logarithmic), there is a linear correlation between analyte concentration and obtained current:

$$i(t) = \frac{nFAc\sqrt{D}}{\sqrt{\pi t}} \quad (2.10)$$

A is the area of the electrode, c the bulk concentration of the reactant and D the diffusion coefficient. The current in a potential step experiment shrinks by \sqrt{t} .

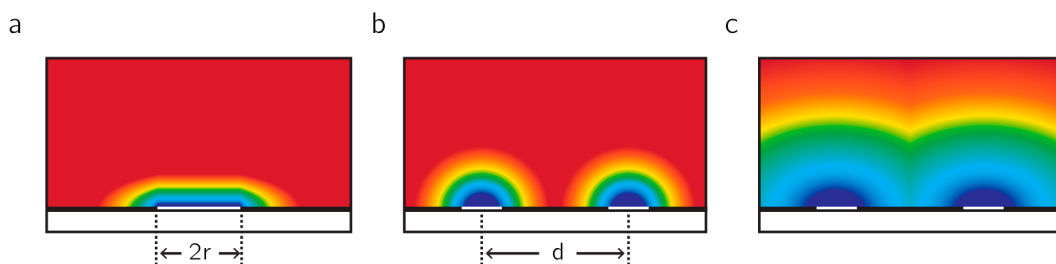


Figure 2.4: Diffusion regimes - In an array of microelectrodes of radius r and with a pitch of d there are several diffusion regimes: (a) initially there is planar diffusion over the surface of the electrode, (b) the layer will grow and exhibit a spherical diffusion profile, (c) until finally the diffusion profiles overlap, and the whole array has the diffusion profile of a large planar electrode.

The concentration profile of the reactant at a planar electrode at different time points can be seen in Figure 2.3. For a diffusion coefficient of $D = 5 \times 10^{-10} \text{ m}^2/\text{s}$ and a concentration of $c = 1 \text{ mM}$, the diffusion layer will have a thickness of $\sim 80 \text{ }\mu\text{m}$ after 1 s.

Disk microelectrodes

The Cottrell equation has been derived by solving Fick's second law of diffusion with appropriate boundary conditions. It also has been derived analytically for some other special cases, like the disk electrode and used to calculate the diffusion-limited current (Saito 1968). For a disk electrode the current is a linear combination of the Cottrell terms for planar diffusion and diffusion at the sides of the disk electrode. For steady-state, the contributions of planar diffusion (Equation 2.10) can be neglected. The transport-limited current is constant in time and independent of the applied overpotential:

$$i(t \gg t_0) = 4nFcDr \quad (2.11)$$

where r is the radius of the disk electrode and c the bulk concentration of the reactant. The current is proportional to concentration and radius of the electrode (and not the area).

2.3.4 Diffusion at microelectrode arrays

For a microelectrode array with electrodes of radius r and pitch (center-to-center distance) d one has to distinguish different diffusion regimes (see Figure 2.4): (i) planar diffusion on a single electrode, (ii) spherical diffusion on a single electrode, (iii) planar diffusion over the whole array. As soon as the reactions at the electrode start to be diffusion limited, the currents will diminish and be dominated by planar diffusion (see Figure 2.4 a), according to the Cottrell equation (2.10). The current is proportional to the area of the electrode and $1/\sqrt{t}$. The diffuse layer above the electrodes grows over time with a spherical shape

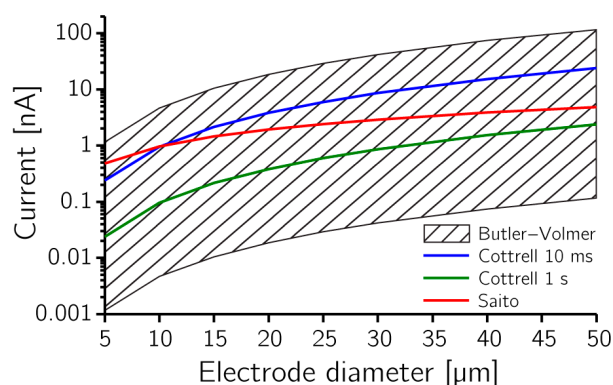


Figure 2.5: Diffusion-limited currents - Expected currents for different diffusion regimes and electrode diameters. The Butler-Volmer current range was calculated using $j_0 = 1 \frac{\mu A}{cm^2} - 1 \frac{mA}{cm^2}$, $\alpha = 0.5$ and $\eta = 0.1 V$. The blue and the green curve are the currents expected for planar diffusion during 10 ms and 1 s. The current due to spherical diffusion is shown in red.

(Lavacchi et al. 2009; Guo and Lindner 2009). The current is then dominated by the diffusion at the rim of the electrode and can be calculated using the radius of the electrode according to Equation 2.11 (see Figure 2.4 b). When the diffusion layer of neighboring electrodes overlap, the transport of the reactant will become slower and the currents decrease (see Figure 2.4 c). Upon complete overlap of the diffusion layers of neighboring electrodes, the whole array can be regarded as a single large planar electrode, and the currents are, again, defined by the electrode area and $1/\sqrt{t}$ according to the Cottrell equation.

2.3.5 Faradaic currents expected at microelectrodes

The maximum currents, which can be expected at a microelectrode is defined by the Butler-Volmer equation (Equation 2.9), hence, by the concentration, the overpotential applied, the standard exchange current density, and, finally, by the area of the electrode. Depending on the time-span of the experiments, different current limits can be expected. These currents are depicted in Figure 2.5 (hatched area) for the aforementioned diffusion regimes. The maximum currents for an overpotential of $\eta = 0.1 V$ range from $1 nA/mM$ for a 5- μm diameter electrode up to $100 nA/mM$ for a 50- μm diameter electrode. A lower limit can not be defined, considering an overpotential of $\eta = 0.1 V$ and exchange current densities for a sluggish reaction, then $\sim 1 pA/mM$ for a 5- μm diameter electrode is expected.

2.3.6 Equivalent circuit

After looking at both, the charge separation at the electrode-electrolyte interface and the charge transfer at the electrode, an electric equivalent model can be given (see Figure 2.6

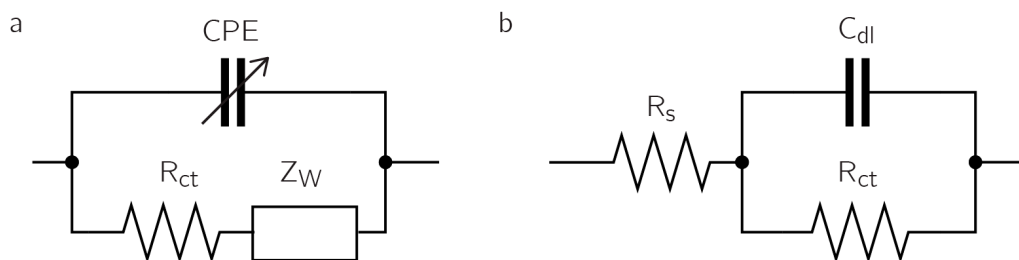


Figure 2.6: Equivalent circuit of the electrode-electrolyte interface - (a) CPE is the non-ideal capacitor including non-faradaic currents, the resistor R_{ct} in series with the Warburg impedance Z_W for modeling the faradaic currents. (b) Simplified equivalent circuit including the solution resistance R_s

a).

CPE is the constant phase element, R_{ct} is the faradaic charge transfer resistance, and Z_W the Warburg impedance, which models the effect of ions, produced on the surface of the electrode that have to diffuse away. In Figure 2.6 b a simplified version of the equivalent circuit is given, which does not include the Warburg impedance and which can be used as a transducer or sensor equivalent circuit model for designing the circuits. The DL capacitance C_{dl} is assumed to be constant and in parallel with a charge transfer resistance on the order of several $100\text{ M}\Omega$ for a $5\text{-}\mu\text{m}$ diameter electrode. It includes the solution resistance R_s . This resistance can be estimated by calculating the resistance of a disk electrode with radius r and an infinitely large CE located far away. In PBS (conductivity $\kappa = 15\text{ mS/cm}$) the resistance is in the range of $10 - 100\text{ k}\Omega$ ($R = 1/(4\kappa r)$) (Newman 1966).

2.4 SUMMARY

Upon immersion of an electrode into an electrolyte charge carriers (electrons and ions) will move to equilibrate differences in the electrochemical potentials. The movement of charges creates a space charge layer giving rise to an electrode potential. The electrode potentials are tabulated and can give an idea which reactions will happen at an electrode. The electrode potentials can be determined with respect to a reference electrode. The space charge layer of the electrode-electrolyte interface has a capacitive behavior and the metal-electrode solution interface capacitance in an aqueous solution amounts to $20 - 50\text{ }\mu\text{F/cm}^2$. When a current is applied, the space charge layer is disturbed and the electrode potential altered. Hence, current should not be passed through the reference electrode. Therefore, a potentiostat regulates the potential in the electrolyte by applying current to a third (the counter) electrode until the desired voltage is measured versus a reference electrode. The expected currents due to oxidation or reduction of a molecule range from 1 pA up to 1 nA for a

5- μm diameter electrode, and from 1 nA up to 100 nA for a 50- μm diameter electrode. In experiments concerning bulk concentrations (i.e. electrodeposition), diffusion effects will reduce the respective currents. Microelectrodes in electrochemical microarrays are in different diffusion regimes depending on the time scale. After some time (~ 5 s for a pitch of 100 μm) the diffusion layers of neighboring electrodes will overlap. A simple sensor equivalent circuit model consisting of the arrangement of the double-layer capacitance and the charge-transfer resistance in series with the solution resistance can be used for designing the circuits.

3

CIRCUIT DESIGN CONSIDERATIONS AND SPECIFICATIONS

To be able to perform electrochemical experiments on a large sensor array, there are two major blocks required: (i) the potentiostat to control the potential in the electrolyte and (ii) the current readout units to acquire the current and control the potential of the electrodes. The specifications for the circuits must be determined in order to realize the intended functionality. In this chapter, design considerations are described, and design choices for the complementary-metal-oxide semiconductor (CMOS) chip are explained.

3.1 ARRAY OF WORKING ELECTRODES

The dimensions of the sensing array (the number and total area working electrodes) have an impact on the entire chip design. They are the key factors in determining the specifications of the circuits.

3.1.1 Parameters

Parameters to consider include the size of the electrodes, the pitch (center-to-center distance), the electrode arrangement in the array and the electrode material.

The layout of the electrode array defines the spatial resolution that can be achieved. Concerning circuit design, the size or area of the electrode that is needed for implementing a certain electrochemical technique will determine the current range that the circuits must cover. The pitch of the electrodes determines the area and the space available for circuitry per pixel. The arrangement of the electrodes will have an impact on the electrochemistry and will be discussed later (see Chapter 5).

3.1.2 Considerations

The dimensions of the working electrodes should be on the same order of spatial dimensions as the biological cells. Cell diameters range from 0.7-1.5 μm for *E. coli*, 2-5 μm for Yeast (Srinorakutara 1998), through 10 μm for the soma of neuron (Meitzen et al. 2011), up to 15-30 μm diameter for HeLa cells.

3 CIRCUIT DESIGN

3.1.3 Realization

An array of 32×32 electrodes with a pitch of $100\ \mu\text{m}$ was realized. The electrodes were circular and were chosen to have a standard electrode diameter of $25\ \mu\text{m}$. To determine size dependence and to develop new applications, the diameters could be chosen within a range of $5\ \mu\text{m}$ to $50\ \mu\text{m}$. Although the area per pixel would allow circuitry to be placed underneath, it was decided to use a switch matrix and to place the readout circuitry at the periphery the array.

3.1.4 Discussion

The center-to-center distance (pitch) of $100\ \mu\text{m}$ is a compromise between high spatial resolution and sufficient margin for realizing the different electrode sizes. The round electrode opening reduces fringing effects of the electric field. The switch matrix allows for the routing of arbitrary electrodes to the readout channels and provides the means to readout all electrodes by multiplexing. By placing the readout circuits at the periphery of the array, the design of these circuits is not subject to any space restrictions imposed by the electrode pitch.

3.2 THE POTENTIOSTAT

To investigate processes happening at a working electrode of an electrochemical cell, a potentiostat is used. It controls the voltage between a reference electrode and the working electrode.

3.2.1 Parameters

Necessary parameters for the design of the potentiostat are the voltage range and the slew rate and bandwidth for the expected load. The potentiostat must provide a suitable voltage range for the envisaged electrochemical applications; it must provide the currents for the reactions on the working electrodes and for charging the double layer (DL); the potentiostat must regulate the voltages at a proper speed while remaining stable in its operation.

3.2.2 Considerations

In Figure 3.1 the equivalent circuit of an electrochemical cell in a three-electrode setup is shown. The counter electrode (impedance Z_{CE}) is used to control the potential in the electrolyte; the reference electrode (impedance Z_{RE}) measures the potential in the electrolyte; and the working electrode (modeled by the parallel combination of the double-layer capacitance C_{DL} and the charge-transfer resistance R_{CT}) is used to measure the current. Since no

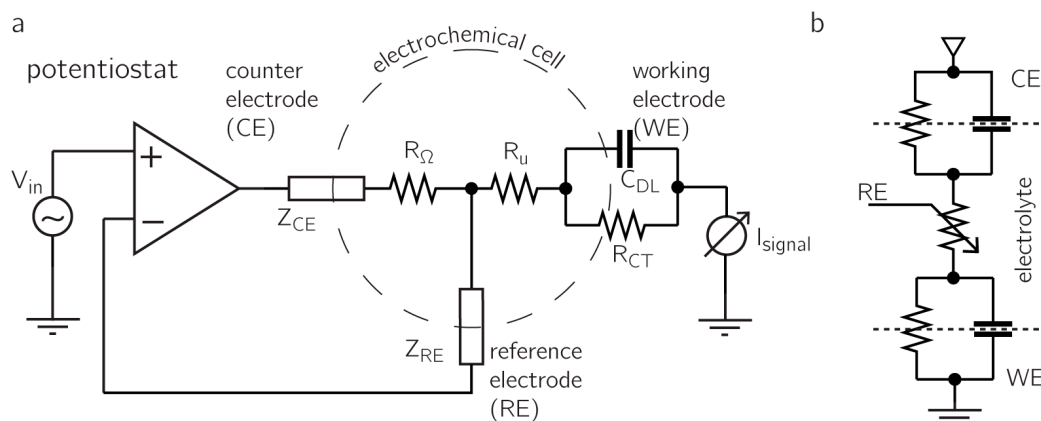


Figure 3.1: Electrochemical cell - (a) Potentiostat with equivalent circuit of electrochemical cell (in the dashed circle). (b) effective load as seen by the potentiostat formed by the voltage divider of counter or auxiliary electrode (CE), working electrode (WE) and the resistance of the electrolyte R_s .

current is flowing through the reference electrode (RE), the feedback loop of the amplifier can compensate for the impedance of the CE and part of the solution resistance (i.e. R_Ω). The uncompensated solution resistance (R_u) will still alter the voltage drop at the electrode. However, at expected current levels of nA for single electrodes, the uncompensated resistance R_u (which is in the range of 100 k Ω) does have a negligible effect on the applied voltage, however, it is important in defining the time-constant to charge the DL capacitance C_{dl} (see Chapter 6).

The usable voltage range in aqueous solutions on platinum electrodes ranges from -0.28 V to $+1.15$ V (in H_2SO_4 pH 0.9) with respect to an Ag/AgCl reference electrode. The position of this potential window depends on the pH of the electrolyte and shifts with -59 mV/pH (see Chapter 2). The useful potential range in PBS (pH 7.2) is -0.62 V to $+0.90$ V (Hudak et al. 2010). If the electrodes are functionalized, other limits apply: for gold the potential window is, for example -0.25 V to $+1.55$ V (see Chapter 7). Hence, a conservative estimation for the voltage range to be established between RE and WE, is -0.8 V to $+1.6$ V vs. Ag/AgCl. The electrochemical cell can be seen as a voltage divider (see Figure 3.1 b). To establish a certain voltage at the RE, the voltage at the CE has to be larger according to the impedances of the CE and the WEs. Therefore, to lower the voltage overhead needed at the CE, it is required to provide a large CE in order to lower the impedance and for avoiding electrode polarization (see Chapter 5).

The impedance of the working electrodes mainly determines the load, which the potentiostatic loop must drive. Platinum electrodes in phosphate-buffered saline (PBS) have a characteristic interface capacitance of 20–50 $\mu F/cm^2$, which sums up to 100–250 nF for 1024 disk electrodes of 25 μm diameter (see Chapter 2). The experimental conditions and the number of working electrodes that are used in an experiment may change considerably,

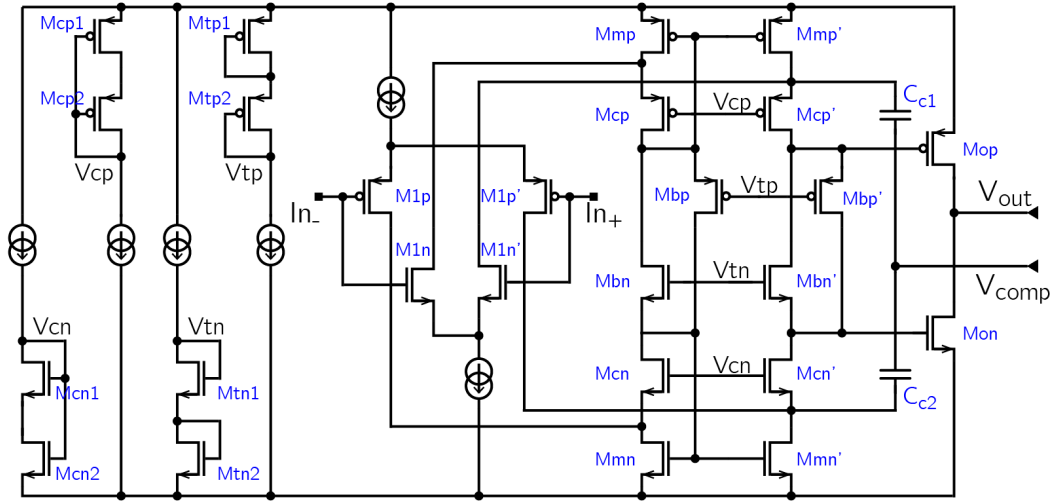


Figure 3.2: Potentiostat Opamp - 2-stage amplifier with rail-to-rail input and output. The first stage is a folded cascode OTA, which includes a floating current sources, the second stage is a class AB output stage. The two branches on the left are used for biasing of the floating current sources via a translinear loop.

which, in turn, means that the load for the amplifier can vary considerably.

The speed requirements depend on the technique used. Pulse voltammetry techniques (see Chapter 6) require the fastest slew rate to provide rectangular pulses to the whole electrochemical system. Pulses are in the range of 10–100 ms; the pulse steps between 5–50 mV. If the potentiostat is supposed to use a maximum of 1 μ s (i.e. 1/10000th of the pulse duration) for slewing in this scenario, a slew rate of 50 kV/s would be sufficient.

3.2.3 Realization

The potentiostat on the chip is realized by a two-stage amplifier with rail-to-rail input and output (see Figure 3.2 and Hogervorst et al. (1994)). The first stage is a rail-to-rail folded-cascode operational transconductance amplifier (OTA), including floating current sources (Mbn, Mbp, Mbn', Mbp'). The floating current sources are biased via translinear loops (i.e. via Mtp1, Mtp2, Mbp, Mmp). The output stage is of class AB. In order to drive a wide range of loads at high stability, the amplifier is compensated with large (40 pF) pole-splitting capacitors. Switches connect the amplifier to internal or external counter and reference electrodes. To avoid decoupling of the load via the switch resistances, the compensation path is fed back into the summing nodes of the folded cascode by using an additional parallel path. This removes the decoupling effect of the switch resistances and is equivalent to an increase in output impedance of the amplifier.

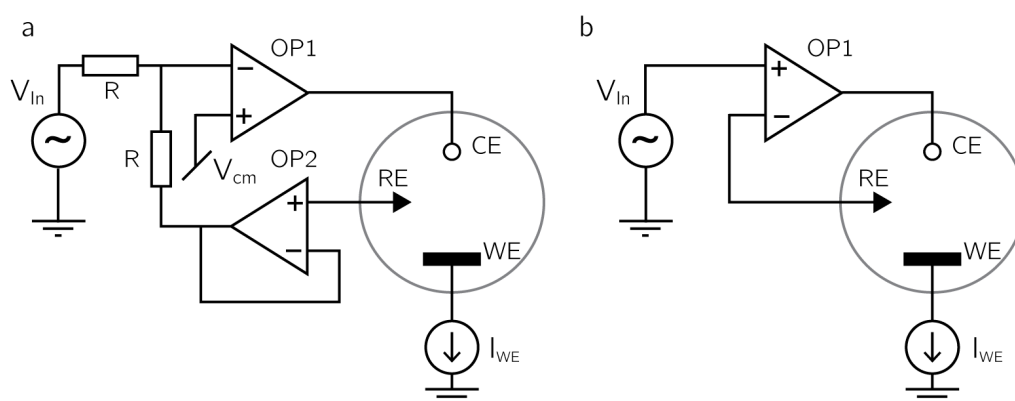


Figure 3.3: Potentiostat alternatives - analog realizations: (a) Inverting amplifier structure. A voltage follower is used to avoid current flowing through the reference electrode (RE). (b) Single amplifier solution.

3.2.4 Discussion

A single stage amplifier, with the dominant pole at the output (i.e. the CE) is slowed down as the capacitive load increases. However, single-stage amplifiers are limited in gain, and to achieve a large voltage range, a rail-to-rail implementation is desirable. A large compensation capacitor is needed to split the non-dominating and the dominating poles. Martins (2011) implemented a two-stage amplifier with capacitive multiplication to reduce the size of the capacitor needed for compensation. This is feasible for large and defined loads; however, if the load is connected via resistances and when only few working electrodes are used for a measurement (light load) the compensation fails. Having the dominant pole at the output is another option to guarantee stability for large loads. This entails two requirements: (i) the parasitic capacitances must be kept low in the first stage for the non-dominant pole to be at high frequencies, and (ii) the capacitor at the output must be large to keep the dominant pole at low frequencies.

For a three-electrode setup, there are two implementations that are widely used (A. Frey et al. 2003; S. Martin et al. 2005): one being an adder amplifier with a voltage follower to buffer the voltage of the reference electrode (Figure 3.3 a); the second implementation (Figure 3.3 b) is realized by a single single amplifier with the output connected to the counter electrode (CE), and the inverting input connected to the reference electrode (RE). An alternative is to realize the potentiostat digitally: the voltage of the reference electrode is digitized, and the feedback to the counter electrode is performed in the digital domain. A DAC is used to set the voltage of the counter electrode. This implementation has the advantage that the dynamic characteristics of the feedback loop can be kept variable. Care must be taken to provide enough resolution, otherwise the voltage cannot be regulated precisely enough.

The different implementations have advantages and disadvantages: The realization by using

two amplifiers allocates the tasks of driving the electrochemical cell and buffering the voltage of the RE to two opamps. In order to not affect the stability of the loop, the unity-gain bandwidth of OP2 has to be much larger than the pole frequency caused by the electrochemical cell. One clear drawback for integration in a CMOS chip is the resistive load that the second opamp (OP2) needs to drive. The other drawback of the adder amplifier is that the voltage at the RE is the inverse of V_{in} with respect to V_{cm} . The flexibility of the digital approach would come at the cost of an additional ADC and DAC on the chip. The single amplifier approach can be used to avoid the aforementioned drawbacks at the cost of a slightly more complex amplifier design.

3.3 CURRENT READOUT

3.3.1 Parameters

Parameters relevant for the design of the current readout circuits are the current range, the resolution needed to measure small signals within a defined range, and the required signal bandwidth. The oversampling ratio (OSR) is the ratio of the sampling rate to the Nyquist rate. By increasing the OSR, the signal-to-noise ratio (SNR) will increase and therefore the resolution. OSR couples sampling frequency, bandwidth, and resolution together. It can be seen either as a design specification, or, if the sampling frequency is given, as a variable.

3.3.2 Considerations

Besides the faradaic currents, which were estimated before (see 2.3.5), there are non-faradaic (background) currents from charging the DL of the electrodes. The double layer capacitance of blank platinum electrodes in aqueous solution ranges from $200 - 500 \text{ fF}/\mu\text{m}^2$ (Bockris et al. 2000; Franks et al. 2005). Depending on the electrochemical technique used and the corresponding required voltage waveforms, the non-faradaic charging current can be dominant. For a standard cyclic voltammogram (CV) (see Chapter 6) and a sweeping rate of 100 mV/s , the background current for a $25\text{-}\mu\text{m}$ diameter electrode will be $I = C_{dl} * dV/dt = 10 - 25 \text{ pA}$. If the electrodes are functionalized, the capacitance can increase by a factor of up to 150 as the active surface area may, due to the deposited material, increase by a factor of up to 1000 (see Chapter 7).

To cope with the different scenarios, a large dynamic range and high resolution is needed, which is the area where sigma-delta converters excel.

The bandwidth required, when using methods without voltage variation, is determined by the signal source. In the case of single cell exocytosis, the time scale of a single event is on the order of tens of milliseconds (Amatore et al. 2008).

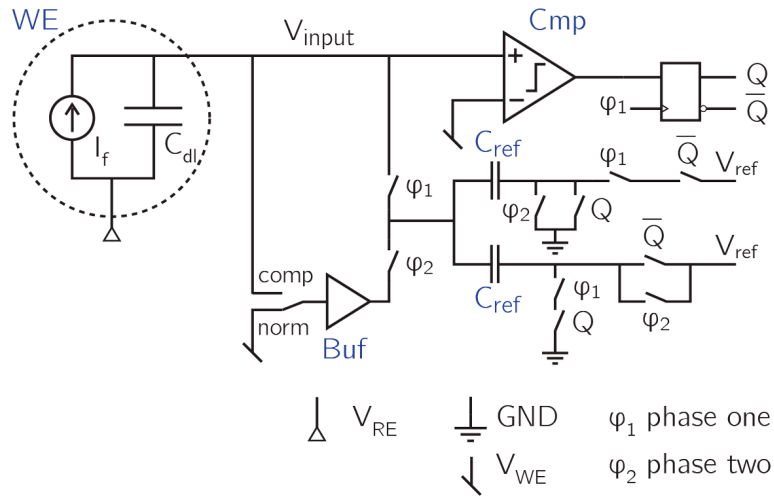


Figure 3.4: SD1 - Schematic view of the 1st-order sigma-delta converter. The faradaic currents are integrated on the double-layer capacitance of the working electrode (dashed circle). If in phase two, the reference capacitors are connected to the voltage of the electrode (V_{input}) instead of the desired working electrode voltage (V_{WE}), the non-ideal charge transfer is compensated.

3.3.3 Realization

To achieve a high resolution without the need for trimming passive components, two direct current sigma-delta converters were employed in this work. One implementation is based on a first-order sigma-delta converter and uses the electrode capacitance as a circuit element (Heer et al. 2008). The other readout implementation is a direct current second-order sigma-delta converter. The second-order sigma-delta converter was designed to achieve higher resolution and to verify the functionality of the unconventional first-order sigma-delta converter implementation.

1st-order sigma-delta converter

The first-order sigma-delta converters (Figure 3.4) perform the integration on the double-layer capacitance (C_{dl}) of the electrode in the electrolyte (Heer et al. 2008).

The converter consists of only a comparator, a flip-flop and a switched-capacitor DAC to realize the sigma-delta loop. This loop keeps the voltage of the working electrode near the trigger voltage of the comparator by adding charge to or subtracting charge from the double-layer capacitance (C_{dl}). When operated at high frequencies ($\gg 1$ kHz), the average voltage at the input tracks the working electrode voltage (V_{WE}). The double-layer capacitance is charged or discharged by the reference capacitors (C_{ref}) of the switched-capacitor DAC. Hence, the double-layer capacitance of the electrode/electrolyte interface (shown in

the dashed circle of Figure 3.4) is used as a circuit element. Using the electrode-electrolyte double layer as an integration capacitor is not ideal, mostly because the charge of the reference capacitors is not completely delivered to the electrode, when the two capacitances are connected (phase 1). The result is a non-ideal integration, which can cause dead-zones in the converter response. To improve the non-ideal integration on the double-layer capacitance, a compensation scheme is implemented. Instead of the desired working electrode voltage (V_{WE}), in phase two, the actual voltage at the electrode (V_{input}) is applied to the capacitors with the help of a buffer (Buf). This compensation circuit reduces dead-zones, thereby improving linearity. The switching capacitors represent the 1-bit DAC of the sigma-delta converter. Additionally V_{ref} can be kept constant even if the voltage at the working electrode is altered during the experiment. The current can be determined from the decimated bitstream by:

$$I = C_{ref} \cdot V_{ref} \cdot f_s \cdot x \quad (3.1)$$

where C_{ref} are the reference capacitors, V_{ref} the reference voltage f_s , the clock frequency and x the decimated value of the converter ($-1 < x < 1$). The value is independent of the value of the double-layer capacitance. There are three different capacitor ($C_{ref} = 100 \text{ fF}, 1 \text{ pF}, 10 \text{ pF}$) pairs to choose from, and together with the reference voltage ($V_{ref} < 1 \text{ V}$) and the clock frequency ($f_s < 1 \text{ MHz}$), current can be measured in a wide range ($100 \text{ pA} - 10 \text{ }\mu\text{A}$). The comparator is realized by an open-loop folded-cascode preamplification stage with rail-to-rail inputs followed by a latched comparator. Latched comparators have low power consumption, however, they have large offset and suffer from kickback noise due to the large output voltage variations that can capacitively couple to the input and can distort the input signal. A preamplification stage (i.e. the folded cascode OTA) reduces these effects (Johns and K. Martin 1997).

2nd-order sigma-delta converter

The second-order sigma-delta converters (Figure 3.5) constitute of two switched-capacitor integrators. Virtual ground of the first stage can be set to V_{WE} and defines the voltage at the working electrode. To provide the required voltage range, an amplifier with rail-to-rail input is required. Due to the sigma-delta loop, the output of the first stage is a signal close to its virtual ground; hence, the output of the first amplifier must also be rail-to-rail. The coefficients of the converter are optimized to reduce the signal swing at the output of the integrator to around 100 mV. The DC output of the first stage is voltage-shifted to half of the supply voltage by C_{12} , in order to reduce the requirements on the signal swing of the second stage. The DAC scheme used, is the same as that of the first-order sigma-delta converter. The current range ($100 \text{ pA} - 2 \text{ }\mu\text{A}$) can be set by choosing one out of two different reference ($C_{ref} = 200 \text{ fF}, 2 \text{ pF}$) and integrator capacitor values, by setting the reference voltage and the clock frequency. The quantizer is realized by a latched comparator. Kickback noise associated with latched comparators will only affect the output of the second stage, where the signals are already amplified. This amplification makes additional kickback noise

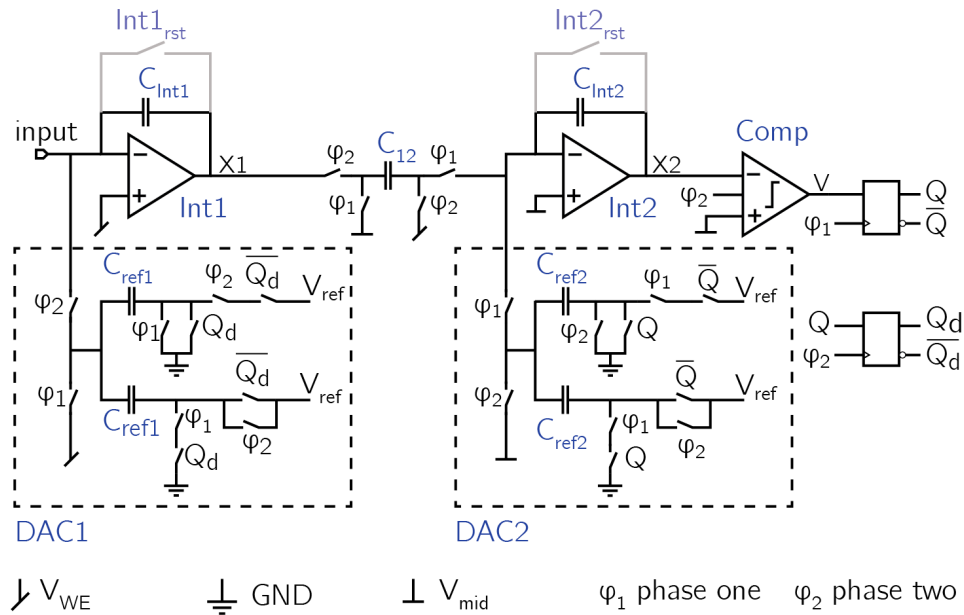


Figure 3.5: SD2 - Schematic view of the 2nd-order sigma-delta converter. The first integrator stage is set to the desired working electrode voltage, C_{12} shifts the voltage to mid-supply for the second stage. The charge on the reference capacitors is independent of the voltage on the electrode.

reduction techniques unnecessary. Q , \overline{Q} , Q_d , $\overline{Q_d}$ denote the digital bit stream of the ADCs, the inverse, and the delayed versions of it. The current is again solely determined by the switched-capacitor DAC and can be determined by Equation 3.1.

The second order sigma-delta converters can be used in an incremental mode, i.e., upon conversion of one value, the integrators are reset (via switches $\text{Int}1/2_{rst}$) for the next conversion cycle. This feature is used for reading out the whole array rapidly.

To be able to compare the two sigma-delta converters – especially the usage of the double-layer of the electrode-electrolyte interface – the second stage of SD2 can be disabled and thereby the noise shaping is degraded to that of a first-order sigma-delta converter. This is done by keeping the integrator in reset (via switch Int2_{rst}) and disabling the corresponding DAC. The first integrator, in this mode, still maintains the working electrodes constantly at the desired potential.

Clock

The clock distribution circuits produce a slow and shifted clock signal so that each converter operates on each channel at a different time-point in order to avoid simultaneous switching and large peak currents. The internal clock signals for the two sigma-delta converter implementations are provided by two non-overlapping clock phases.

3 CIRCUIT DESIGN

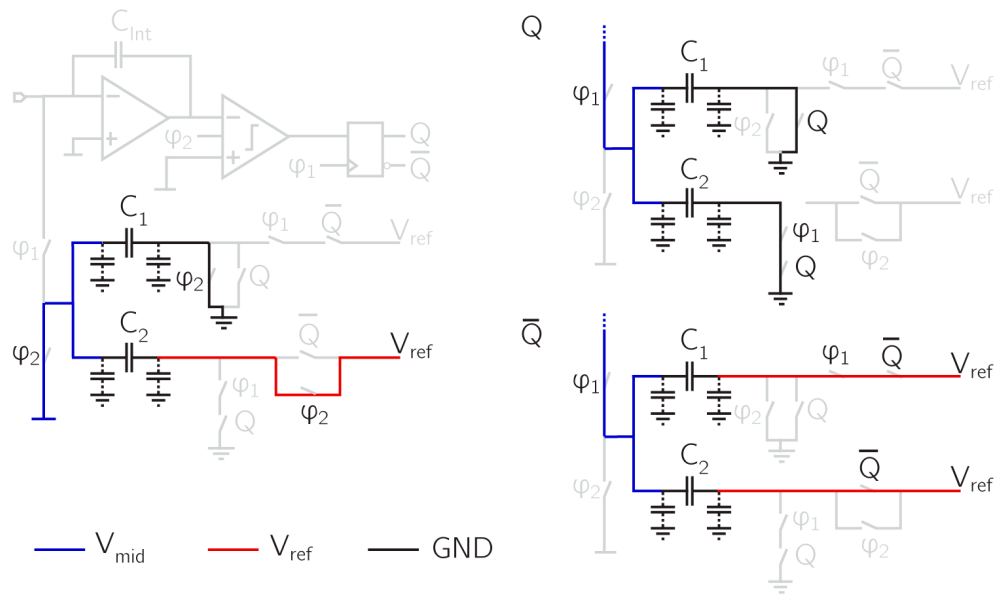


Figure 3.6: Switched capacitor DAC scheme - Left panel (clock phase 2): charging of both reference capacitors, right panel (clock phase 1): charge delivery to the integrator for the case of Q and \bar{Q} . Parasitic capacitances are shown with dashed wires. On the charge delivery side, the parasitic capacitances are kept at V_{mid} during both clock phases, on the reference voltage side, they are charged and discharged by voltage sources. Hence, no charges are delivered to the reference capacitors.

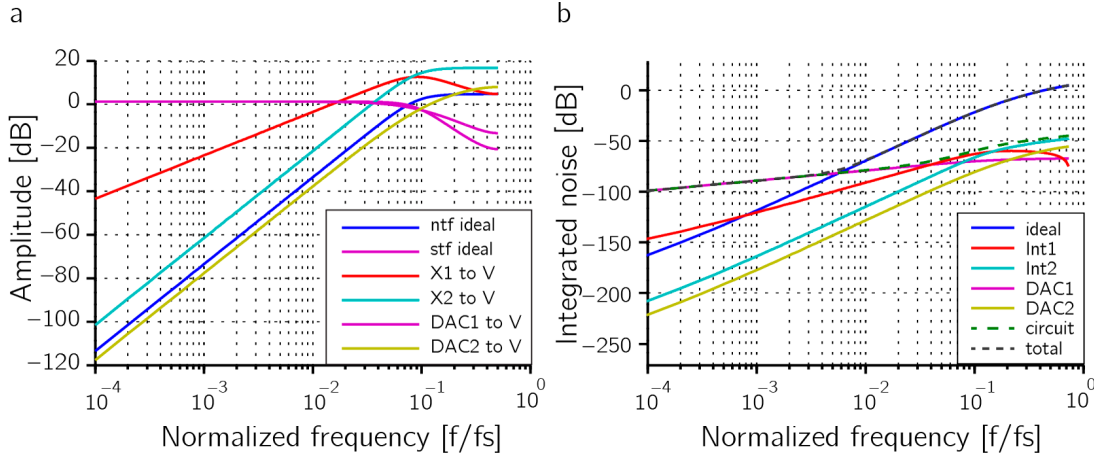


Figure 3.7: Noise contributions - (a) transfer functions from the noise source to the output of the converter. X1 is the output of the first integrator, X2 the output of the second integrator, Y is the output of the quantizer (i.e. the comparator), (b) integrated noise vs. full scale signal power. $V_{ref} = 0.1 V$ $C_{ref} = 2 pF$.

DAC scheme

The DAC scheme was chosen because it allows for setting the charge on the reference capacitors by applying V_{ref} with respect to ground for both positive and negative charges. It is independent of the voltage on the summing node (i.e. V_{mid}). However, this advantage comes at the cost of second capacitor.

During phase 2 C_1 and C_2 are charged:

$$Q_1(\phi_2) = C_{ref}V_{mid} \quad \text{and} \quad Q_2(\phi_2) = C_{ref}(V_{mid} - V_{ref}), \quad (3.2)$$

in phase 1 the charge is added or removed, depending on the previous decision of the comparator (i.e. Q or \overline{Q}) to the integrator according to:

$$\Delta Q_{\overline{Q}} = Q_2(\phi_2) - C_{ref}V_{mid} = -V_{ref}C_{ref} < 0 \quad (3.3)$$

$$\Delta Q_Q = Q_1(\phi_2) - C_{ref}(V_{mid} - V_{ref}) = V_{ref}C_{ref} > 0 \quad (3.4)$$

The implemented DAC scheme has a robust immunity to parasitic capacitances (see Figure 3.6). On the integrator side, the parasitic capacitances are kept at V_{mid} during both clock phases. On the reference voltage side, the parasitics are charged or discharged by voltage sources, which does not influence the charge on the reference capacitors. The parasitics extracted from layout of the DAC on the summing node side are $90 fF$, and $40 fF$ on each of the V_{ref} branches, respectively.

Noise contributions

To estimate the noise contributions, the transfer functions from the noise source to the quantizer of the sigma-delta converter (V) were determined (see Figure 3.7 a). The noise powers were determined from simulations and from manual calculations. The noise power of the integrators was determined by integrating the output noise power from 1 to 1 GHz. The contribution for a configuration of $V_{ref} = 0.1\text{ V}$ and $C_{ref} = 2\text{ pF}$ can be seen in Figure 3.7 b. The theoretical SNR is 76 dB for an OSR of 128, if we assume the signal power of a full scale signal. Above an OSR of 100 the noise of the first DAC is dominant.

The noise of the first DAC needs further investigation: The maximum equivalent signal charge from the input is determined by the full scale range, e.g. the range which can be compensated by the DAC. Signal charge and the noise charge of the first DAC can be calculated:

$$\overline{Q_{sig}} = \frac{Q_{FS}}{\sqrt{2}} = \sqrt{2} \cdot C_{ref} \cdot V_{ref} \quad (3.5)$$

$$\overline{Q_{noise}} = \sqrt{kT C_{ref}} \quad (3.6)$$

$$(3.7)$$

And the SNR, which can be achieved due to the DAC, can be determined:

$$SNR = 10 \log \frac{\overline{Q_{sig}}^2}{\overline{Q_{noise}}^2} = 10 \log \frac{2 \cdot C_{ref} \cdot V_{ref}^2}{kT} \quad (3.8)$$

$$(3.9)$$

Hence, the smaller C_{ref} for a given full scale range (constant $C_{ref} \cdot V_{ref}$), the larger the SNR (see also Chapter 4). This is counter intuitive to the typical preference of having a large capacitor due to switched-capacitor noise (kt/C).

3.3.4 Discussion

Different realizations of sigma-delta converters include continuous-time and discrete-time realizations with different signal feedback and feed-forward structures. Continuous-time realizations of sigma-delta converters impose lower requirements on settling time (i.e. lower power consumption) and provide an inherent anti-aliasing (Cherry and Snelgrove 1999). However, the clock rate must be fixed to preserve the coefficients that define the noise shaping. Continuous time sigma-delta converters are more sensitive to jitter, if non-return-to-zero feedback DACs are used. On the other hand, if switched-capacitor DACs are used, the aliasing rejection can be compromised, thereby degrading one of the most advantageous features of continuous-time operation (Pavan 2011). A discrete-time sigma-delta converter with a switched-capacitor DAC allows the clock rate to be used as another parameter to control the full scale range.

Custom-designed CMOS chips for amperometry or voltammetry, including an array of on-chip electrodes and current readout front-ends to condition the signals, have been designed previously. The respective front-end circuits were based on capacitive (Levine et al. 2008; Kruppa et al. 2010; Augustyniak et al. 2006; Inoue et al. 2012; Mason et al. 2007; Manickam et al. 2012) or resistive (Hwang et al. 2009; S. Martin et al. 2005; Bellin et al. 2014) transimpedance amplifiers, while others employed current conveyors to control the voltage and cope with the large capacitance of the double-layer (Schienle et al. 2004; Nazari et al. 2013; Kim et al. 2013).

Sensor systems with on-chip ADCs were based on current-to-frequency (I-to-F) conversion (Schienle et al. 2004; Nazari et al. 2013), single-slope or dual-slope ADCs (Levine et al. 2008; Nazari et al. 2013; Mazhab-Jafari et al. 2012) and successive approximation register (SAR) ADCs (Kruppa et al. 2010). For bandwidths of more than 100 Hz, better resolution (> 10 bit effective) has been achieved by using a direct current sigma-delta converter (SDC), where the front-end circuits are included in the ADC (Heer et al. 2008) (without electrodes (Stanacevic et al. 2007; Roham et al. 2008; Mollazadeh et al. 2009)).

The CMOS devices with embedded ADCs, however, did not exploit the CMOS advantage of acquiring rapid electrochemical image sequences. Many of the presented devices are designed for specific use (i.e., detection of DNA (Kruppa et al. 2010; Mazhab-Jafari et al. 2012; Schienle et al. 2004)) and are limited with regard to array dimensions and/or electrode number (< 200 electrodes (Nazari et al. 2013; Levine et al. 2008; Mazhab-Jafari et al. 2012)), detectable current range (> 10 pA, < 350 nA (Nazari et al. 2013; Schienle et al. 2004; Levine et al. 2008)), and resolution (< 9 -bit effective (Levine et al. 2008; Nazari et al. 2013)).

4

SYSTEM DESCRIPTION AND CHARACTERIZATION

The measurement system entails three major blocks (see Figure 4.1):

(i) The CMOS chip with the main features integrated on chip, including the array of electrodes, the sigma-delta current ADCs (SD1 and SD2), the master potentiostat, and auxiliary circuits. (ii) A PCB with an FPGA including a microcontroller soft core and custom peripheral cores for filtering of the bit streams from the sigma-delta converters, performing automated tasks with a real time engine (such as running cyclic voltammograms (CVs)) and for packaging data into frames to be transmitted to the computer. (iii) The software running on a computer to program and control the experiments via a graphical user interface in LabVIEW (National Instruments), and a MATLAB (MathWorks) toolbox to perform analysis of the recorded data sets.

In the following chapter the measurement system is described and characterized.

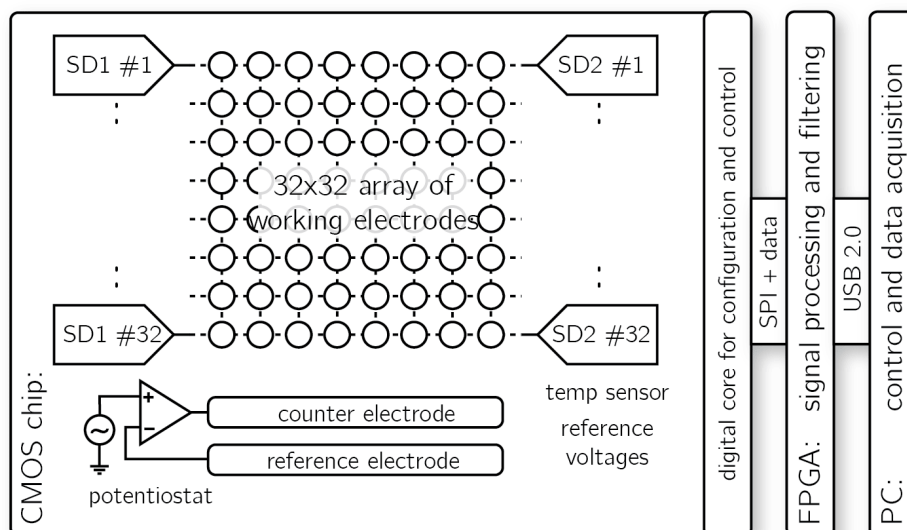


Figure 4.1: System block schematic - an overview of the measurement system with the three main blocks involved: the CMOS chip, the PCB including the signal-processing FPGA and the software.

4 SYSTEM DESCRIPTION AND CHARACTERIZATION

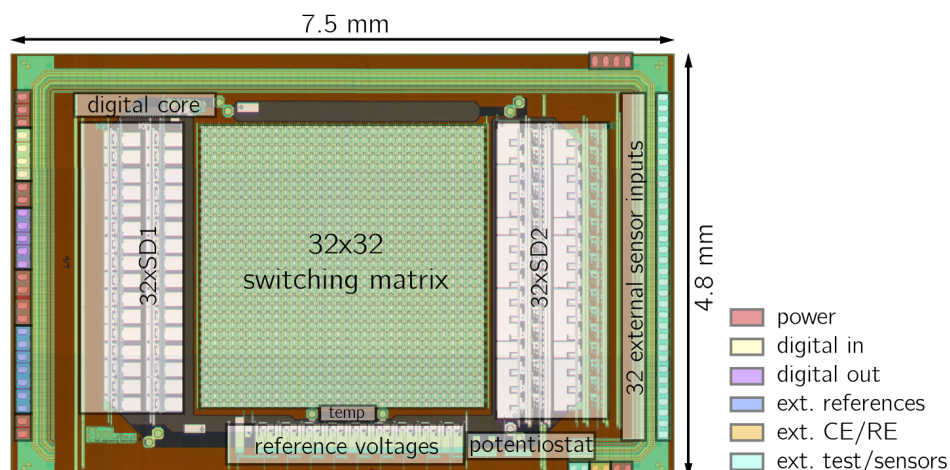


Figure 4.2: Micrograph of the CMOS chip - showing the major circuit blocks and the pad types. The chip system can be used without external analog signals.

4.1 CMOS CHIP

The CMOS chip is suitable for performing amperometric and voltammetric electrochemical experiments on 1024 working electrodes. Configurations of arbitrary electrodes can be connected to the readout channels or to external inputs via a flexible switching matrix. A master potentiostat (control amplifier) controls the potential in the electrolyte, whereas the working electrodes can be set to two different voltages, providing bi-potentiostatic capability. There are 32 identical first-order and 32 second-order sigma-delta converters to measure the current. A digital serial interface is implemented for control of the chip. The circuit specifications are summarized in Table 4.1. The micrograph of the chip with the major circuit blocks can be seen in Figure 4.2. The chip has a size of 7.5 × 4.8 mm² and has been fabricated on a 2-polysilicon-4-metal-layer 0.35-μm standard CMOS process (X-FAB, Erfurt, Germany).

4.1.1 Switching matrix

Working electrodes are connected directly to an underlying 32-by-32 switch matrix. The electrodes can be accessed in two different modes; in the row-mode, arbitrary selected electrodes in each row of the array can be connected to one readout channel; in the block-mode, each electrode of an arbitrary chosen 4 × 8 subarray is connected to an individual readout channel allowing for continuous monitoring in a high-density patch. To acquire the current of all on-chip electrodes, the switch-matrix is operated in a multiplexing sequence.

A. Array of electrodes	
number of working electrodes	1024
arrangement	32 × 32
pitch	100 μm
surface material	Pt
B. Potentiostat	
max. potential range (CE-WE)	0-3.3V
resolution (LSB)	2.8 mV
RE voltage range	0-2.8 V
C. SD modulators	
1 st order SDCs	32
full-scale range	1 nA - 10 μA
bandwidth	500 Hz
OSR	256-1024
area per channel	250×200 μm^2 (+180×200 μm^2 buffers)
2 nd order SDCs	32
full-scale range	100 pA - 2 μA
bandwidth normal mode	1 kHz
bandwidth fast mode	8 kHz
OSR	128-256
area per channel	450×200 μm^2 (+200×200 μm^2 buffers)

Table 4.1: Circuit specifications

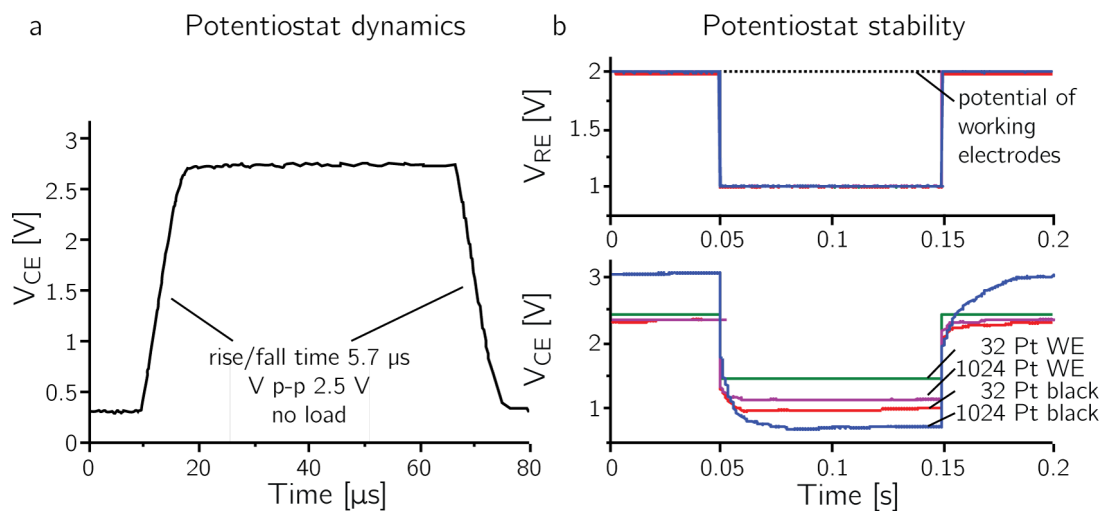


Figure 4.3: Potentiostat - (a) Step response of the potentiostat without external load showing a slew rate of 350 kV/s. (b top) Voltage at the Ag/AgCl reference electrode for a step of 1 V under different load conditions (solid lines are on top of each other). Dashed line denotes the potential of the working electrodes. (b bottom) Corresponding voltage at the on-chip counter electrode controlled by the potentiostat for a load of 32 bright Pt (green curve), 1024 bright Pt (magenta curve), 32 Pt black (red curve) and 1024 Pt black (blue curve) working electrodes.

4.1.2 Master potentiostat

The dynamics of the master potentiostat were determined by applying a pulse of 2.5 V peak-to-peak under dry conditions through connecting the counter-electrode directly to the reference electrode. Functionality and stability were tested under dry conditions by connecting external capacitors (up to 100 μ F) and in PBS with an external standard Ag/AgCl reference electrode and the on-chip platinum counter-electrode. In PBS, connecting different numbers of bright platinum working electrodes and Pt-black-covered working electrodes provided the different load conditions. To test for stability, a square wave of 1 V vs. Ag/AgCl was applied, and the voltages at the reference and counter electrodes were monitored. The master potentiostat was tested for speed and stability (Figure 4.3). The slew rate was determined to be 350 kV/s (Figure 4.3 (a)) with the counter-electrode output and the reference-electrode input shorted. Having a high slew rate is a prerequisite for being able to provide steep square wave pulses as used in deposition protocols. For a pulse of 1 V amplitude the slew rate of the amplifier adds a negligible 2.9- μ s rise time. A mandatory system requirement is the control loop stability. An external capacitor of 1 μ F entailed the smallest phase margin, which was 66°. The upper plot in Figure 4.3 (b) shows the voltage of the Ag/AgCl reference electrode. When applying a square wave to the input, the response of the amplifier showed high stability and no ringing for very small loads — 32 25- μ m-diameter bright Pt

electrodes — and for large loads — 1024 electrodes modified with Pt black. The lower plot in Figure 4.3 (b) shows the corresponding voltage at the counter electrode. The voltages at the counter electrode are usually not considered, because they are forced to a certain value by the potentiostatic loop in order to provide the preset potential at the reference electrode. However, one can see the effect of the different loading conditions on this voltage and the resulting requirements for the circuitry. When only 32 bright-platinum electrodes are connected, the current through the counter electrode is small, does not alter the interface, and, as a result, the voltage at the electrode just reproduces the voltage at the reference electrode with some offset. When 1024 electrodes, modified with Pt black are connected, the perturbation of the electrode interface of the counter electrode due to flowing currents is much larger, the peak-to-peak voltages are higher, and the voltage curve is not a simple reproduction of that at the reference electrode anymore. In a simplistic view, the counter electrode and the working electrodes form a capacitive divider. The large area, chosen for the counter electrode, lowers its impedance, thereby reducing the voltage overhead needed to provide a certain potential in the electrolyte.

4.1.3 Current readout

To test the analog-to-digital converters, a sinusoidal current was generated by a voltage source (DS360 Stanford Research Systems, U.S.), connected in series to different resistors ($1\text{ M}\Omega$ - $100\text{ M}\Omega$), depending on the targeted range. On-chip test current sources were used to perform a functional testing and to equalize the different channels. The bit stream of the sigma-delta converter under test was recorded via the measurement setup. To assess the performance of the 1st-order sigma-delta converters, PBS was used as an electrolyte to establish the double-layer capacitance at the electrode, which is needed for the integration function. The electrodes were bright platinum electrodes, the voltage was set to 0 V vs. Ag/AgCl. The electric characterization of the 2nd order SDC was performed under dry conditions by using the same equipment as for the 1st order SDC. All tests were conducted without a Faraday cage to mimic real working conditions. The performance of the two different SDC current-readout schemes is summarized in Table 4.2 for different range settings.

First-order sigma-delta converter

The best signal-to-noise-and-dynamic-range ratio (SNDR) of the first-order sigma-delta (73.6 dB, or 11.9 effective number of bits (ENOB)) is achieved for a range of $\pm 1\text{ }\mu\text{A}$ (230 Hz BW). The effect of the compensation circuit can be assessed through comparison of the results of a single electrode (Figure 4.2 a curve 4), of a single electrode with the compensation circuit turned on (curve 3), and of the results of 32 electrodes connected in parallel (curve 2). The larger the ratio of the double-layer capacitance to the reference capacitor value, the better is the performance. When 32 electrodes are connected in parallel, the SNDR increases by 15.3 dB compared to the case when only one electrode is connected. In the latter case, the

4 SYSTEM DESCRIPTION AND CHARACTERIZATION

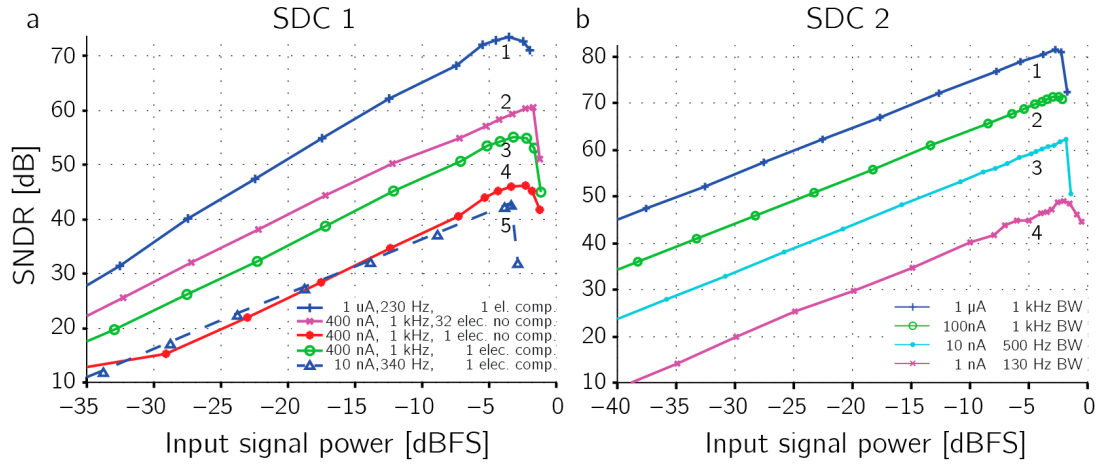


Figure 4.4: SDC electric characterization - (a) input signal power in dB of the full scale vs. signal-to-noise-and-distortion ratio (SNDR) of the 1st-order sigma-delta converter for $\pm 1 \mu\text{A}$ (1), $\pm 400 \text{ nA}$ (2, 3, 4) and $\pm 10 \text{ nA}$ (5) full-scale range under different conditions. (b) SNDR of 2nd-order SDC for $\pm 1 \mu\text{A}$ (1), $\pm 100 \text{ nA}$ (2), $\pm 10 \text{ nA}$ (3), $\pm 1 \text{ nA}$ (4) full-scale range.

First-order sigma-delta converter				
range	10 μA	1 μA	100 nA	10 nA
bandwidth	915 Hz	230 Hz	230 Hz	340 Hz
OSR*	1024	1024	1024	512
SNDR	71.3 dB	73.6 dB	63 dB	47.6 dB
ENOB	11.6 bit	11.9 bit	10.1 bit	7.6 bit
Second-order sigma-delta converter				
range	1 μA	100 nA	10 nA	1 nA
bandwidth	1 kHz	1 kHz	1 kHz	130 Hz
OSR*	256	256	256	256
int. RMS noise	250 pA	16.8 pA	3.2 pA	540 fA
SNDR	82 dB	72 dB	62.2 dB	49.1 dB
ENOB	13.3 bit	11.6 bit	10 bit	7.9 bit
Potentiostat				
slew rate	350 kV/s			
sweep rate	0-300 V/s			

Table 4.2: Electric characterization - performance summary of the circuit blocks. *oversampling ratio (OSR) was not a design criteria and is given for reference only.

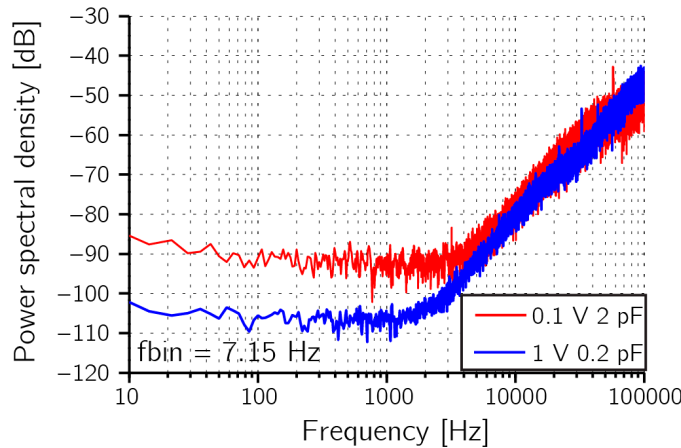


Figure 4.5: Noise considerations - For the same range settings, a smaller reference capacitor together with a higher reference voltage result in lower noise levels (see also Chapter 3)

SNDR can be increased by 9 dB upon turning on the compensation circuit. One channel consumes an area of $430 \times 200 \mu\text{m}^2$ and has a power consumption of 1.5 mW.

Second-order sigma-delta converter

The 2nd-order SDC achieves an ENOB of up to 13.3 bits for a 1 kHz bandwidth and a range of $\pm 1 \mu\text{A}$ full scale (see Figure 4.4 and Table 4.2). The integrated noise for the lowest range ($\pm 100 \text{ pA}$) is 220 fA within a bandwidth of 100 Hz ($21.5 \text{ fA}/\sqrt{\text{Hz}}$).

The noise considerations in Chapter 3 were verified. In Figure 4.5 the spectra of SD2 for a full-scale range of 93.8 nA at a clock rate of 468750 Hz is shown for two different combinations of reference capacitor and reference voltage. Use of the smaller reference capacitor (0.2 pF) in combination with the larger (1 V) reference voltage lowers the noise floor by about 10 dB , which is equivalent to an increase in SNR by 10 dB , as also predicted by Equation 3.9. One channel of the 2nd-order sigma-delta converter consumes an area of $650 \times 200 \mu\text{m}^2$ and has a power consumption of 1.9 mW.

4.1.4 Auxiliary circuit blocks

Several auxiliary circuit blocks are embedded on chip: reference voltages are provided for biasing, nine 10-bit segmented DACs are used to provide the reference voltages to the sigma-delta converters, the voltages for the potentiostat and for the working electrodes. All analog signals and reference voltages can optionally be supplied by external circuits.

32 external input pads can be connected to the readout channels. This allows for external sensors to be connected to the chip. For debugging and test purposes, two input pads can

4 SYSTEM DESCRIPTION AND CHARACTERIZATION

be connected to various locations on the chip. Voltage followers can be inserted into the signal path of the test channels to buffer the signal under investigation. Internal or external reference test currents can be applied to the readout channels and also scaled down by a factor of 10 or 100.

A rewritable 16-bit EEPROM is included, which can be used to store an identification number on the chip. Finally, a connection to a Pt-1000 resistor is provided as a means to monitor temperature during the experiments.

4.1.5 Digital interface

The connectivity of the switch matrix and all configuration settings are stored in SRAM cells (6T) on the chip. An SPI interface, clocked at 11.25 MHz, is used to program and read back the SRAM cells. The reference voltages are configured by the SPI interface and with a specific command loaded into all DACs simultaneously to allow for a synchronized change of the reference voltages for all channels.

The bitstreams of all 64 sigma-delta converters are time-multiplexed onto 4 pads. To avoid an additional pad for synchronizing the packet frame start, the bit of the first channel is toggled with the clock. Sampling on the rising and falling edge (double sampling) in the FPGA can detect this start condition and align the frame accordingly.

4.1.6 Full frame readout

Taking “electrochemical images” by reading out the whole array is a central feature of the system. It is realized by using the second-order sigma-delta converters in an incremental mode, i.e., upon conversion of one value the integrators are reset for the next conversion cycle. The currents from the whole array are read out column by column. Electrodes, which are not connected to the readout, can be left floating or can be kept at a different potential by connecting them to the 1st-order SDC. The fast digital interface is used to control the connectivity of the electrodes and reset of the ADCs. Reconfiguration of the whole array in order to switch from one column to the next and resetting the ADCs is achieved in 200 μ s, which is also the speed limiting factor of the frame readout. However, a frame rate for acquiring electrochemical images of up to 90 frames per second (fps) could be achieved.

4.1.7 Power consumption

The power consumption of the chip is summarized in Table 4.3. The measurements were performed by using PBS as an electrolyte and all electrodes turned on. Differences in simulated vs. measured values are due to discrepancies between assumptions for simulations and the real experiment. The major contributors to power consumption are the buffers to charge the reference capacitors in the case of using SD1, and the amplifier of the first integrator in

Block	Simulation	Measurement
quiescent current		15 mW
all DACs		13 mW
potentiostat*	380 μ W	1.7 mW
SDC1 per channel	1.7 mW	1.5 mW
SDC2 per channel	1.5 mW	1.9 mW
digital blocks		12 mW
all blocks on ⁺		165 mW

Table 4.3: CMOS chip power consumption - The different main blocks and their power consumption. * power consumption depends strongly on the load. ⁺ worst case scenario, used to determine the temperature rise of the sample liquid due to power dissipation.

the case of using SD2. The power consumption of the potentiostat depends strongly on the waveform applied, due to the class-AB output stage, and the actual load. The total power consumption is a worst-case scenario, i.e. all circuit blocks are turned on. The temperature during that operation in the liquid near the surface increased by only 0.5°C.

4.1.8 Discussion

All circuit blocks were successfully tested and show the expected performance. The potentiostat is stable under all loading conditions, and the capability to use the whole range of the 3.3 V power supply provides enough margin to work under higher load conditions, for example during the deposition of Pt black (see Chapter 7).

The 2nd-order sigma-delta converter has a much higher resolution and bandwidth, compared to the 1st-order SDC, owing to the better noise shaping (2.5 bit per doubling of the oversampling ratio (OSR) vs. 1.5 bit) and the active integrator structure. High resolution is required to reveal small signals embedded in a large background current.

The 1st-order sigma-delta converter can be used for measuring extremely high currents, i.e. functionalizing many electrodes in parallel (see Chapter 7).

Both current readout implementations can be used in parallel, for example to keep multiple electrodes passive — by applying a potential where no oxidation or reduction should occur —, while other electrodes are active in an electrochemical procedure or detection scenario (i.e. use of functionalized sensors), or to keep electrodes with one sigma-delta converter (SDC) polarized, while the others are read out by the other SDC. Both sigma-delta converter implementations together cover a range of 7 orders of magnitude.

Other implementations of fully integrated CMOS chips, with integrated microelectrode arrays (MEAs), for performing chronoamperometric measurements are listed in Table 4.4. The first five references (Schienle et al. 2004; Levine et al. 2008; Heer et al. 2008; Kruppa et al. 2010; Nazari et al. 2013) digitize the signals on-chip. However, they do not take advantage of the possibility of taking electrochemical images of the whole array. In order to compare the

Reference	Array	Material	Pitch	Range	LOD*	Resolution	max. BW*	Frame rate	Power
Schienenle et al. (2004)	16 × 8	Au	300 μm	1 pA - 100 nA	1 pA				
Levine et al. (2008)	4 × 4	Au	N/A	100 pA - 250 nA	550 pA	9 bit eff.			
Heer et al. (2008)	24 × 24	Pt	100 μm	10 nA - 10 μA	1 pA	11 bit eff.	1 kHz		25 mW
Kruppa et al. (2010)	24 × 16	Au	120 μm	100 pA - 100 nA		12 bit nom.			102 mW
Nazari et al. (2013)	10 × 10	Au	200 μm	24 pA - 350 nA	24 pA	8 bit eff.	1 kHz		18 mW
Inoue et al. (2012)	20 × 20	Au	250 μm	100 pA - 100 nA	1 pA	N/A	55 Hz	5 fps	630 mW
Kim et al. (2013)	10 × 10	Pt	35/50 μm	20 pA - 400 nA *		N/A	2 kHz	40 fps	
Bellin et al. (2014)	5 × 2 × 6	Au	N/A	70 nA - 70 μA	240 pA	N/A	1 kHz		
this work	32 × 32	Pt	100 μm	100 pA - 10 μA	1 pA	13 bit eff.	1 kHz	89 fps	165 mW

Table 4.4: Comparison table - fully integrated electrochemical CMOS chips with embedded microelectrode array. The first five references include the ADCs on-chip. However, no full frame readouts are shown. The implementations with external ADCs perform full frame readouts at a maximum of 40 fps. * can only handle oxidative currents. (* LOD limit of detection, BW bandwidth)

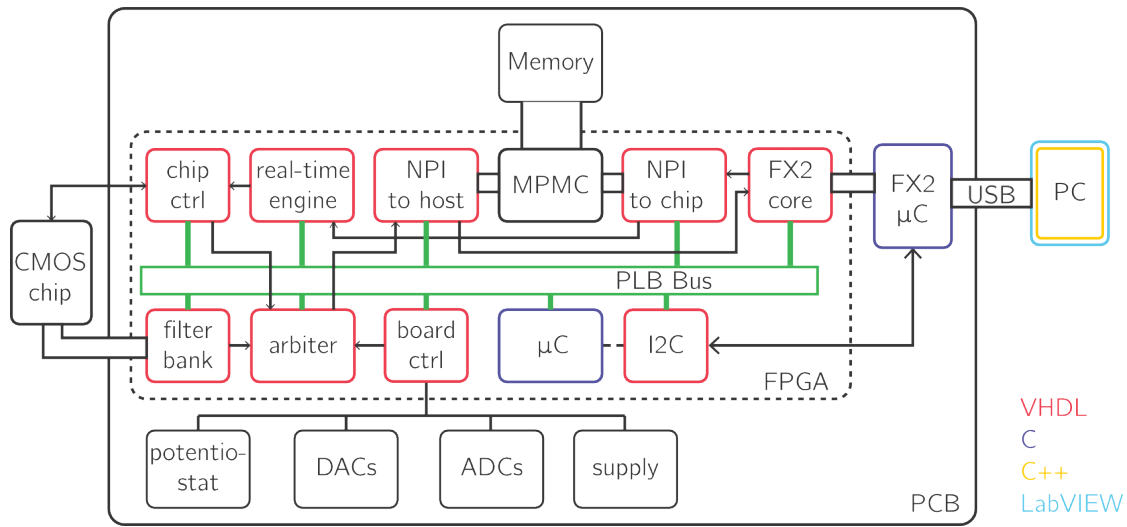


Figure 4.6: FPGA and circuit board - The red boxes in the FPGA (inside dashed line) are custom peripheral cores (pcores), which are connected to a bus and controlled via an embedded microcontroller (μ C; microblaze Xilinx). They perform filtering, data buffering and framing, real-time control of the CMOS chip, data transmission to the USB chip (Cypress FX2) and control of the circuits blocks on the PCB. An external 1 GB memory is attached to the FPGA and used to buffer the data via a native peripheral interface (NPI) and the multi-port memory controller (MPMC, Xilinx).

"imaging" feature to other designs, implementations without embedded ADCs were added to the table (Inoue et al. 2012; Kim et al. 2013; Bellin et al. 2014).

The design featured in this work showed the largest dynamic range, competitive noise limits and the fastest frame rate. Among the chips with embedded ADCs it has the highest effective number of bits.

4.2 FPGA AND CIRCUIT BOARD

The control of the CMOS chip, the signal processing of the acquired data, and the communication with a computer are performed by a custom PCB with a Spartan 6 (Xilinx) FPGA micromodule (Trenz Electronic). The main building blocks of this setup are shown in Figure 4.6. The FPGA design is centered around a soft microcontroller (microblaze Xilinx), which has access and control of the main bus (PLB). The firmware on the microcontroller handles direct commands from the PC via an interrupt engine. Peripheral cores (pcores) are attached to the main bus and perform different tasks: (i) demultiplexing and filtering of the sigma-delta bitstreams, (ii) framing and buffering the data (iii) timed control of the CMOS chip and the circuitry on the PCB, (iv) monitoring the correct functioning of the CMOS chip.

4 SYSTEM DESCRIPTION AND CHARACTERIZATION

4.2.1 Decimation filters

A filter bank on the FPGA is used to decimate the bitstreams of the 64 sigma-delta converters. In normal mode the bitstream of a channel is first filtered by a cascaded integrator-comb filter (CIC) (Hogenauer 1981) and subsequently by an exponential moving average filter (EMA) (R. G. Lyons 2010). The filter characteristics and the order of both filters are variable and can be adapted to the bandwidth requirements.

Cascaded integrator-comb filter

The CIC decimation filter is a hardware-efficient multirate filter, built of a cascade of integrators and of differentiators, separated by a sampler. The difference equation of a single stage without downsampling and the transfer function of a N -th order CIC filter can be expressed as:

$$y[n] = x[n] - x[n - M] + y[n - 1] \quad H(z) = \left[\frac{1}{1 - z^{-1}} \cdot (1 - z^{-RM}) \right]^N \quad (4.1)$$

where y is the output, x the input, n the current state of the variable and $n - 1$ the previous state of the variable. The decimation ratio is R , the order N and the differential delay of the filter is M . The frequency response for a 3-rd order decimating CIC filter with a differential delay of $M = 1$ is shown in Figure 4.7 a.

The cascaded integrators will overflow, because of the unity feedback at each integrator stage. The overflow is without any consequence if the number system used can wrap around (i.e. two's complement) and if the number of bits is large enough to handle the expected magnitude at the output of the filter (Hogenauer 1981).

The magnitude, respectively the gain G , and the number of bits B needed are given by:

$$G = (RM)^N \quad B = N \log_2(RM) \quad (4.2)$$

Due to sampling, side bands are aliased into the baseband of the filter response (colored curves in Figure 4.7 a). Reducing the bandwidth by another filter can decrease the level of the aliased noise: assuming a CIC filter of order $N = 3$, and a differential delay of $M = 1$, a passband of $f_{bw} = 1/16$ of the decimated sample rate will increase the image attenuation to 81 dB.

Exponential moving-average filter

The EMA filter can be implemented to perform filtering without multiplications (in contrast to common FIR and IIR filters) by using shift and add operations. This is achieved by having a filter coefficient of a power of 2. The difference equation of a single stage moving averager and the transfer function are:

$$y[n] = 2^{-s} \cdot x[n] + (1 - 2^{-s}) \cdot y[n - 1] \quad H(z) = \frac{2^{-s}z}{2^{-s} - 1 + z} \quad (4.3)$$

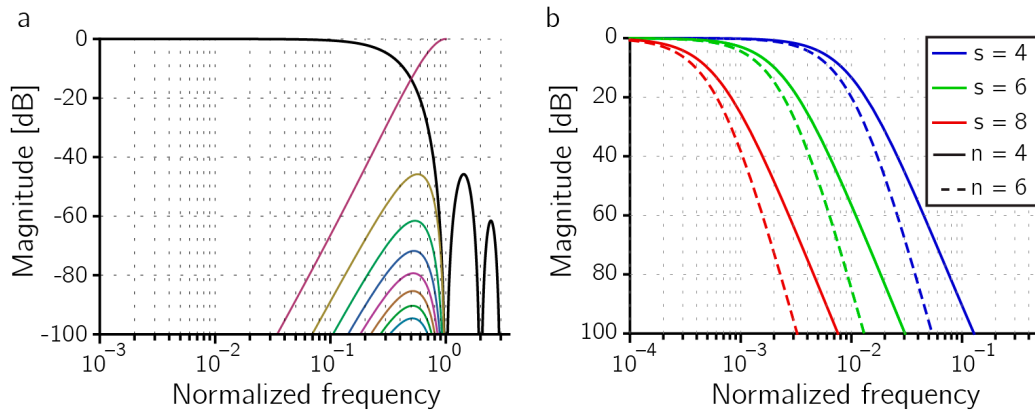


Figure 4.7: Decimation filter characteristic - (a) Frequency response of a 3-rd order CIC filter with differential delay $M = 1$. Frequency is normalized to the slow clock. Colored curves depict the sidebands aliased back into the baseband. (b) Frequency response of a 4-th and 6-th order EMA filter for different shift factors. Frequency is normalized to the sampling frequency.

where s is the shift factor. The frequency response for 3 different shift factors ($s = 4, 6, 8$) and two different orders ($n = 4, 6$) are shown in Figure 4.7 b (frequency normalized to the sampling clock).

Having both filters in series, the EMA filter can be used to avoid the anti-aliasing problem of the CIC filter.

To reduce the noise, the bandwidth of the two filters can be further reduced. Also if a lower bandwidth is sufficient for a certain experiment (which is often the case in amperometry) the data rate can be reduced drastically. However, a decimation filter of one order higher than the order of the sigma-delta converter is sufficient for filtering the bitstream (Schreier and Temes 2004). This is utilized for the fast filter mode (i.e. for fast electrochemical techniques like FSCV or DPV see Chapter 6), where 32 CIC filters of third-order with a fixed decimation rate of $R = 128$ and a differential delay of $M = 1$ are used to decimate the bitstream. Consecutive decimated values can be averaged by a sum and shift operation, i.e. to get the mean value. The number of averaged values is fixed to a power of 2, in order to compensate for the gain by a shifting operation. The implemented filters can decimate the bitstream continuously, or in incremental mode (i.e. for acquisition of the whole array) reset after one output value from a sequence of bits is processed.

4.2.2 Real-time engine

To be able to produce arbitrary waveforms, timed configuration changes and to provide a timestamp for the data packets, a global clock with a resolution of $1 \mu\text{s}$ is employed. The real-time engine has access and control of all features of the CMOS chip and the circuits on

4 SYSTEM DESCRIPTION AND CHARACTERIZATION

the PCB. The clock controls the fast acquisition of measurements from the whole electrode array: initialization of the ADCs to start the conversion, definition of the connections in the array and filtering of the acquired data.

4.2.3 Data communication

The measurement system relies on USB 2.0 to communicate with the PC. The fast data path from the PC to the real-time engine passes the USB microcontroller (Cypress FX2) via a parallel interface and is buffered in the RAM attached to the FPGA. The real-time engine collects newly arrived data and waits for the time point of execution. A slower control command path uses I2C to communicate with the embedded microcontroller on the FPGA and can be used independent of the real-time engine. The fast data path from the FPGA to the PC is using an arbiter (round-robin) to pass arriving packets from the two filters, from the real-time engine and from ADCs on the PCBs to the memory for buffering. The fast data paths uses direct memory access. It allows the data packets to bypass the microcontroller, so that the transmission rate is independent of the current processor load. The packets are transmitted to the PC as soon as memory space is available.

4.2.4 Discussion

The rather elaborate design of the measurement setup evolved over time to cope with new requirements: increasing acquisition speed and better filtering, which required more resources of logic gates and memory. To even out the differences in data generation and transmission via USB, a buffering of the data in the large external memory was necessary. The fast array readout was made possible by the real-time engine and the fast filters.

The design of the measurement setup enabled to apply additional experimental techniques and to conduct experiments in a reliable and repeatable manner. Since the whole measurement setup is compact, it can be placed in a small desktop incubator. The setup is powered via USB, and experiments can be performed without additional equipment.

4.3 SOFTWARE

The driver to communicate with the FX2 USB chip is based on the open-source library libusb, which is cross-platform compatible. The driver was deployed as a library (a dynamic link library on a Microsoft Windows platform and a framework on Mac OS X) and can be loaded and accessed by LabVIEW (National Instruments). The raw data are directly stored on the hard disk by the library for highest performance.

The main program to control the experiments and to visualize the data is realized in LabVIEW by using an object-oriented approach. The LabVIEW program allows for direct configuration of all functions of the measurement setup. Experimental protocols can be assembled

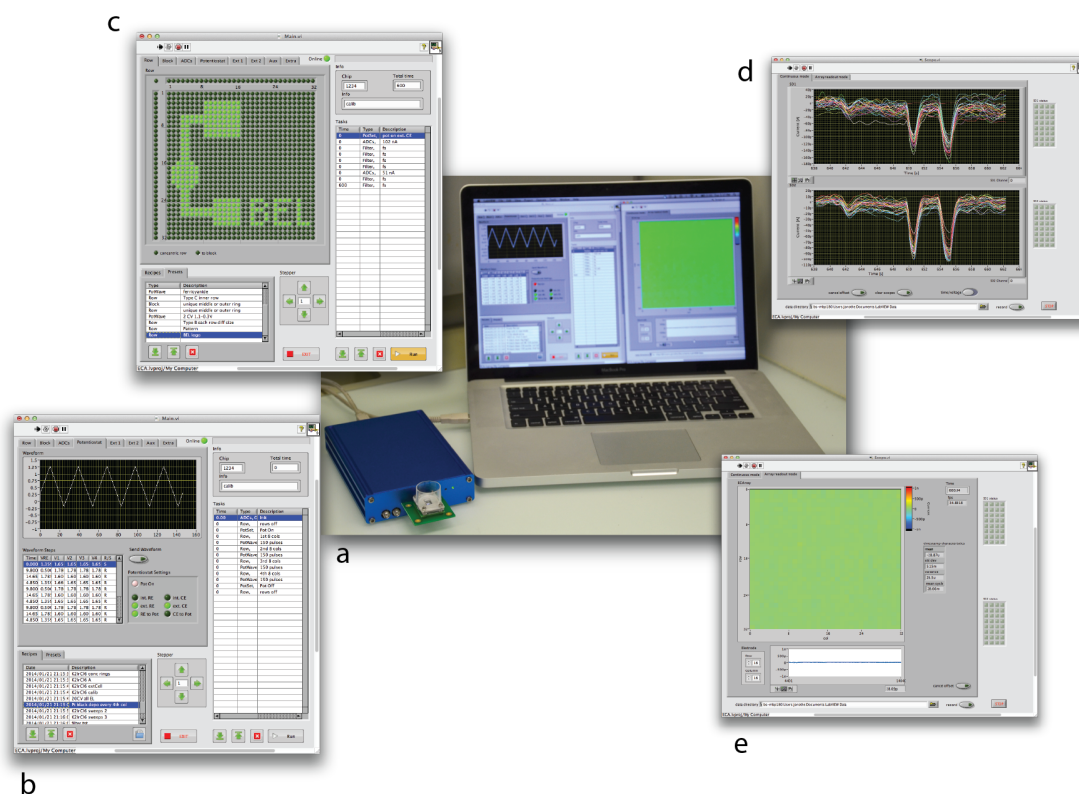


Figure 4.8: Measurement Setup - (a) Picture of the CMOS chip assembly, plugged into the measurement system with acquisition laptop. (b-e) Screenshots of the software suite: (b) controlling the potentiostat for cyclic voltammetry, (c) configuring the connectivity, (d) 64 ADC channels in continuous mode and (e) image of whole array to visualize the measurement data.

by adding configuration states and the time of execution to a list. This list can be stored, loaded and executed. When an experiment is started, the protocol is sent to the FPGA, and the real-time engine controls the timed execution.

Direct visualization of the measurement data is crucial during experiments and is provided for different measurement techniques. A picture of the measurement setup, together with some screen shots of the running software, can be seen in 4.8. Raw data, together with the configuration settings, are saved on disk and can be imported into Matlab (MathWorks) for later data analysis.

The software suite allows for a flexible and automated control of the measurement setup during an experiment. Data and chip settings are seamlessly transmitted between the different tools for control, recording and data analysis. The object-oriented implementation provides a robust basis to adopt new features.

5

MICROFABRICATION AND PACKAGING SOLUTIONS

One problem of using CMOS technology is the limited selection of materials that are compatible with the processes and that some of the CMOS materials (e.g., aluminum metallization) are not compatible with biological matter. Metal pads of the standard CMOS process are made of non-noble metals, like copper and aluminum, which are neither compatible with biological applications nor usable for electrochemical methods. The CMOS chips must be post-processed in order to be viable for accommodating wet cell or tissue samples (Hierlemann and Baltes 2003) and to provide electrode materials, which are suited for electrochemistry. Electrode materials suited for electrochemistry are noble-metals, like gold or platinum, glassy carbon or diamond (Huang et al. 2009). The fabrication process has to be compatible with the CMOS technology, i.e. temperatures need to be low enough ($< 400^{\circ}\text{C}$) in order not to destroy the chip by mechanical stress due to different thermal expansion coefficients of different materials. Standard microfabrication techniques have been developed for this purpose, such as Ti/Pt/Au stacks deposited and structured via lift-off techniques (Thewes 2007), or plasma-enhanced vapor deposition of silicon oxides and nitrides, followed by sputtering of Pt to realize electrodes (Franks et al. 2005).

An alternative approach is electrodeposition (Huang et al. 2009) or electroless deposition (Hwang et al. 2009) of noble metals. Screen printing techniques may be a viable option for depositing materials like carbon paste on CMOS chips (Huang et al. 2009).

Another obstacle one has to face is that once the electrode fabrication problem is solved, the rest of the CMOS chip also needs protection against the biology and wet chemistry as well as connections to external equipment (such as a laptop) for readout or to drive or power the chip. The CMOS chip and system packaging should be reliable and straightforward and yield a system that is compact and simple to use. Additionally, some measurement techniques may need containers for liquids, sophisticated fluid handling in the form of microfluidics, or external electrodes.

This chapter will highlight the efforts in the design and fabrication of the electrodes, the developed packaging methods, and ideas to provide wells for hosting cells.

The post-CMOS fabrication of the platinum electrodes was developed by our cleanroom engineer Alexander Stettler.

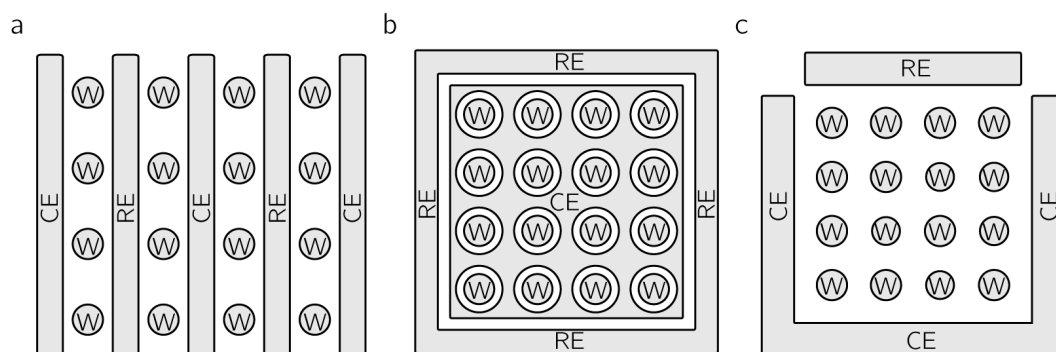


Figure 5.1: Reference and counter electrode placement - (a) reference and counter electrode distributed in the array, (b) working electrode array surrounded by a large counter electrode, (c) array surrounded by counter electrode, reference electrode at the top.

5.1 ELECTRODES FOR ELECTROCHEMISTRY

The post-processing concept enables a high flexibility in the layout of the electrodes that are located on top of the switch matrix. The possibility to vary the electrode sizes and layout renders the device suitable for a multitude of applications and enables to study how the specific electrode area determines the recorded signals.

5.1.1 Counter and reference electrodes

To provide a self-contained system, the counter or auxiliary electrode (CE) and the reference electrode (RE) have to be included on the CMOS chip. The working principle of a potentiostat has been described before (see Chapter 2 and 3). The potential of the working electrode is set with respect to a reference electrode, which is in dynamic equilibrium (no net current) with the electrolyte. If current is flowing through the working electrode (WE), the CE has to supply that current. Initially the current can be provided by non-faradaic charging currents of the CE ($I = C_{CE}dV/dt$). However, after some time, the voltage will reach a value, where side reactions will take place at the CE. In aqueous systems, if there is an oxidation reaction at the WE, it is most likely that dissolved oxygen will be reduced at the CE. If the electrodes are in close proximity, the products of the CE reaction can diffuse to the working electrode and might interfere with the WE reaction.

Separating the counter electrode from the working electrodes might not be necessary for voltammetric experiments, like cyclic voltammetry, where the time scale of the experiment limits the size of the diffusion layer (see Chapter 2). Moreover, by using a counter electrode with a large area and capacitance, the currents at the working electrodes can be provided by the charging currents of the counter electrode without reaching excessive voltages. This not only limits the side reactions, which can occur, but also reduces the requirements on the

voltage range that the potentiostatic circuit has to provide.

These considerations lead to two design decisions: (i) the counter electrode should be large with respect to the working electrodes, and (ii) it should preferably be spatially separated from the working electrodes.

Different design options are shown in Figure 5.1. The first option (Figure 5.1 a) places REs and CEs in between the WE array to provide the same distances between the different electrode types. The design requires the electrodes to be internally connected to a common potentiostat. To maximize the area of the CE, another option is shown in Figure 5.1 b. However, as mentioned above this positioning could lead to interferences on the WEs, if long time scales are involved (i.e. amperometry). Trying to separate the CE from the array while keeping a large size is the idea of the design in Figure 5.1 c. The design of Figure 5.1 c is realized on the fabricated chip: a CE which is 14 times larger ($7489300 \mu m^2$) than the area of all WEs together is located in 200 μm distance to the array together with a RE of $594875 \mu m^2$ in area. To maximize the area of the CE, the design in Figure 5.1 b has also been realized (see also the pixel layout in Figure 5.2 e), however, it has not been tested up to now.

The positioning and the size of the reference electrode is not so crucial: the currents are small, and the conductivity of the solution will not lead to a significant Ohmic drop (see also Chapter 3). More important than position is stability of the RE. If the electrode potential of the RE changes during an experiment or between experiments, a proper measurement is no more possible. This instability can be avoided by using an external standard reference electrode (Ag/AgCl/KCl 3M), which was done for most of the experiments. A platinum pseudo reference electrode has been placed atop the array, which can be used in cases for which external electrodes cannot be used, like in the case of using a microfluidic compartment.

In experiments, where the CE could be contaminated by side reactions an external CE was used.

5.1.2 The array of working electrodes

The array of working electrodes has been designed in different layout versions. The only limitation is imposed by the underlying switch matrix of the CMOS chip, to which the electrodes have to be connected, via the pad opening of the CMOS process. In one design an array of 32×32 equal-sized electrodes of 25 μm diameter has been arranged to yield a large array of so-called ultra-microelectrodes (Bard and Faulkner 2001). This is the standard design used for electrochemical images. Another design includes electrodes with different diameters ranging from 5 to 50 μm in blocks of 4×8 electrodes (Figure 5.2 c), to explore applications, where the optimum electrode size is not known *a priori*. To test the effect of the CE surrounding the WEs, a third design was fabricated (see Figure 5.2 e). The electrodes in all these layouts have a center-to-center distance of 100 μm . To monitor cell cultures or cell spheroids, three large concentric electrodes were designed, where the inner two electrodes feature the same area, and the outer, much larger electrode can serve as a CE or RE.

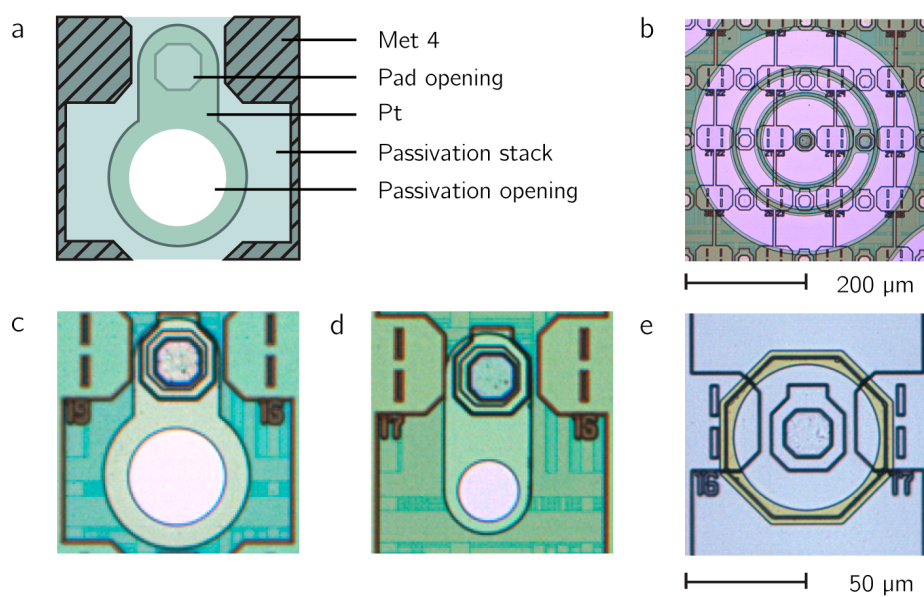


Figure 5.2: Working electrode pixel layouts - (a) Pixel layout: Met 4 is the top metal layer of the CMOS process; the pad opening provides the connection to the underlying switch matrix; platinum serves as the electrode material; the active electrode area is defined by an opening in the passivation layer stack. (b) Three concentric electrodes, the inner two have the same area and are suitable for generator-collector experiments, (c) 40 μm electrode, (d) standard 25 μm electrode, (e) WE on top of pad opening; all surrounded by the CE (see also Figure 5.1 b).

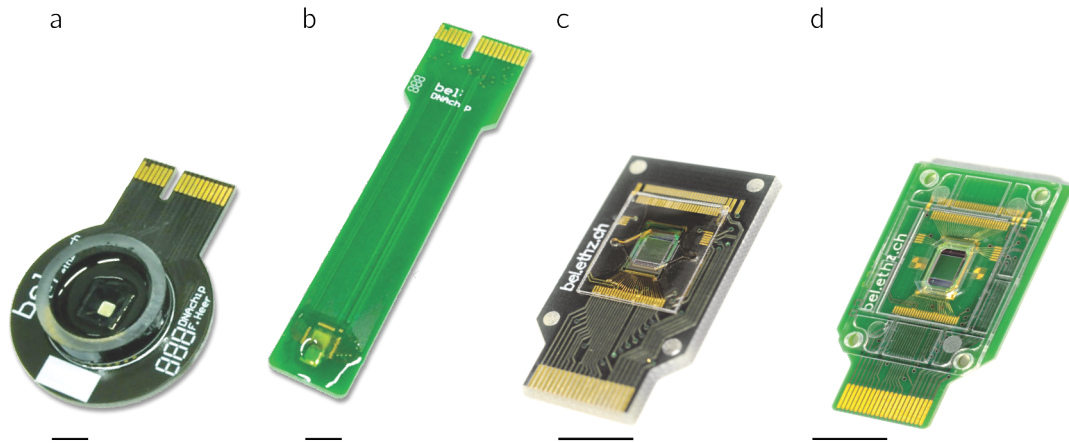


Figure 5.3: Package variations - (a) a glass ring is glued on the PCB, the array is protected by a PDMS stamp, while epoxy is poured on the chip, (b) light curing epoxy is manually deposited around the array opening and cured under UV light, (c) thick layer of SU-8 covers PCB and chip assembly and was structured by photolithography, (d) injection-molded polycarbonate package is glued onto the CMOS chip and the PCB.

5.1.3 Electrode fabrication

The platinum microelectrodes have been patterned on the chips during a wafer-level post-processing in house. First, a SiO_2 passivation layer has been deposited over the whole wafer. Reactive-ion etching has been used to re-open the connection pads. An adhesion layer of WTi (50 nm) and the platinum layer (270 nm) have been deposited and structured through ion-beam deposition and ion-beam etching processes. Finally, a thick (1.6 μm) passivation stack, consisting of SiO_2 and Si_3N_4 has been deposited on top of the wafer and has been structured by reactive ion etching to open the active areas of the electrodes (see Figure 5.2). This top passivation layer is not only used to shape the electrodes but also protects the CMOS circuitry from corrosion. Additional protection is achieved by shifting the electrode openings in the passivation layer away from the openings in the CMOS aluminum pads.

5.2 PACKAGING SOLUTIONS

Packaging is one of the most underestimated challenges in the system design process. Packages for CMOS chips that are in contact with solution and biological matter have to provide protection to the chips and bond wires, must be bio-compatible and may not harm the cells, and they must withstand all sorts of chemicals and be long term stable. The packaging process should be simple and straightforward.

5.2.1 Package variations

Several packaging options for different applications were implemented (see Figure 5.3). For all packages, the CMOS die is glued on a custom-made PCB and connected with bond wires. The whole assemblies are plugged into a card-edge connector for a reliable but easily reversible electric connection.

The traditional way of packaging is shown in Figure 5.3 a: a glass ring is glued on the PCB, subsequently a bio-compatible epoxy (Epotek 302-3M) is poured on the chip, while the array is protected by a PDMS stamp. Finally, the PDMS stamp is removed after the epoxy has cured. This method is efficient, since many chips can be packaged in parallel. However, sometimes leakage occurs due to bad adhesion of the epoxy to the chip surface. Residues from the silicone in the PDMS stamp may lead to contamination of the electrodes and to subsequent non-uniform layer deposition. The package shown in figure 5.3 b can be used to dip the whole array into a vial. It is prepared by manually depositing light-curing epoxy (Epotek Pb 604) around the array over the bond wires and by subsequent curing under UV light. The process is not very effective and needs a skilled operator, but the contamination problem of the PDMS stamp can be avoided.

Figure 5.3 c relies on photolithographic techniques to pattern the package. The latest development relies on an injection molded polycarbonate package, which is glued onto the CMOS chip and the PCB (see Figure 5.3 d).

In the following paragraph the schemes of the last two package variations are explained in more detail.

5.2.2 Packaging procedure

The packaging scheme based on photolithography is depicted in Figure 5.4 a. The single dies are glued into a recess of the PCB and wire-bonded. The photolithographic process is done in the cleanroom. Four PCBs are glued on a dummy wafer in order to be able to use standard cleanroom equipment. A 250- μm -thick layer of photoresist (SU-8) is spun on top. A low spinning-speed (<1000 rpm) is used to achieve the desired thickness and has to be used as the dummy wafer assembly is not balanced. A mask aligner and a photomask are used to precisely structure the package.

The advantage of this scheme is that the packaging process is performed in a very clean environment with little probability of contamination. Second, the process involves no manual handling, hence, the resulting packages are very reliable. The scheme can be adapted to new requirements: upon designing a new mask, new features can be implemented, i.e. fluidic channels can be embedded into the packaging layer (see Figure 5.6 a). One problem is the adhesion of SU-8 to the PCB: delamination of the layer on the PCB was observed in some instances so that a pretreatment of the PCBs was required. Spin-coating on an uneven surface creates a non-uniform layer of photoresist. In addition, the whole process is very time consuming and parallel processing of many chips is not really possible.

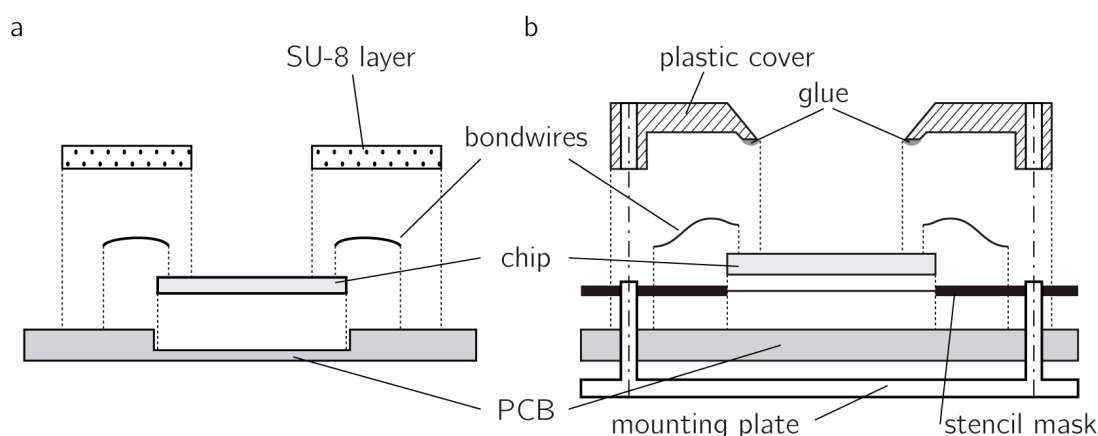


Figure 5.4: Packaging procedures - (a) The CMOS die is glued into a recess on the PCB, the chip is connected via bond wires, a 250 μm -thick layer of SU-8 is applied and structured to protect the bond wires and to have an opening for the array. (b) The die is glued onto the PCB by using a mounting plate and a stencil mask, the chip is connected via bond wires, an injection molded polycarbonate package is glued atop the array using the mounting plate.

PCB, CMOS chip and package have to be aligned with each other. In the scheme described above, this alignment is achieved by a recess in the PCB and by alignment marks on the CMOS chip. Another approach was chosen in the scheme shown in Figure 5.4 b: (i) the PCBs are aligned on a mounting plate with poles by using the mounting holes of the PCB; (ii) a stencil mask (which normally is used to apply solder paste to a circuit board) with openings for the dies is placed on top; (iii) the dies are placed into the openings and glued to the PCB; (iv) the stencil mask and the PCBs are removed from the mounting plate, and the chips are wirebonded; (v) the assemblies are placed again on the mounting plate, and an injection molded polycarbonate package is glued onto the array and the PCB by using the same mounting holes as for the PCB.

Using the mounting plate, 15 chips can be packaged in parallel in one afternoon. The only step where care has to be taken is the application of the glue to the rims of the plastic package which touches the array. This package was found to be most reliable. Polycarbonate material is inert to many chemicals (also acids or oxidants, not acetone) and biocompatible. The packages already provide some space for a small liquid volume, which is sufficient for some applications (i.e. cleaning). The volume can be increased by attaching various auxiliary packages like beakers or fluidic systems to the assembly, by using the mounting holes of the assembly (see Figure 5.5 a).

For precise alignment to external equipment a guiding rail is used (see Figure 5.5 b).

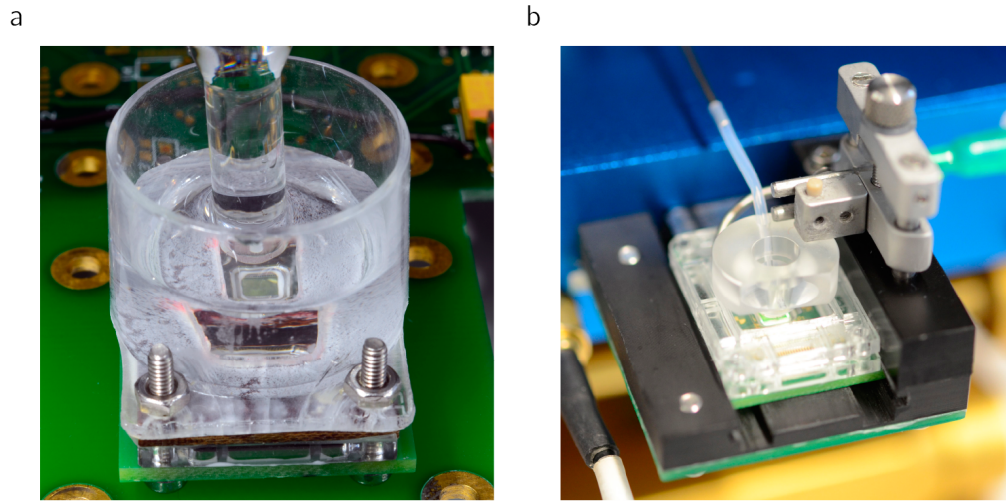


Figure 5.5: Accessories - Various additional items can be used with the system: (a) beaker for increased sample volumes, (b) fixture for biological tissue with included perfusion system for oxygenation.

5.3 MICROFABRICATION

Microfabrication can not only be used for packaging, but also to realize fluidics onto the chip. Large channels have been fabricated for a flow-through system (see Figure 5.6 a) and small wells for hosting cells (see Figure 5.6 b and c). To be able to monitor secreted substances of cells, cells should be located above a sensing electrode. The cells should stay immobilized even if a perfusion system is used at the same time. For hosting the cells, microwells were fabricated on top of the electrodes by applying and structuring a 10- μm -thin layer of photoresist (SU-8). The wells have a diameter of 20 or 50 μm with a volume of 3 or 20 pL. Diffusion of secreted molecules is confined by the wells, and the confined volume will lead to detectable concentrations. Figure 5.6 (c) shows a section of the array with single yeast cells loaded into the cavities above the microelectrodes. This has been achieved by pipetting cells suspended in media onto the array. The cells simply drop into the wells by gravity. Due to the high number of microelectrodes available and the highly flexible routing scheme, laborious spotting for single-cell trapping can be avoided by applying a defined concentration of cells in suspension.

5.4 DISCUSSION

The post-processing allows for addition of noble-metal electrodes onto the CMOS chip. The layout of the electrodes can be easily adapted for new applications.

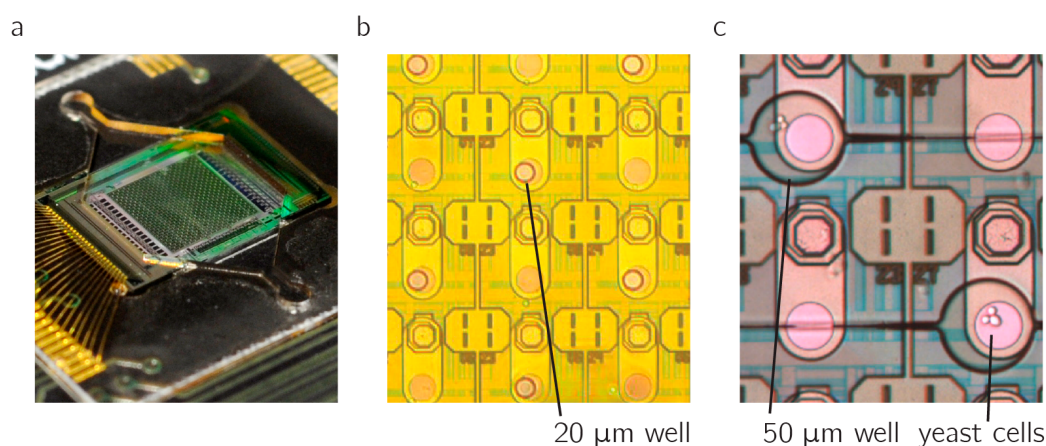


Figure 5.6: Microfabrication - (a) Fluidic channels can be embedded in the package by using photolithography. (b) Wells to host the cells are formed with a 10 μm -thin layer of SU-8. (c) Close up of working electrodes with wells hosting yeast cells.

The final packaging scheme by using injection-molded parts provides a longterm biocompatible package, which protects the electronics against the harsh biological and chemical liquid environment. The packaging procedure is robust and many chip systems can be packaged in parallel. Other approaches based on wax, PDMS, photoresist, epoxy, parylene, crystal adhesive, or a combination of these materials have been used (Hassibi and Lee 2006; Inoue et al. 2012; Kruppa et al. 2010; Li et al. 2011).

By using microfabrication techniques, fluidic channels or wells for hosting cells can be built. Such wells are suitable, for example, for amperometric detection of single chromaffin cells (Liu et al. 2011).

6

MEASUREMENT TECHNIQUES AND ELECTROCHEMICAL CHARACTERIZATION

All electrochemical measurements in the following chapters were acquired and all techniques were applied solely with the developed measurement system. Besides a standard Ag/AgCl reference electrode no external equipment has been used.

This chapter begins with a short explanation of different electrochemical techniques. Then, these techniques are applied to characterize the performance of the CMOS chip.

6.1 ELECTROANALYTICAL TECHNIQUES

6.1.1 Amperometry

In amperometry a potential is applied to the working electrode (WE) versus a reference electrode (RE), and the current at the WE is measured over time. The current is a result of electrochemical reactions at the working electrode. The faradaic current is limited by the mass transport rate of ions to the electrode and the considerations of diffusion limits apply (see Section 2.3.3): for a planar electrode the current will decrease over time; for a disk microelectrode the current will reach a certain steady-state value; for a microelectrode array, the current will reach similar current values as for the steady-state of a single microelectrode, until the diffusion layers of neighboring electrodes overlap, at which point in time the currents will decrease, in analogy to the case of a planar electrode. The current is, in most cases, linearly proportional to the concentration of the electroactive species in the solution. Amperometry has a very good time resolution, since the measured current is directly the resulting signal. However, amperometry is limited in selectivity: if reactants with redox potentials lower than that of the target ion or lower than the applied potential are present, their redox currents will contribute to the overall signal. To increase selectivity, size-discrimination layers, e.g. non-conducting polymers, or ionophores can be applied (see Chapter 7).

Enzymatic biosensors are common amperometric sensors, where the biosensitive layer is in close contact with the electrode (Ronkainen et al. 2010). The product of an enzymatic reaction is obtained directly above the electrode and can then be oxidized or reduced without having to diffuse across large distances. This proximity to the electrode alleviates the issue of time dependent currents due to diffusion limitations on microelectrode arrays.

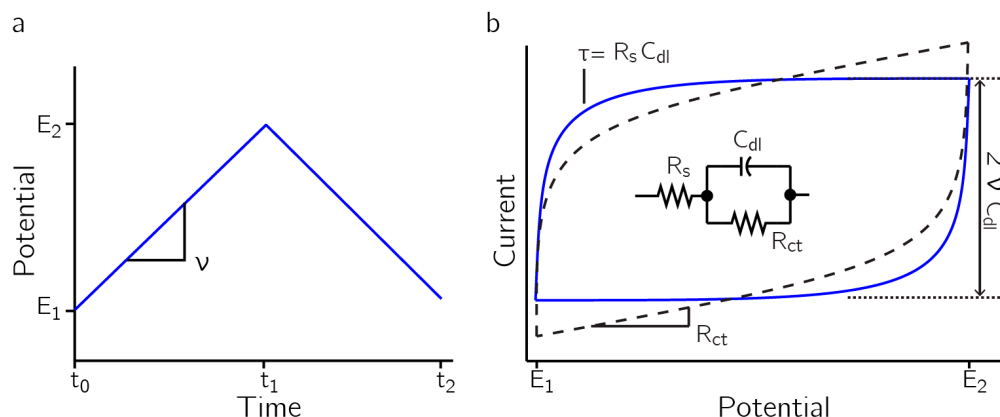


Figure 6.1: Cyclic voltammetry - (a) voltage ramp applied to the electrode arrangement with sweep rate ν (b) cyclic voltammogram: current vs. potential curve and correlation of curve features with elements of the equivalent circuit of an electrode in an electrolyte.

6.1.2 Cyclic voltammetry

In cyclic voltammetry the voltage imposed on the WE and RE is swept in a triangular fashion (see Figure 6.1 a), and the current is then measured. The result is a cyclic voltammogram (CV), where the current is plotted versus the voltage (see Figure 6.1 b). Sweep rates (ν) are in the range of 10 mV/s to a few 100 mV/s for standard CVs, and faster than 100 V/s for fast-scan cyclic voltammograms (FSCVs) (Heien et al. 2004). The endpoints of the sweeps are chosen below levels, where bulk electrolysis occurs, i.e. hydrogen/oxygen evolution in aqueous systems. General features of the CV can be explained by a simple equivalent model of the electrode-electrolyte interface (see also Section 2.3.6): (i) Non-faradaic charging of the double layer (DL) is the reason for the separation of the currents in the forward and the backward sweeps, since $I = C \frac{\partial V}{\partial t} = C \cdot \nu$. (ii) The charging and discharging of the DL capacitance C_{dl} follows an exponential behavior (the time constant is $\tau = R_s C_{dl}$), since the capacitance is charged via the uncompensated solution resistance R_s . (iii) A resistive current through the charge transfer resistance R_{ct} may add to the capacitive charging currents (dotted line in Figure 6.1 b). However, the charge transfer resistance is not necessarily constant.

If a redox couple is present in the solution, initially, at low voltages, the faradaic current will be small; upon surpassing the reduction potential, the current will peak; at high enough potentials diffusion will be limiting and lead to a reduction of the current. Microelectrodes at sufficiently slow sweep rates do not show the peak, since the steady state current is reached rapidly, due to radial diffusion (compare to Section 6.2.1). Adsorption and desorption of molecules will also add to the signal, hence, the simple model including only a charge transfer resistance cannot explain all features present in CVs.

The advantage of cyclic voltammetry, compared to amperometry, is that multiple analytes can be distinguished according to differences in their redox potentials. Thus, the method can be more selective than amperometry. Due to the background current from charging and discharging of the DL, a higher dynamic range is needed to acquire the signal. The bandwidth is lower than in amperometry, since a complete sweep has to be performed to acquire one sample of the signal.

Fast-scan cyclic voltammetry

In fast-scan cyclic voltammetry, sweep rates of 100 V/s and faster are applied. These high scan rates can provide better temporal resolution, allowing for measurements of changes in neurotransmitter levels and exocytosis in real-time (Wightman 2006).

Figure 6.2 a shows a voltammogram acquired with bright platinum electrodes of different diameters in PBS at a sweep rate of 100 V/s. The increasing background current, i.e., the non-faradaic current from charging the DL capacitance, for larger electrodes can be seen. In Figure 6.2 b a proof-of-concept measurement to detect dopamine was performed. At a sweep rate of 100 V/s different concentrations of dopamine were added to the solution. A clear oxidative peak at the limit of the CV at 0.6 V and the corresponding reductive peak at ~ -50 mV can be seen. Clearly, for proper measurements, the cycling parameters have to be tuned, and an adequate electrode functionalization has to be employed, to reduce cross-sensitivity to other electro-active compounds present in solution (see Section 7.3.5).

Nevertheless, the capabilities of the system can be assessed. The maximum sweep rate, which can be achieved is 300 V/s.

It is evident that a large dynamic range and high resolution are required to detect small changes in the signal accompanied by the large background current. The high sweep rates require sufficient speed and bandwidth in all levels of the measurement system: the DACs have to provide the waveforms, the potentiostat has to control the voltage and the current readouts, and the decimation filters need to be fast enough and synchronized to the applied waveform.

6.1.3 Pulse voltammetry

Pulse voltammetry is similar to cyclic voltammetry in the sense that the voltage is swept across a certain range. In pulse voltammetry, however, pulses of certain duration and height are used to sweep over the potential window of interest. In differential pulse voltammetry (DPV), after an induction period, a forward pulse of width t_{pulse} and height E_{pulse} is followed by a reverse pulse of the same height minus the step height E_{step} . The currents are sampled during a defined time at the end of the forward and reverse pulses (compare to red and black marks in Figure 6.3). A differential current is determined by subtracting the response of the reverse pulse from the response of the forward pulse.

Square wave voltammetry (SWV) is a special form of DPV, where the pulse waveform is a

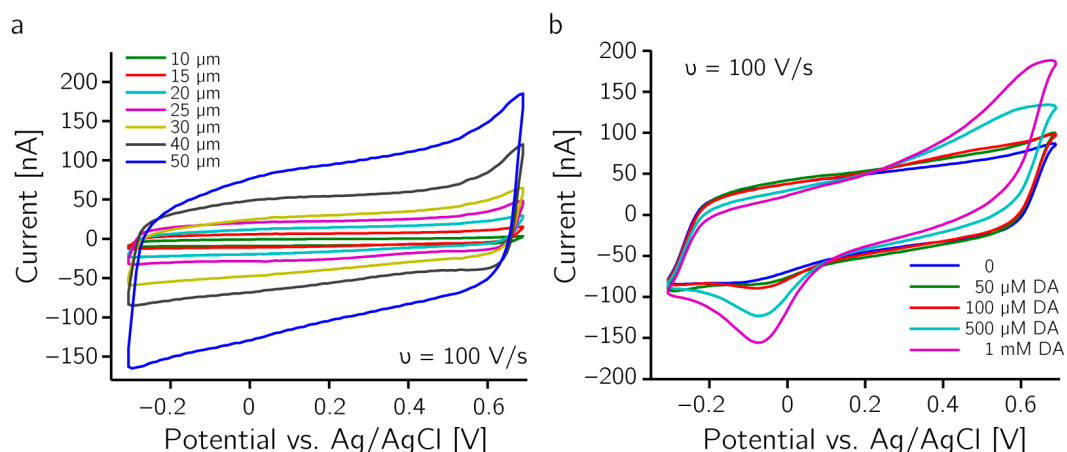


Figure 6.2: Fast-scan cyclic voltammetry - CV in PBS, sweep rate 100 V/s. (a) Non-faradaic currents of electrodes of different sizes. (b) Detection of dopamine on bright Pt electrodes.

square wave (pulse width=pulse period/2). If an electroactive molecule is present, which can be oxidized and reduced upon a sweep, the forward pulse will cross the formal reduction potential first, and, therefore, generate a higher current, than the reverse pulse. Hence the differential current will show a positive peak, which increases with increasing potential. When the potentials of the pulses reach a diffusion limiting regime, the currents of forward and reverse pulses cancel each other, and the peak in the differential current will disappear (see also Figure 6.4).

The pulse height is proportional to the concentration of the analyte and the area of the electrode. Figure 6.4 shows the response of different-sized electrodes to the presence of the redox couple ferridyanide(III)/(IV) ($\text{Fe}(\text{CN})_6^{3-} + e^- \rightleftharpoons \text{Fe}(\text{CN})_6^{4-}$). The pulse width was $t_{\text{pulse}} = 100$ ms, the pulse height was $E_{\text{pulse}} = 43.7$ mV, the step height was $E_{\text{step}} = 5.5$ mV, and the period of one double pulse was 273.4 ms (for a sweep rate of 20 mV/s). The currents were sampled during the last 10% of the pulse widths before the end of each pulse (compare to Figure 6.3 a).

Through sampling of the currents at the end of the pulse, after the charging of the DL, background currents can be effectively suppressed.

Compared to cyclic voltammetry, pulse voltammetric techniques need a larger dynamic range to cope with the charging currents during the pulses. They exhibit a selectivity similar to cyclic voltammetry, but can provide a lower limit of detection as compared to cyclic voltammetry (Mann et al. 2014). However, pulse voltammetric techniques require precise control and synchronization of current readouts and applied voltage wave forms.

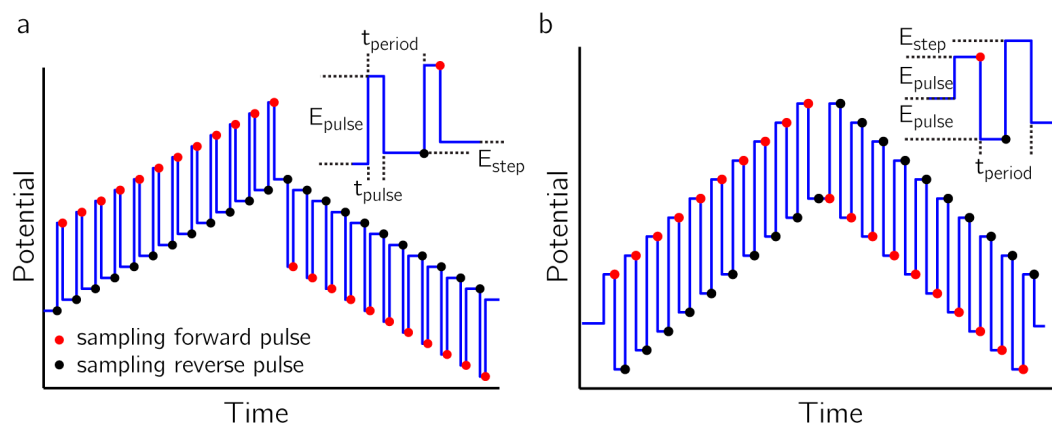


Figure 6.3: Pulse voltammetry schemes - (a) cyclic DPV voltage waveform; DPV would only include an upward or downward ramp. (b) cyclic SWV;

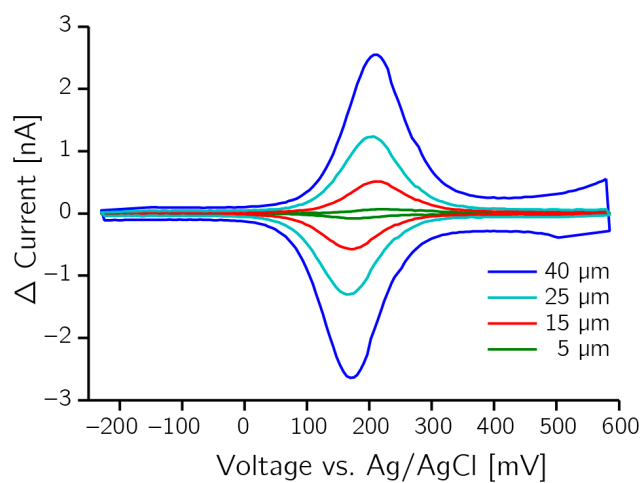


Figure 6.4: CDPV of $\text{Fe}(\text{CN})_6$ - Response of electrodes of different sizes to 1.4 mM potassium ferricyanide(III) in PBS, pulse width $t_{\text{pulse}} = 100$ ms, pulse height $E_{\text{pulse}} = 43.7$ mV, step height $E_{\text{step}} = 5.5$ mV, sweep 20 mV/s (period 273.4 ms). Currents were sampled in the last 10% of the pulse widths before the end of each pulse.

6.1.4 Galvanostatic methods

In galvanostatic methods, a constant current is applied, and the voltage is measured. Galvanostatic methods are commonly used for electrodeposition, where it is important to provide a constant current density, they are less common an electroanalytic tool.

On the CMOS chips, galvanostatic methods can be realized by operating the current readouts in saturation: the current is limited by the full-scale range, which can be delivered from the DAC in the sigma-delta loop. To reach saturation, the potential of the working electrode has to be chosen in a range, where the desired reaction will happen and where the potential is large enough to produce the desired current density. The potential of the working electrode is not kept at the preset potential.

In the case of SD1 the only difference to normal operation is the constant decision process of the comparator in a hopeless attempt to bring the voltage of the working electrode back to the preset value. In the case of SD2 the amplifier of the first stage will quickly go into saturation and will not be able to maintain the input at virtual ground anymore. The voltage will drift to whatever value results from applying the current to the electrochemical cell. That is exactly the function of a galvanostat: to apply whatever voltage is needed to provide a constant current.

The galvanostatic mode has been successfully used for electrodeposition of gold. However, the results of galvanostatic deposition schemes on the large array were not satisfying with respect to layer uniformity and reliability. Hence, a different deposition scheme was developed, as can be seen in Chapter 7.

6.1.5 Bipotentiostat

Bipotentiostatic experiments are used to establish different electrochemical regimes (two applied electrode potentials) on two working electrodes. It is used in ring-disk setups and also can be used to conduct generator-collector experiments.

The chip can be used as a multipotentiostat, which can simultaneously provide four separate electrochemical regimes (four different electrode potentials plus reference potential), by the ability to set the voltage not only of the reference electrode, but also specifically for different WEs or sets of WEs.

In this work, the multipotentiostatic feature was used to keep electrodes in a passive electrochemical regime, whilst other electrode were functionalized (see Chapter 8).

6.2 ELECTROCHEMICAL CHARACTERISTICS OF THE MICROELECTRODES

In this section some key electrochemical characteristics of the measurement system are presented. All experiments were performed by using the measurement system together with an external standard Ag/AgCl/KCl (3M) reference electrode.

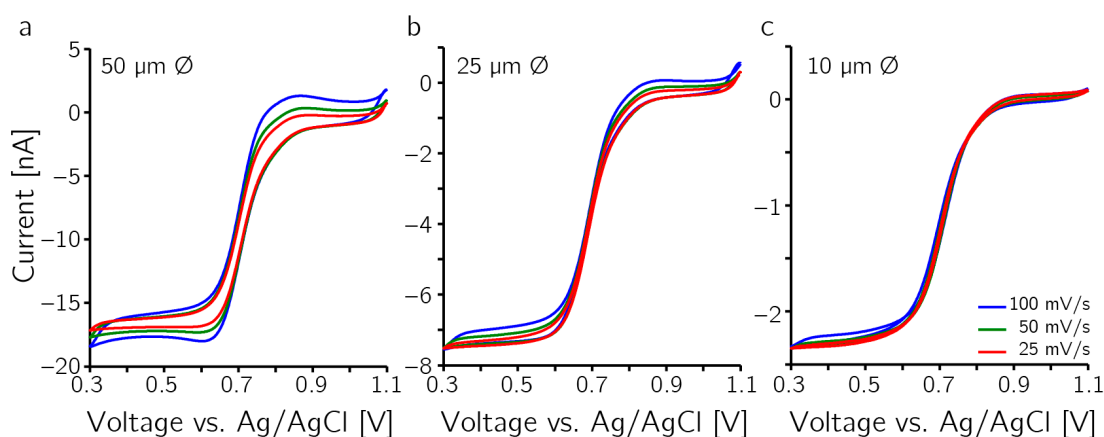


Figure 6.5: Ultra-microelectrodes - cyclic voltammogram of a redox couple: 1.6 mM K_2IrCl_6 in 0.1 M KNO_3 . Corresponding voltammograms from a (a) 50 μm , (b) 25 μm , and (c) 10 μm diameter electrode have sigmoidal shapes, which are characteristic for ultra-microelectrodes. At the large 50- μm electrodes (a) a peak due to planar diffusion starts to form for using sweep rates > 25 mV/s.

6.2.1 Redox couple

Electrodes in the range of tenths of micrometers are called ultra-microelectrodes (Bard and Faulkner 2001). However, there is no general definition what the characteristic dimensions of ultra-microelectrodes are. At ultra-microelectrodes a time-independent stationary state is reached very rapidly, as soon as the current due to radial diffusion dominates over the current due to quasi-planar diffusion (see Chapter 2 and Heinze (1993)). Small electrodes and slower scan rates will have a sigmoidal-shape current response due to radial diffusion, which are characteristic of ultra-microelectrodes: larger electrodes or faster scan rates will show a peak-shape CV due to planar diffusion.

The hexachloroiridate(IV)/hexachloroiridate(III) redox couple ($\text{IrCl}_6^{2-} + e^- \rightleftharpoons \text{IrCl}_6^{3-}$) was used, and CVs were performed on electrodes having a diameter of 10 μm , 25 μm and 50 μm (see Figure 6.5, Petrovic (2000)). For the two smaller electrodes the CV had the sigmoidal shape for all applied scan rates. The CV on the large 50- μm electrode starts to develop peaks at scan-rates faster than 25 mV/s.

The steady-state current (which is reached below 0.5 V vs. Ag/AgCl) is proportional to the radius, the concentration and the diffusion coefficient, according to Equation 2.11. The proportionality to the concentration could be seen, however, the dependence on the radius was proportional to $r^{1.23}$. The discrepancy may be a consequence of the small recess (~ 1.6 μm) of the microelectrodes, which entails a different diffusion regime as assumed by Equation 2.11 (compare to Bond et al. (1988)).

In summary, the characteristics of ultra-microelectrodes can be observed for all realized

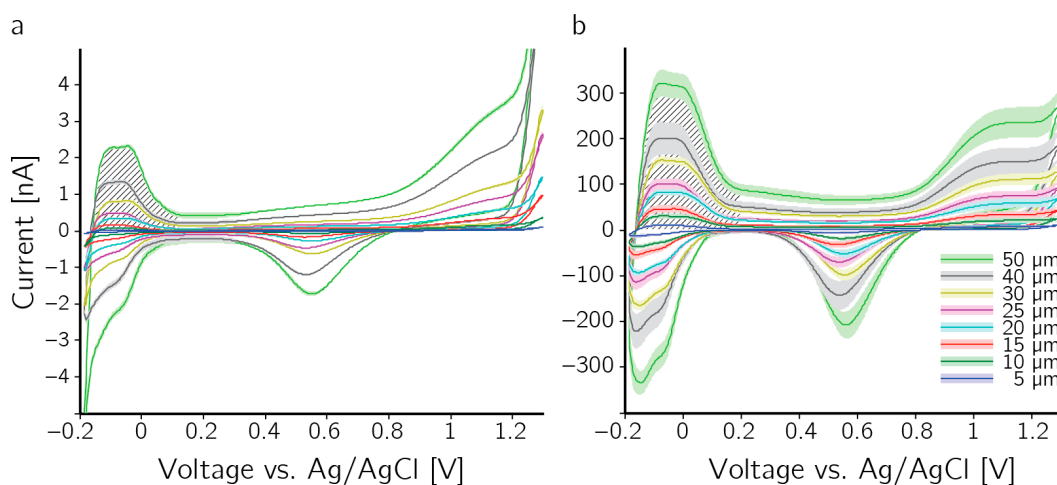


Figure 6.6: Surface properties - Cyclic voltammograms in 1 M H_2SO_4 at 100 mV/s sweep rate. (a) Bright platinum electrodes, (b) after deposition of Pt black. Hatching marks the areas used to calculate the microscopic surface area.

electrode diameters, as long as the scan rates for the largest electrodes are limited to 25 mV/s.

6.2.2 Surface properties

One possibility to increase signal-to-noise ratio on the sensing side is to modify the surface (see also Chapter 7). The surface of an electrode has a geometric area due to the dimensions and a microscopic area, which includes the real area including all surface roughness. Increasing the true or microscopic area increases the area for possible charge-transfer and increases the capacitance due to the DL (i.e. lowers the impedance). However, in a diffusion limited scenario, increasing the microscopic area will not increase mass-transport.

Figure 6.6 shows cyclic voltammograms in 1 M H_2SO_4 for bright platinum electrodes of different electrode diameters (Figure 6.6 a) and for electrodes modified with Pt black (Figure 6.6 b). The CVs show the characteristic features of a polycrystalline platinum electrode in H_2SO_4 ; the buildup of adsorption layers of oxygen and hydrogen, as well as their removal, and bulk solution electrolysis. The CVs do not show any indication of contamination resulting from metals (Al, Cu) of the CMOS layers.

The microscopic (true or active) electrode area was determined from the charge needed to remove an adsorbed monolayer of hydrogen atoms. It was determined by integrating the current in the corresponding region of the CV (hatched area in Figure 6.6) and by subtracting it from the current needed to charge the double-layer capacitance. The true area is given by a characteristic charge of $208 \mu\text{C}/\text{cm}^2$ (Doña Rodríguez et al. 2000).

An equivalent radius was calculated from the microscopic area, which would be the radius of

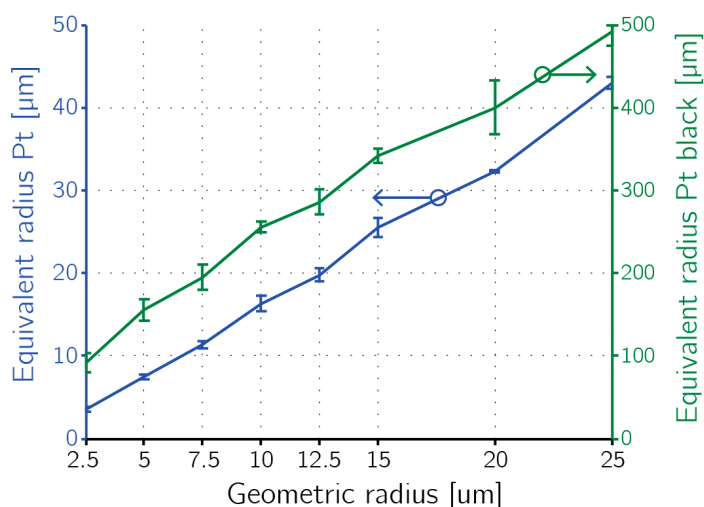


Figure 6.7: Microscopic area - Geometric vs. equivalent radius of the electrode, calculated from the microscopic area as determined in Figure 6.6. The equivalent radii of bright Pt electrodes relate to the ordinate at the left; those of electrodes with Pt black to that at the right.

an equivalent electrode with a perfectly smooth surface. It is plotted in Figure 6.7 for bright platinum electrodes (left ordinate) and electrodes modified with Pt black (right ordinate) for comparison.

The roughness factor is determined by the ratio of the microscopic area to the geometric area. For bright platinum electrodes the mean roughness factor was 1.97 ($n=32$, $\text{std} = 0.29$). The uniformity of the bright platinum electrodes, evidenced by the roughness factors, shows the precision of the microtechnological process steps and allows for performing reproducible measurements.

Electrodeposition of Pt black, on the other hand, increases the active area by a factor of >100 for the large, $50\text{-}\mu\text{m}$ diameter electrodes, and a factor of >400 for the small, $5\text{-}\mu\text{m}$ diameter electrodes. The mean roughness factor, where Pt black was deposited, is 540, however, with a standard deviation of 267 ($n=32$). The increase in roughness factor is not uniform, when different-size electrodes are functionalized with the same protocol, which has to be taken into account and requires calibration measurements.

6.3 CIRCUIT IMPLEMENTATIONS AND ELECTROCHEMISTRY

6.3.1 Comparison of the current readout circuits

As two different circuits were implemented to acquire and digitize the current, the question arises, if both circuits perform as required in electrochemical experiments.

To compare the different readout circuits in different modes, CVs in $0.5\text{ M H}_2\text{SO}_4$ were

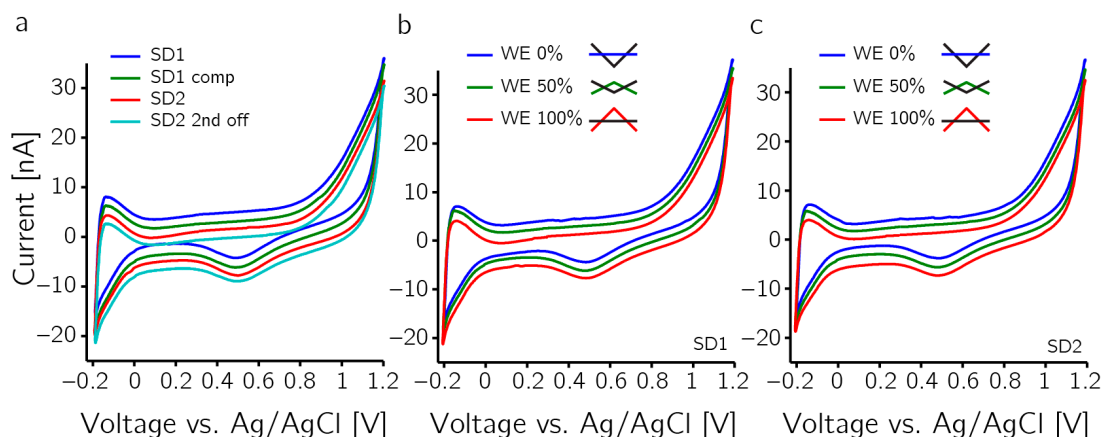


Figure 6.8: SD1 vs. SD2 - CVs on 32 bare 25-μm electrodes in 0.5 M H₂SO₄ with a sweep rate of 100 mV/s. (a) comparison of SD1, SD1 with compensation turned on, SD2 and SD2 with the second stage disabled. (b,c) sweep performed by varying the voltage of the WEs. For WE 0% the sweep is performed solely by varying the voltage of the RE; at WE 100% solely by varying the voltage of the WEs; and for WE 50% both voltages are varied. CVs for SD1 shown in (b), for SD2 in (c) (a-c) The different traces are offset by 2 nA for better visibility.

performed (-0.2 – 1.2 V vs. Ag/AgCl 100 mV/s sweep rate). To reduce possible effects from individual electrodes, 32 electrodes of each row were connected in parallel.

In Figure 6.8 a, the corresponding CVs acquired while using the first-order sigma-delta converter (SD1), SD1 with the compensation circuit enabled, the second-order sigma-delta converter (SD2), and SD2 with the second stage disabled, are shown. For better visibility the curves are offset by 2 nA each.

To achieve a large voltage range, a differential voltage sweep can be performed, which does not only later the voltage of the RE but, at the same time, also the voltages of the WEs (see Chapter 3). In Figure 6.8 b and c, the effect of varying the voltage of the WE was investigated. The traces show the response for the case, when the sweep is performed by only varying the potential at the RE (WE 0%), by only sweeping the potential of the WE (WE 100%) and by sweeping both differentially at half the amplitude each (WE 50%).

All curves overlap, and no major differences, besides variations as a consequence of performing the measurements sequentially, can be seen.

Especially in the case of SD1, where the electrode-electrolyte interface is used as a circuit element, the same electrochemical response can be elicited, and the same gain can be provided, as in the case of a conventional sigma-delta converter. The compensation circuit of SD1 was not required in this case, since many electrodes were connected in parallel, however, the signal and the electrochemical reaction were also not degraded or modified due to enabling the compensation circuit. Even though the two implementations (i.e. SD1 and SD2) are comparable in the electrochemical response, they still feature the electronic differences in

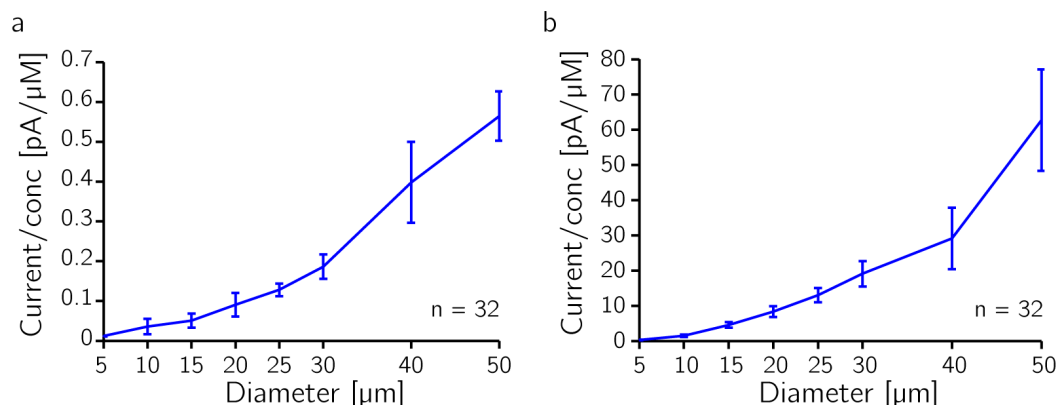


Figure 6.9: Polarized vs. floating electrodes - Sensitivities to H_2O_2 concentration for different electrode diameters, determined by calibration measurements. (a) Electrodes are constantly polarized. (b) Fast multiplexing mode, electrodes are not connected (i.e. floating) in-between readouts.

resolution and bandwidth.

Finally, varying the voltage of the WE did not have a detrimental influence on the voltammogram. The voltage variations did neither change the charge of the reference capacitors in the digital-to-analog converter (DAC) of the sigma-delta converters, nor did they influence the acquired current as a consequence of variations of the virtual ground in SD2. In summary, the current readout circuits performed as intended.

6.3.2 Polarization of electrodes - multiplexing effects

To read out the whole array of the chip, the electrodes are read out column by column. In slow mode, all electrodes are connected to SD1; the column, which is read out, is switched to the other readout circuit (SD2). Hence, the electrodes are polarized at all times.

In fast mode, all electrodes are floating, and only one column is polarized by SD2 during readout. If the duration of one acquisition cycle is short enough, the potential of the electrode stays constant.

The difference in both modes was investigated in a calibration measurement by using H_2O_2 (see Figure 6.9). Different concentrations (0, 10, 100, 1000 μM) of H_2O_2 were measured in slow mode (i.e. all electrodes polarized at the same potential at all times), and the sensitivity was evaluated (Figure 6.9 a). Figure 6.9 b shows the response due to different concentrations (0, 5, 25, 100, 400 μM) acquired in fast mode at 17.5 fps (57 ms).

The sensitivity while having floating electrodes is approximately 10 times higher, compared to the case, where the electrodes are polarized continuously.

It could be argued, that the longer acquisition time in the slow mode is responsible for a reduced current, since diffusion limits as specified by the Cottrell equation (see section 2.3.3) apply. And indeed, Cottrell conditions ($1/\sqrt{t}$) could be seen, when looking at the

sum of the currents. However, the acquisition is automated, and the currents per column are acquired at the same time for each concentration. Hence, when the sensitivities are determined from subsequent calibration steps, the time as a factor in the Cottrell equation ($1/\sqrt{t}$) is eliminated.

Nonetheless, the reason for the elevated current upon having floating electrodes between readouts, can be found in the diffusion effects: When an electrode is connected, the reactant is converted and the concentration at the electrode reaches zero very quickly. As soon as the electrode is disconnected from the current readout, no more reactant is consumed and the diffusion layer can be replenished. At the same time, the electrode potential starts to deviate from the requested potential. In the next cycle, the electrode potential is re-applied, and the reactant that diffused to the electrode, when disconnected, can be converted and adds to the faradaic current.

This explanation would also explain the increase in current, when longer periods (i.e. lower frame rates) are used.

However, the limitations of this effect and the electrochemical implications are currently not fully understood and need further investigation.

The effect of an elevated current could be advantageous for biosensors, where usually the enzyme is the rate limiting factor (see Chapter 8). The analyte is pre-concentrated during the time, when the electrodes are floating, and a higher signal can be achieved.

6.4 DISCUSSION

The CMOS microsystem can be used to apply various electrochemical techniques, e.g. amperometry, voltammetry, differential-pulse voltammetry, square-wave voltammetry, bipotentiostatic techniques and basic galvanostatic techniques.

The electrodes in the array show electrochemical characteristics of ultra-microelectrodes. The active surface of the microfabricated electrodes is highly uniform and allows for performing reproducible measurements.

Consistent electrochemical results are obtained with all implemented readout circuits in all operation modes. Fast multiplexing in combination with having floating electrodes between readout cycles can be used to achieve larger signals.

7

ELECTRODE FUNCTIONALIZATION

The microtechnological process yields uniform and well defined platinum microelectrodes, which themselves are suitable for performing basic electrochemical methods. However, the properties of the platinum microelectrodes may not be suitable for many sensing applications. Key properties of microelectrode surfaces include: (i) to provide a large active surface area for better charge-transfer and higher signals; (ii) to serve as a substrate for accommodating biomolecules like enzymes to build biosensors; (iii) to allow for other molecules to be anchored; (iv) to act as a size discriminating or anti-interference layer to reduce cross-sensitivity; or (v) to obviate electrode fouling.

These surface properties can be realized by functionalization of the electrodes.

The requirements on the functionalization scheme for a microelectrode array are more stringent than for a single sensor: (i) Functionalization must be robust, such that it can be performed reliably on all electrodes. (ii) Spatial control is crucial, as non-specific deposition will interfere with the measurements. (iii) Deposited layers have to be uniform on the array to allow for comparable measurements of single sensors. (iv) The layer thickness should be controllable, since other parameters depend on it (i.e. response time, enzyme loading). (v) The deposition method should be robust against electrode size variations in order to be useful for parallel deposition and various designs. Finally (vi), the functionalization scheme should be applicable to different types of layers. In the quest for finding a method, which can be used to deposit a functional layer while meeting the aforementioned criteria, several deposition schemes were tested on the electrode array.

Many biologically relevant molecules are non-electro-active, thus, detection schemes have to be employed to make the analyte accessible to electroanalytical methods. One possibility is to use enzymatic biosensors, which convert the analyte of interest to an electro-active molecule.

Biosensors, based on the enzyme family of oxidases, catalyze the reaction of a specific analyte (i.e. choline, glucose, lactate) to H_2O_2 . Hydrogen peroxide can be readily oxidized on the platinum electrode (by applying a potential of 0.65 V vs. Ag/AgCl), and two electrons participate in the faradaic current. The resulting current is proportional to the concentration of the analyte.

There are many methods for immobilization of enzymes on electrodes (Hanefeld et al. 2009). The method must retain catalytic activity for extended time and must provide precise spatial control of the immobilization over the array, to avoid cross-sensitivities.

7 ELECTRODE FUNCTIONALIZATION

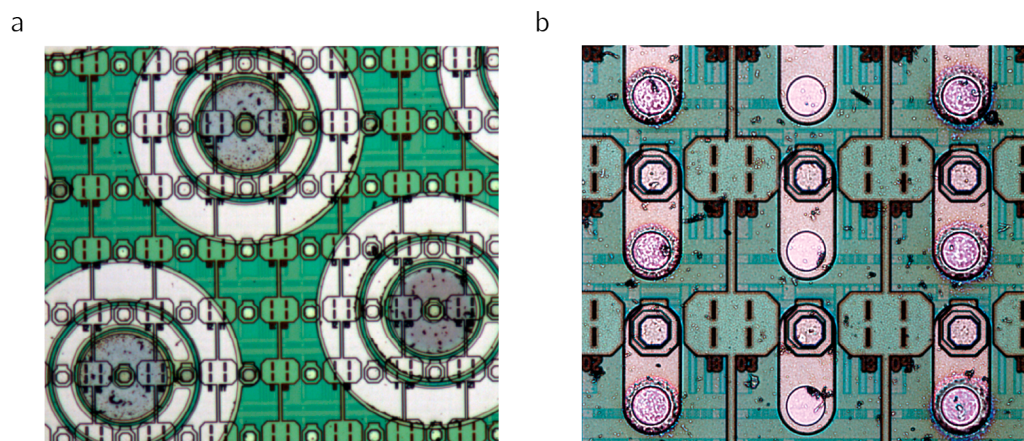


Figure 7.1: Electrochemically aided adsorption - (a) The inner electrodes (135 μm radius) of the concentric ring electrodes were functionalized by electrochemically aided adsorption of lactate oxidase to detect lactate. (b) Picture of a 25- μm electrodes after use. The left and right columns were functionalized to detect choline. The middle column was kept empty to check for selectivity and crosstalk.

This chapter describes the efforts spent on functionalization of the electrodes and fabrication of sensitive layers to detect biomolecules.

7.1 DROP COATING

Drop or dip coating is used to embed a biosensitive element into a matrix immobilized on the surface of the electrode. The method involves pipetting a self cross-linking mixture onto the sensors and letting it cure.

The method is easily applicable, however, spatial control is poor. Very precise low volume dispensing equipment is needed to reach a controlled and reproducible deposition. The uncontrolled deposition of enzymes results in different sensitivities of the sensors and in comparably thick layers. Thick layers result in long response times of the sensor, due to restricted diffusion of the analyte to the electrode (compare to Section 8.2.1). Slow response times are only acceptable for applications involving slow changes of the analyte concentration during measurements.

7.2 ELECTROCHEMICALLY AIDED ADSORPTION

Better spatial control can be achieved by a technique called electrochemically aided adsorption (EAA) (Johnson 1991). An enzyme in solution with a pH greater than the isoelectric point (PI) will possess a negative charge. The enzyme is pulled to and immobilized on the

surface of an electrode, if the electrode is positively charged. The immobilization can be combined with the cross-linking of the enzymes. Glutaraldehyde is an organic compound, which cross-links proteins. The cross-linking agent only starts to cross-link when protein concentrations are high enough. Hence, the immobilization will be specific to the electrodes, where the concentrations are highest. An example of EAA is shown in Figure 7.1. A mixture of an oxidase (e.g. lactate oxidase to detect lactate, choline oxidase for choline), bovine serum albumine (BSA) and glutaraldehyde was pipetted onto the array and cross-linking was initiated by applying a train of 25 pulses, each pulse consisting of 3 s at 1.8 V followed by 6 s at 0.4 V (= open circuit potential of Pt vs. Ag/AgCl). The remaining deposition solution was removed from the surface of the array, and the chip was rinsed and dried.

In Figure 7.1 a, the inner disk electrode (135 μm radius) of the concentric-electrode design was functionalized to detect lactate. The deposition was restricted to the area of the electrode.

Figure 7.1 b shows the scheme applied to small 25- μm electrodes for the detection of choline. The left and right columns were functionalized to detect choline, the middle column was left empty to check selectivity and cross-talk. The enzyme layer is mainly located atop the electrode opening. Electrically aided deposition enhances cross-linking at the electrodes, but does not restrict cross-linking to the area of the electrodes, hence, deposition outside the electrode area can occur. EAA enables in only limited control over the layer thickness: the concentrations of the cross-linking agent and the proteins have to be tuned, and the time for cross-linking has to be adapted for each case.

7.3 ELECTRODEPOSITION

Electrodeposition is the method of electrochemically depositing a compound on an electrode. Materials suited for electrodeposition are, e.g., metals and polymers. Polymers, allow for co-immobilization of other molecules by entrapment within electropolymerized layers or by covalent binding to these layers (Vidal et al. 2003).

Electrodeposition features good spatial control, since the deposition is restricted to the surface of the electrode, where current can flow. The deposited mass, and consequently the layer thickness, is related to the applied total charge through Faraday's law. Common methods for electrodeposition include galvanostatic methods through applying constant voltages, and performing cyclic voltammograms (CVs). In galvanostatic methods, the current is fixed to achieve a certain current density, and therefore a certain deposition rate. The current has to be adjusted in order to provide the desired current density for a certain deposition area. If the exact area is unknown or if deposition should be achieved on differently sized electrodes, the application of the method pose a challenge and has to be adapted for every scenario. Voltage-based (potentiometric) deposition methods are independent of the deposition area.

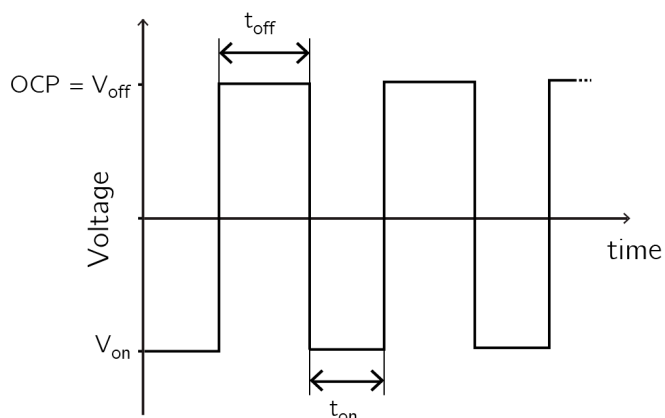


Figure 7.2: Voltage-pulse based deposition scheme - Pulse shape for cathodic deposition of, e.g., Au or Pt black. During t_{on} the deposition potential E_{red} is applied, during t_{off} the electrodes are brought back to the original open-circuit potential. For oxidative deposition reactions the polarities have to be reverted.

7.3.1 Voltage-pulse based deposition scheme

For robust and uniform functionalization, a general electrodeposition scheme has been developed that can be easily adapted to modify the sensing surface by spatially controlled patterning of two key classes of molecules, namely metals, such as Pt black and gold, and polymers, such as poly(3,4-ethylenedioxythiophene) (PEDOT) and poly(phenylenediamine) (PPD).

Before use, the microelectrodes were electrochemically pretreated by scanning the electrode potential for 32 cycles between -0.2 and +1.2 V vs. Ag/AgCl in a 0.5 M H_2SO_4 solution at a scan rate of 100 mV/s. The chips were rinsed with DI-water and blown dry with nitrogen. The depositions were performed by using 1 ml of deposition solution. Good agitation for reducing diffusion limitation is achieved by positioning a pipette tip mounted to a sonicating electric toothbrush into the solution.

The deposition scheme is performed by applying alternating voltage pulses (see Figure 7.2). During t_{on} , the deposition potential V_{on} is applied. During t_{off} , the electrode is brought back to the open circuit potential (OCP), and the ionic species to be deposited are replenished in the diffusion layer. The relaxation time t_{off} is set to a value, after which no significant current is flowing anymore. The OCP is determined with the help of the Ag/AgCl reference electrode and a platinum wire before deposition. The parameter windows for the different materials are listed in Table 7.1.

Metals like platinum or gold can be electrodeposited by reduction of aqueous solutions of their salts (Pourbaix et al. 1959). In this case V_{on} is lower than V_{off} and the OCP.

Compounds like phenol and phenylenediamines polymerize upon electrochemical oxidation

layer	t_{on}	V_{on}	t_{off}	$V_{off} = \text{OCP}$	cycles
Pt black	0.1-0.8 s	0 V	0.4 s	680 mV	100-250
Au smooth	0.25 s	-0.43 V	0.25 s	120 mV	220-360
Au porous	0.1 s	-0.45 V	0.1 s	120 mV	2000
PEDOT	0.2-0.3 s	1.05 V	0.5 s	275 mV	20-50
PPD	0.25 s	0.5-0.9 V	0.5 s	50 mV	60-500

Table 7.1: Parameter windows for the deposition of different materials yielding optimal results in terms of controlled growth.

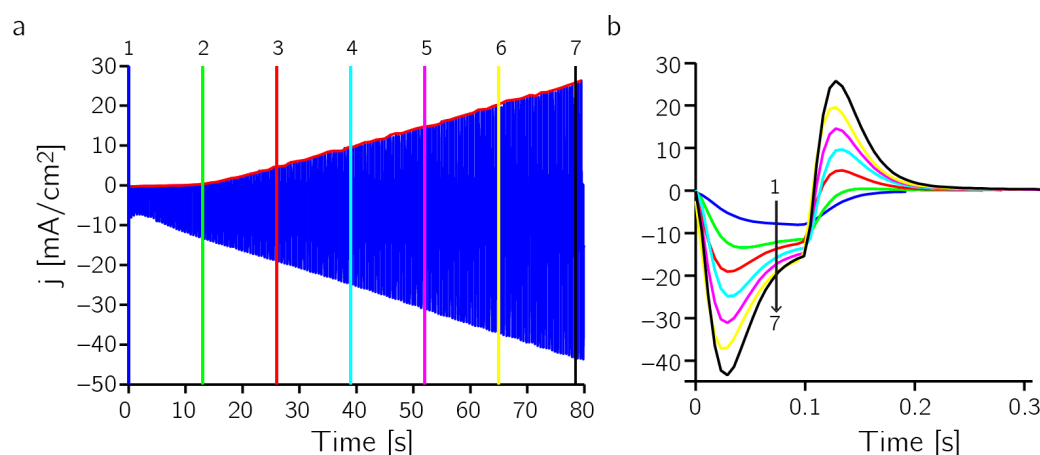


Figure 7.3: Deposition of Pt black - (a) current response during deposition; the red trace marks the peak heights due to charging of the increasing double layer; the pulses at times marked with vertical colored bars are zoomed in and overlaid in (b).

of the aromatic amine portion of the complex (Ohnuki et al. 1983; Guerrieri, Ciriello, et al. 2009), in which case the polarities are inverted ($V_{on} > V_{off}$).

7.3.2 Pt black

To increase the effective surface area while maintaining a small geometric sensor area, a layer of amorphous platinum black can be grown on the bare platinum electrodes. The increase in effective surface area lowers the impedance of an electrode and allows for better charge-transfer.

Materials and methods

Hexachloroplatinic acid (17.5 mM) and lead(II) acetate trihydrate (0.03 mM) (from Sigma-Aldrich, Buchs, Switzerland) dissolved in DI water were used for electrodeposition of Pt black.

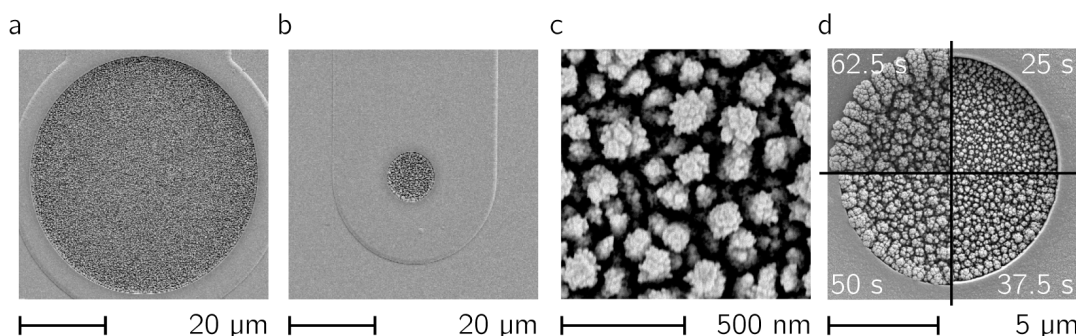


Figure 7.4: Deposited Pt black - SEM pictures of deposited Pt black layers. The same deposition parameters have been used for a 50-μm (a) and 10-μm (b) electrode. (c) Close up of the Pt black structure. (d) Different total t_{on} -times clockwise from top right 25 s, 37.5 s, 50 s, 62.5 s for deposition on a 10-μm electrode.

Platinum black was deposited by using the parameters listed in Table 7.1. The pulse widths t_{on} were varied between 0.1 and 0.8 s, t_{off} set to 0.4 s. The total t_{on} -times ($t_{on} \times$ number of pulses) were kept constant for each set of pulse-widths by adapting the number of pulses. The different depositions were performed sequentially without renewal of the solution.

Results

Figure 7.3 a shows the current pulse train during a deposition ($t_{on} = 0.1$ s $V_{on} = 0$ V, $t_{off} = 0.4$ s, $V_{off} = 0.68$ V, 160 cycles). The single pulses at several time points (at the vertical colored bars in Figure 7.3 a, from 1-7) were extracted and plotted in Figure 7.3 b (from 1-7). The first part of the pulse is due to a combination of non-faradaic (i.e. charging of the double layer) and faradaic (i.e. metal deposition) currents. The second (positive) part of the pulse is due to only non-faradaic charging of the double layer. Both pulses increased over time, as the active surface area grew, which corresponds to an increase of the double layer (DL) capacitance. The peak current of all these pulses is depicted by the red trace in Figure 7.3 a.

In Figure 7.4 a and b two electrodes with a diameter of 50 μm (a) and 10 μm (b) are shown. The layers were deposited by using the same deposition parameters. In both cases, the electrode surface is nicely covered, no overgrowth of the layers can be seen, and they show the same morphology upon optical inspection.

The porous structure (which is the reason for an increase in active area) of the Pt black surface is shown in Figure 7.3 c.

The effect of increasing the number of pulses can be seen in Figure 7.3 d. Pt black was deposited in the recess of the electrode (~ 1.6 μm) for a total t_{on} -on time of 25 s, 37.5 s, 50 s and 62.5 s (from top right clockwise); at 50 s the layer started to overgrow the electrode opening.

Figure 7.5 a is the result of a measurement from all electrodes on a single chip. It shows the dependence of the roughness factor on different pulse widths (t_{on}) and total t_{on} -times ($t_{on} \times$ number of pulses). Each point is the average of 64 electrodes; the standard deviation is depicted by semi-transparent layers below and above.

The roughness factors were determined coulometrically from the hydrogen desorption region of cyclic voltammograms (CVs) measured in a 0.5 M H_2SO_4 solution at a sweep rate of 100 mV/s (see also Section 6.2.2). The roughness factor (i.e. the ratio of active area to geometric area) is proportional to the total t_{on} -on time as expected. The roughness factor can be increased up to 150 without overgrowth of the electrodes.

Depositions at different pulse widths (t_{on}) cannot be distinguished optically (using SEM). Reducing the relaxation time t_{off} down to 0.25 s did not visibly change the structures or the electrochemical response of the resulting layer. However, the relaxation time may need to be increased for larger electrodes.

Another interesting aspect is shown in Figure 7.5 b: the charge from the hydrogen desorption region, used for determining the roughness factor, is plotted against the maximum anodic pulse height of the pulse train during deposition.

A clear linear dependence between pulse height and integrated charge can be seen. Hence, the active area can be predicted during deposition. This may prove useful to tune the active area and impedance of the electrodes in order to achieve a uniform response over the electrodes of a large array.

The voltage-pulse based deposition of Pt black provides a robust method to achieve spatially controlled and uniform deposition on an array of electrodes. The active surface area can be maximized, while keeping the geometric area restricted to the electrode opening.

7.3.3 Gold

Gold electrodes can be used to bind biomolecules covalently onto the surface via thiols. The strong affinity of the thiol groups for noble metal surfaces enables the formation of covalent bonds between the sulfur and gold atoms (Sassolas et al. 2008). This is a common approach used for nucleic acid biosensors (Wang 2002; Drummond et al. 2003). Hence, the voltage-pulse based deposition protocol was evaluated for the deposition of gold on the platinum electrodes.

Materials and methods

Neutronex 309 solution was bought from Enthone Inc. (Connecticut, USA) and used as is. Two different parameter sets were determined (see Table 7.1), which allow for production of gold surfaces with different morphologies.

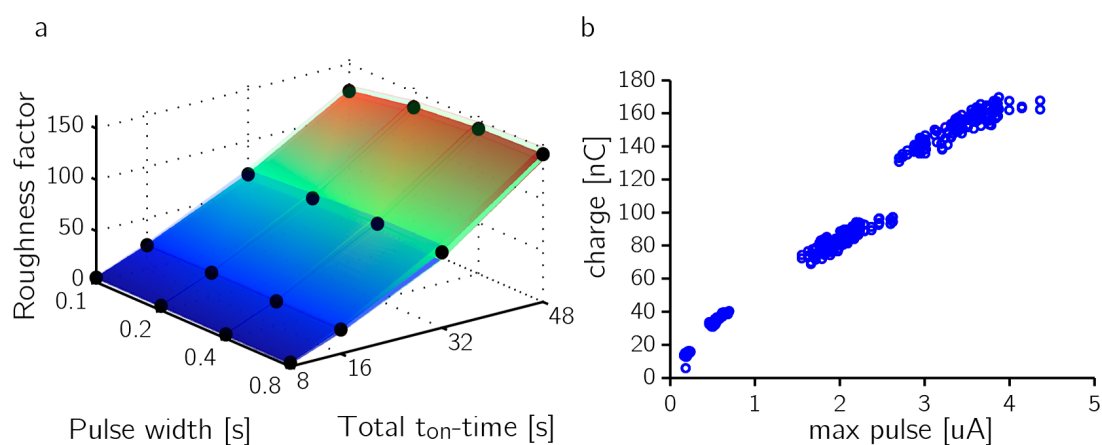


Figure 7.5: Pt black characteristics - (a) Roughness factor determined from integrating CVs in H_2SO_4 from all electrodes of one chip for different deposition parameters ($n=64$ per point). Standard deviations are represented by semitransparent layers. (b) Integrated charge from the hydrogen desorption region vs. maximum positive pulse of pulse train during deposition.

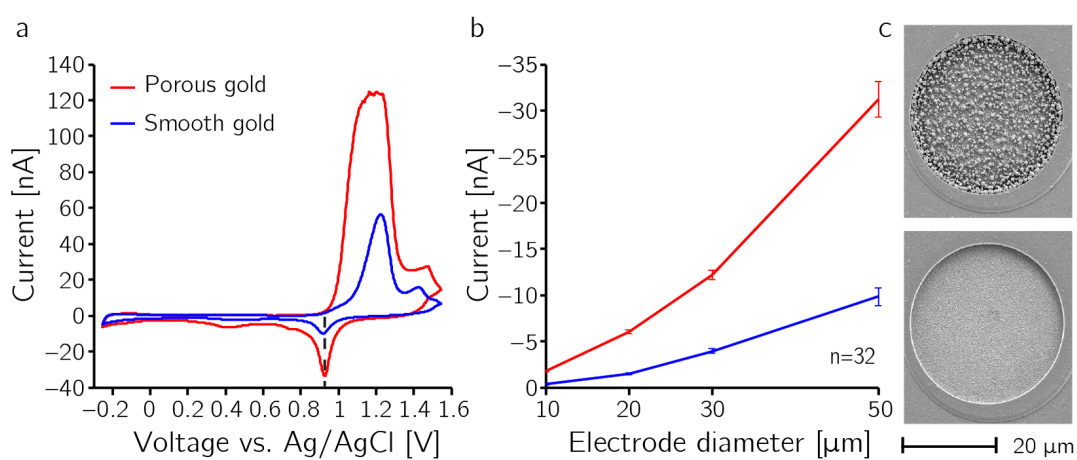


Figure 7.6: Gold deposition - Cyclic voltammogram of an electrode with deposited gold layer. (a) CV of 50- μ m electrode modified with porous, or smooth gold in 0.5 M H_2SO_4 from -0.25V - 1.55V vs. Ag/AgCl; sweep rate 100 mV/s. A single sharp reductive peak can be seen at ~ 0.9 V. Electrodes are completely covered, since no traces of platinum are visible. (b) Reductive peak heights for different electrode diameters, for smooth and porous gold. (c) SEM of 30- μ m electrode after deposition of porous gold (top) and smooth gold (bottom) layers.

Results

By altering the deposition time (t_{on}) the layers can be made either smooth or porous: smooth gold depositions are achieved by using pulse durations t_{on} of 0.25 s or longer; porous gold deposition by using t_{on} -times of 0.1 s.

Figure 7.6 a shows a CV in 0.5 M H_2SO_4 performed on a 50- μ m gold electrode covered with porous gold and one with smooth gold, while using a sweep rate of 100 mV/s. Complete gold coverage of the electrode without contaminations is indicated by the characteristic CV features of gold, with the single oxygen reduction peak at ~ 0.9 V (Hoare 1984).

The total t_{on} -time needed for complete coverage was 50 s for smooth and 150 s for porous gold. If the electrodes are not covered completely, the CV cannot be performed in the range specific for gold electrodes (up to 1.6 V), since the platinum surface will promote the generation of gaseous oxygen above 1.2 V vs. Ag/AgCl, which will lead to excessive currents and overload the potentiostat. The dependence of electrode diameter on peak height of the oxygen reduction peak (marked with a dashed line in Figure 7.6 a) on the electrode diameter is shown for different layer types in Figure 7.6 b. Porous gold has 3 ± 1 times higher active surface area due to the dendritic growth. The peak height is proportional to the area of the electrode.

Besides a spatially controlled deposition, the voltage-pulse based deposition scheme allows for varying the morphology of the gold layer by changing pulse parameters.

7.3.4 Conducting polymers

To evaluate the proposed deposition scheme for the deposition of conducting polymers, PEDOT was chosen as an example system. PEDOT has been used for building biosensors by embedding enzyme into (Madangopal et al. 2012), or by attaching enzyme onto (Vidal et al. 2003) the conducting polymer. Furthermore, PEDOT has been used for neurotransmitter sensing (Samba et al. 2014) and as an anti-fouling layer (Yang et al. 2013).

Materials and methods

Poly(sodium 4-styrenesulfonate) (PSS, MW $\sim 70,000$ g/mol) and 3,4-Ethylenedioxythiophene (EDOT, 97%) were bought from Sigma Aldrich (Buchs, Switzerland). PEDOT deposition solution was prepared by adding 20 mM EDOT to PSS (1 wt%) in water. Thorough mixing and immediate use is crucial, since the monomer will precipitate from solution.

PEDOT was deposited using the parameters listed in Table 7.1. The pulse widths t_{on} were varied between 0.2 and 0.3 s, t_{off} set to 0.5 s; the number of pulses varied between 20 and 50 pulses.

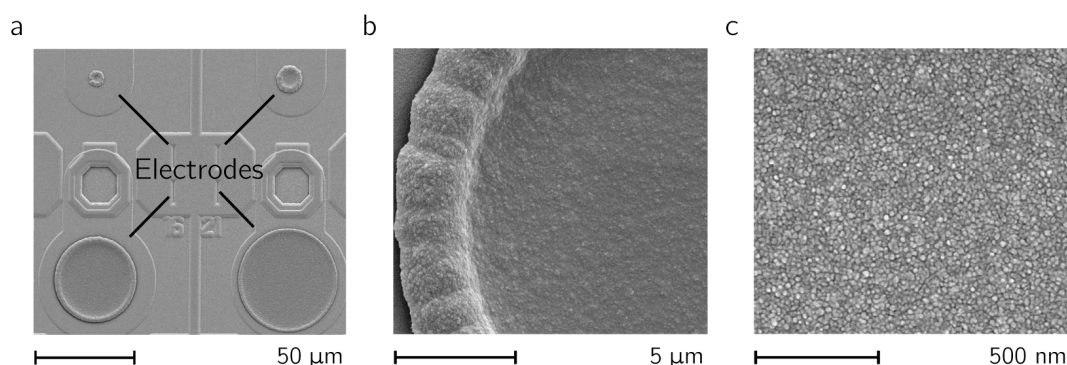


Figure 7.7: Deposited PEDOT - (a) SEM pictures of (top) 5, 10, 40 and 50 μm electrodes and (b,c) close-up views of a 25- μm electrode after PEDOT deposition.

Results

Depositions on differently sized electrodes are shown in the SEM micrographs of Figure 7.7 a. A slight overgrowth on the rim of the electrodes was observed. The dense structure of the deposited layer can be seen in Figure 7.7 b and c. Figure 7.8 a shows a CV performed in PBS between -0.3 and 0.3 V vs. Ag/AgCl at a sweep rate of 100 mV/s. A large non-faradaic current can be observed as compared to a bright Pt electrode (black trace in Figure 7.8 a). In Figure 7.8 b the integrated charge is plotted against the total t_{on} -time. The results indicate, that the total t_{on} -time defines the capacitance. The capacitance can be estimated by the current values of the CV ($C=I/\text{sweep rate}$). For the values in Figure 7.8, the capacitance ranges between 50-150 nF (10-30 mF/cm²), which ~ 1000 times larger than the capacitance measured on bright Pt electrodes ($150 \text{ pF} \hat{=} 30 \mu\text{F/cm}^2$).

However, in contrast to Pt black, due the smooth and dense layer morphology (see Figure 7.7 c), an increase in active surface area cannot be used to explain the interface capacitance increase. PEDOT/PSS is known to exhibit a large pseudo-capacitance due to the immobilized anions (PSS^- ; Bobacka et al. (2000)). Hence, the dependence of the pseudo-capacitance on the total t_{on} -time observed in Figure 7.8 can be attributed to differences in the deposited layer thickness.

The voltage-pulse based deposition provides fine control over the impedance of a layer of PEDOT by variation of the layer thickness.

7.3.5 Non-conducting polymers

Finally, the voltage-pulse based deposition procedure has been applied to the deposition of a non-conducting polymer. The non-conducting nature of these polymers is used to reject other electro-active molecules, such as dopamine (DA) and ascorbic acid (AA), from being oxidized and interfering with the signal of interest (Guerrieri, De Benedetto, et al. 1998).

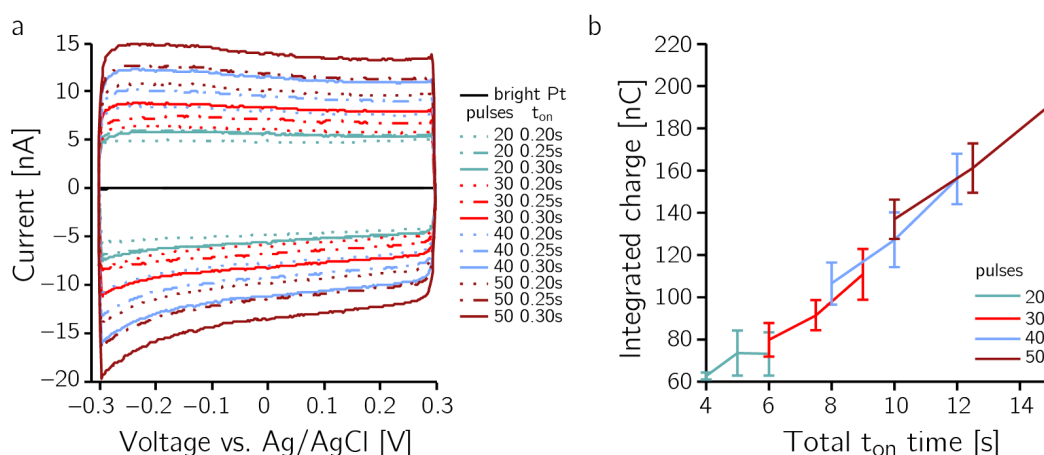


Figure 7.8: PEDOT - (a) CV in PBS -0.3 — 0.3V vs. Ag/AgCl 100 mV/s sweep rate, on 25- μ m diameter electrodes for bright Pt electrodes and for depositions with t_{on} of 0.2s, 0.25s, 0.3s and 20, 30, 40, 50 pulses. (b) Integrated charge for different total- t_{on} times. Colors code the number of pulses and correspond to (a). The integrated charge of a CV of a bright Pt electrode is 200 pC.

PPD is a non-conducting polymer that can be deposited by the electropolymerization of o-phenylenediamine (o-PPD). PPD provides permselective properties (Ohnuki et al. 1983) and has been used as a matrix for embedding biosensitive elements (Lowry et al. 1994).

Materials and methods

For the PPD layer, o-phenylenediamine (100 mM, Sigma Aldrich; Buchs, Switzerland) was dissolved in de-aerated PBS. The depositions were performed with pulse widths of $t_{on} = 0.25$ s; the voltages V_{on} were varied between 0.5 and 0.9 V vs. Ag/AgCl.

Depositions of PPD are self-limiting: the non-conducting nature suppresses further electrodeposition. Nevertheless, the number of pulses has been varied between 60 and 500 to verify if sufficient total deposition times were used. The layer of PPD is transparent, and the deposited thickness in the range of 60 nm (Malitesta et al. 1990), hence, calibration measurements have been performed to assess the properties of the film.

Results

Results from calibration measurements are shown in Figure 7.9. Two blocks of 20- μ m-diameter electrodes were evaluated: the electrodes of the left block are completely covered with PPD, those of the right block are half covered with PPD, the other half is left blank for comparison. Sensitivities were determined by measuring the current due to additions of solutions of different concentrations of DA and AA (0 – 400 μ M). The permselective nature is evident: the signal due to DA on functionalized electrodes is suppressed by a factor of 24, the signal due to additions of AA by a factor of 160, compared to bright Pt electrodes.

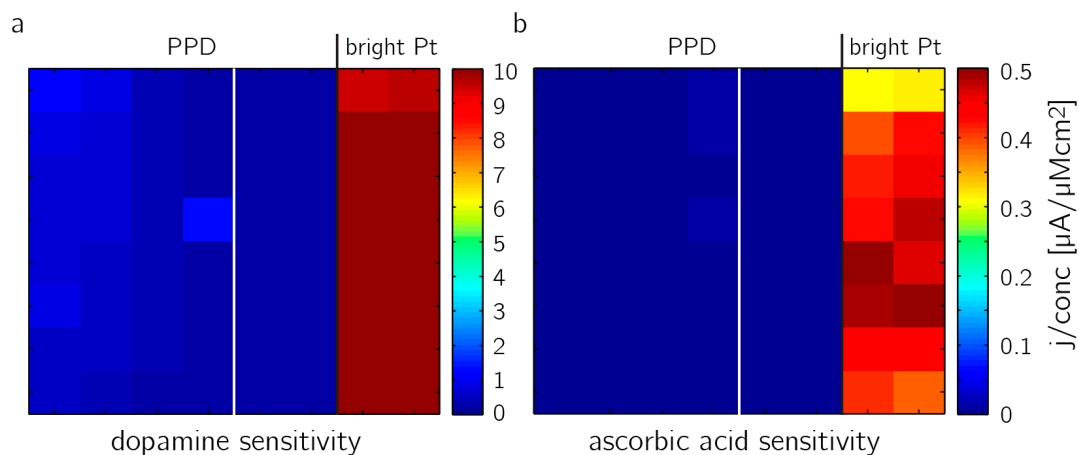


Figure 7.9: Non-conducting polymer PPD - Sensitivity evaluated for two blocks of 20- μm electrodes: the left block was completely covered with PPD; half of the right block was covered with PPD and half was left with bright Pt electrodes. Sensitivity evaluated for (a) dopamine and (b) ascorbic acid.

However, varying the parameters of the deposition protocol did not show a clear dependence with respect to the suppression of DA or AA. This might be due to self-limiting deposition of the non-conducting polymer.

The layer of PPD provides an effective anti-interference layer.

7.4 DISCUSSION

Drop coating, a simple method, does not provide specific and defined layer deposition, hence, it is only applicable for some special cases and not appropriate for multi-analyte sensing. Electrically aided adsorption can provide spatially defined layers, however, the layer thickness is hard to control, which is a prerequisite for uniform electrode sensitivity across the array. Electrodeposition can provide spatial control, since deposition can only occur, where charge-transfer happens, and it can provide defined thicknesses, since the volume of the deposited material is defined by the total current during deposition.

The presented voltage-pulse method is suitable for deposition on different electrode sizes (i.e. 5-50 μm diameter) while using the same parameters. The voltage-pulse deposition is well suited for larger electrode arrays and allows for using the same deposition parameters on many electrodes in parallel. This feature is especially useful when a new material or a new design should be established; the possibility to perform a tuning of the deposition method on only a few electrodes and then scaling it up to the array with the optimized protocol parameters is the big advantage of this method. The materials, which are amenable to voltage-pulse based deposition methods (i) can provide a large active surface (e.g. Pt black and PEDOT),

(ii) can serve as a matrix for included biomolecules (e.g. PPD and PEDOT), (iii) allow for binding of other molecules to the surface (e.g. gold), or (iv) act as a size discriminating or anti-interference layer to reduce cross-sensitivity (e.g. PPD).

Finally, the scheme can be easily adapted for other materials that can be used for electrodeposition.

8

MEASUREMENTS OF BIOLOGICALLY RELEVANT SPECIES

In the previous chapters, the design of the electrochemical CMOS microsystem was elaborated, the electrical and electrochemical characteristics and techniques were shown, packaging methods were demonstrated, and functionalization schemes were investigated. This chapter demonstrates the usage of the measurement system for possible applications. The goal was to assess the system with respect to functionality and signal quality by applying different electroanalytical techniques and different functionalization schemes. Biologically relevant species involved in signaling, e.g., neurotransmitters and neuromodulators, and molecules involved in the metabolism of cells, were chosen as example analytes.

The measurements in the sections on neurotransmitters and metabolites were performed by connecting the readout channels continuously to selected electrodes. Whereas in the final section, the measurement system was used to acquire amperometric electrochemical "images", where the electrodes are sequentially connected to the readout channels, and where concentrations of analytes over the whole array at high spatial and temporal resolution were measured.

8.1 NEUROTRANSMITTERS

Measuring changing neurotransmitter concentrations from a brain slice, or from neurons cultured on the sensing array, can add an additional level of insight into the functioning of the brain, the role of neurotransmitters in the context of different diseases, or the efficacy of drugs.

Possibilities of detecting neurotransmitters with the electrochemical sensor array were investigated.

8.1.1 Dopamine detected via square wave voltammetry

The neurotransmitter dopamine plays an important role in addiction and goal-directed behavior in the brain. Dopamine is linked to diseases like schizophrenia and Parkinson's.

Dopamine is an electroactive molecule; the concentration can be directly determined by the faradaic current from oxidation. Hence, various voltammetric methods have been applied to detect dopamine concentrations. Among them, square wave voltammetry (SWV) can provide measurements that are more selective, compared to amperometry, and more sensitive, compared to cyclic voltammetry (see Section 6.1.3).

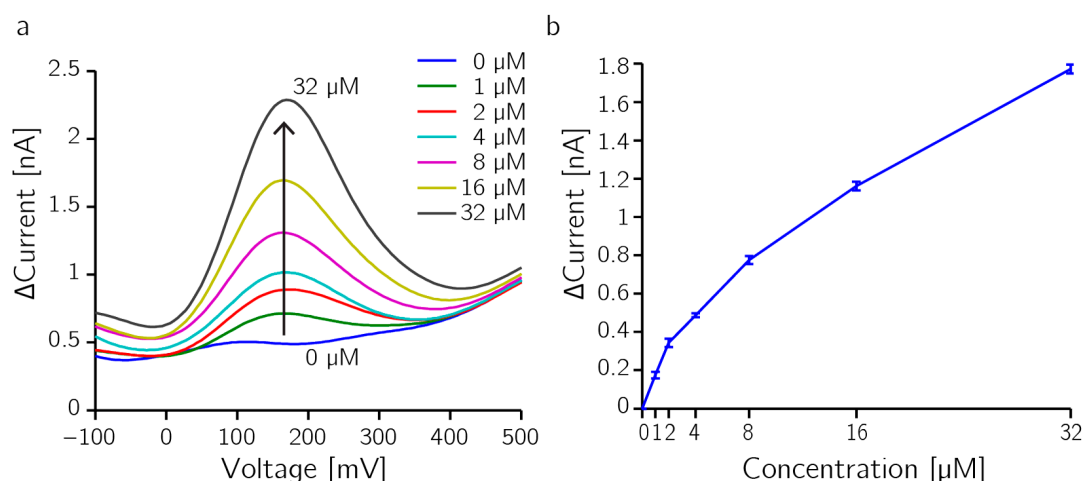


Figure 8.1: Dopamine sensing - (a) Differential current from the detection of dopamine via square wave voltammetry $E_{\text{pulse}} = 32.8$ mV, $E_{\text{step}} = 5.5$ mV, $t_{\text{period}} = 0.2$ s sampled 10% before the end of each pulse; measured at single 25- μm electrode functionalized with PEDOT. (b) Calibration curve: mean and standard deviation were determined from the response of 8 neighboring electrodes.

Materials and methods

Functionalization of the electrodes with PEDOT:PSS was performed according to Section 7.3.4. Dopamine calibration stock solution (10 mM in DI water from dopamine hydrochloride; Sigma-Aldrich, Buchs, Switzerland) was prepared immediately before use.

Calibration measurements were performed in phosphate-buffered saline (PBS) (0.01 M). Neurotransmitter samples were consecutively injected into the electrolyte solution followed by manual stirring.

Square wave voltammetry was applied using a pulse height of $E_{\text{pulse}} = 32.8$ mV, a step height of $E_{\text{step}} = 5.5$ mV, and a period of $t_{\text{period}} = 0.2$ s. An external Ag/AgCl reference electrode was used. The current was sampled during the last 10% of the pulse duration. The sensitivity is derived from the calibration curve by determining the peak current after subtracting the background current.

Results

In Figure 8.1 a, square wave voltammograms of 0 to 32 μM dopamine solutions recorded with single 25- μm diameter electrodes are shown. The trace shows the differential current after subtracting the response of the reverse pulse from the response of the forward pulse. The sensitivity of the measurements can be seen in Figure 8.1 b, where the mean and standard deviations of the peak current versus the concentration are plotted for 8 electrodes. The calibration curve deviates from a linear relationship. The initial part of the calibration curve at concentrations below 8 μM can be linearized and shows a sensitivity of 170 pA/ μM (35

$\mu\text{A } \mu\text{M}^{-1} \text{ cm}^{-2}$). The sensitivity of the second part of the calibration curve, including concentrations of 4 – 32 μM , can be approximated to 45 pA/ μM (9 $\mu\text{A } \mu\text{M}^{-1} \text{ cm}^{-2}$).

Discussion

SWV on PEDOT:PSS electrodes allowed for the measurement of dopamine concentrations down to 1 μM . The sensitivities determined in this work are higher compared to PEDOT-functionalized 25- μm diameter gold electrodes (18/6 $\mu\text{A } \mu\text{M}^{-1} \text{ cm}^{-2}$; low/high concentration range) and comparable to PEDOT electrodes with embedded carbon nanotubes (37/12 $\mu\text{A } \mu\text{M}^{-1} \text{ cm}^{-2}$), presented, e.g., in Samba et al. (2014).

The measurement system offers enough dynamic range to be able to perform the SWV method.

The non-linear response and the saturation of the response is not a consequence of the detection method or the electric circuits, but may be due to adsorption of reaction products of the oxidation of dopamine (see also Samba et al. (2014)). Another issue is electrode contamination: after coming in contact with the dopamine calibration solution, even electrodes that had not been polarized showed a residual peak in pure buffer solution (see also Samba et al. (2014)).

Contamination and electrode fouling (deposition of reaction products on the electrode surface), are a problem in dopamine sensing and a general problem in detecting electroactive species. Different materials can be used to reduce their effects, or additional anti-fouling layers can be added. However, an additional layer can influence the primary functionalization and lead to signal degradation.

8.1.2 Choline detected via an enzymatic biosensor

Another neurotransmitter is acetylcholine, which is highly involved in cognitive functions, such as learning, memory and behavior. Malfunctions of the cholinergic system are related to neurological disorders, such as Alzheimer's disease and depression.

Choline, the precursor of acetylcholine, is not electroactive, and a biosensitive layer is needed for detection. Using the enzyme choline oxidase, choline concentrations can be measured via the amperometric detection of hydrogen peroxide.

Materials and methods

The surface of individual microelectrodes was coated with an enzymatic membrane. Functionalization is based on electrochemically aided adsorption (EAA) (see Section 7.2), combined with chemical co-cross-linking by using glutaraldehyde (according to O. Frey et al. (2010)). All chemicals were bought from Sigma-Aldrich (Buchs, Switzerland). Choline oxidase (20 U), was mixed with PBS (500 μl) and bovine serum albumin (8 mg). Glutaraldehyde (20 μl , 25%) was added just before the deposition. By applying a train of 25 pulses, (3 s at 1.8 V,

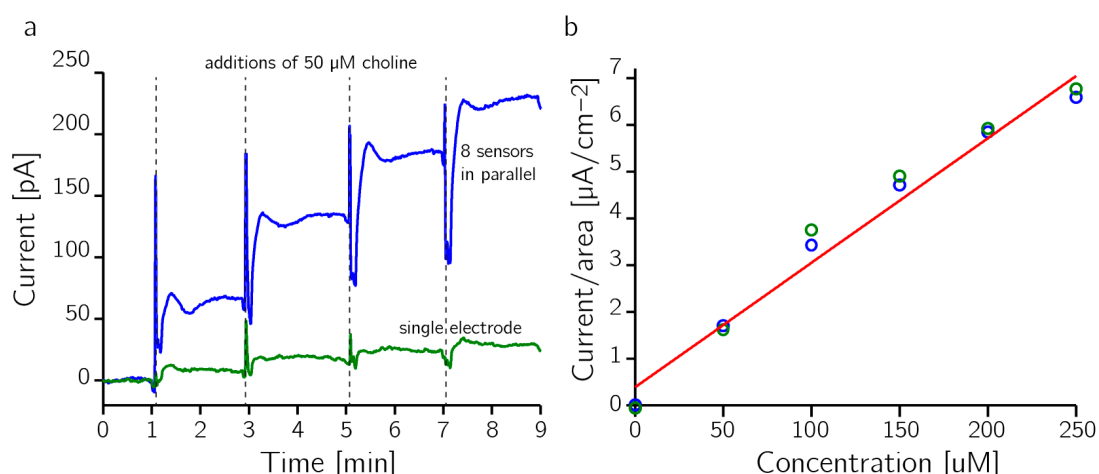


Figure 8.2: Choline calibration - (a) Raw data of a single electrode and eight 25- μm electrodes connected in parallel. 50 μM of choline was added four times. (b) Sensitivity of the biosensors determined from (a).

followed by 6 s at 0.4 V), cross-linking was initiated.

For the enzymatic biosensor calibration, small amounts of choline were added five times into PBS solution, resulting in a concentration increase of 50 μM . After each addition the solution was thoroughly stirred by using a pipette. The working electrodes were set to 0.65 V vs. an external Ag/AgCl for amperometric detection of hydrogen peroxide. An external Pt counter electrode and an Ag/AgCl reference electrode were used. The signals were evaluated after reaching steady state.

Results

Figure 8.2 a shows two curves of raw data: the response of a single 25- μm electrode and the cumulative response of eight electrodes connected in parallel. Artifacts in the response curves at the time of analyte addition result from stirring. The sensitivity per area is depicted for both configurations in Figure 8.2 b. The approximate response time of a single sensor is 2 seconds (rise time of the sensor response from 0 to 90% of the final value). Both curves show comparable behavior and a sensitivity of $\sim 27 \mu\text{A mM}^{-1} \text{cm}^{-2}$ (single electrode 135 pA/mM). The theoretical limit of detection (3 times the background noise) has been calculated as 33 μM .

Discussion

For measuring in the physiological range (1–10 μM) the sensitivities achieved were not sufficient, and a better biosensitive layer has to be employed.

A picture displaying the functionalized and used electrodes was shown before in Figure 7.1

b. The deposition method allows for spatial control, whereas control of the layer thickness is limited. The response times due to the thick layers are long, but may be acceptable for monitoring slow changes of neurotransmitter levels in the brain.

8.2 METABOLITES

The metabolism of a cell is key for understanding cell functions, determining cell viability and functionality, and the influence of drugs on cells. If single cells or several cells could be cultivated atop the sensing electrodes of the array, changes in concentrations of certain analytes, due to application of drugs, or forms of altered metabolism could be monitored in a massively parallel approach.

8.2.1 Glucose detected via enzymatic biosensor

Glucose is an ubiquitous source of energy in most organisms from bacteria to humans. Glucose oxidase is often used as a model enzyme to perform and test immobilization procedures for biosensors, due to the good availability and its excellent stability (Raba and Mottola 2006). Due to the ease of application, glucose oxidase functionalization was performed by drop coating.

Materials and methods

To build a glucose sensor by drop coating, a freshly prepared solution of glucose oxidase (30 U) in 250 μ l DI water, bovine serum albumin (10 mg) and glutaraldehyde (5 μ l, 25%) was pipetted and evenly distributed on the array. All chemicals were bought from Sigma-Aldrich (Buchs, Switzerland). The solution was left to dry for 1 hour at room temperature and rinsed with DI water to remove not cross-linked proteins.

Glucose stock solutions (30 mM) were prepared in DI water and allowed to undergo mutarotation overnight at 4 °C.

For the enzymatic biosensor calibration, the working electrodes were set to 0.65 V vs. Ag/AgCl for amperometric detection of hydrogen peroxide. An external Pt counter electrode and an Ag/AgCl reference electrode were used. Small amounts of glucose were added four times into PBS solution, resulting in a concentration increase of 10 μ M each time. After each addition, the solution was thoroughly stirred by using a pipette. The signals were evaluated after reaching steady state.

Results

Figure 8.3 a shows raw data from 8 selected microelectrodes of a calibration measurement executed in PBS solution. The time to reach steady state was \sim 4 minutes. The sensitivity

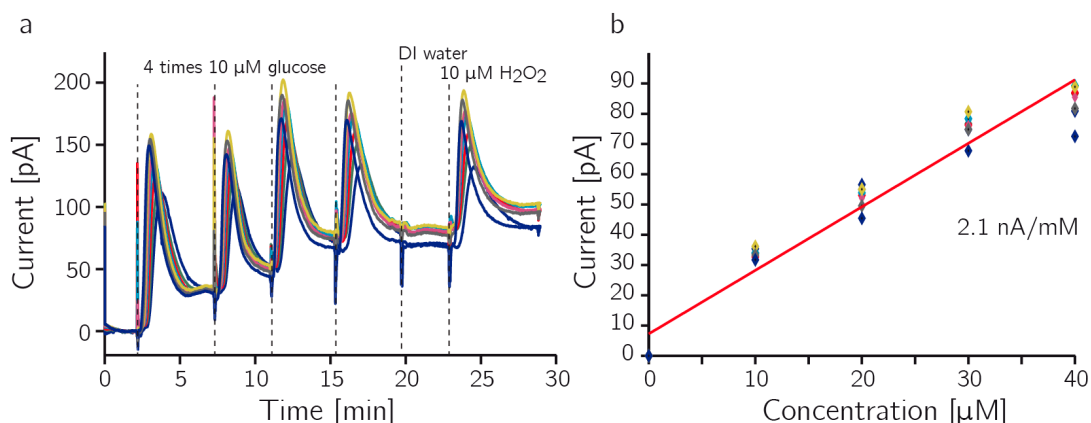


Figure 8.3: Glucose calibration - (a) Raw data from 8 individual 25-μm electrodes. Glucose concentration was increased 4 times by 10 μM each. (b) Sensitivity of the biosensors determined from (a) by linear fitting.

of the sensor was 2.1 nA/mM glucose ($427 \mu\text{A mM}^{-1} \text{ cm}^{-2}$). The limit of detection has been calculated as 1.1 μM.

Discussion

Drop coating as a functionalization method is a simple protocol with only very limited control of spatial deposition and thickness of the layer. As mentioned before, automated dispensing equipment would be needed to improve controlled deposition.

The good sensitivity can be attributed to the excellent properties of the enzyme, and to the thick enzyme layer. However, this thick layer leads to excessive response times. To measure concentrations of glucose at physiological levels (4 – 6 mM in human blood), other, more sophisticated biosensing techniques have to be applied (Wang 2008).

8.2.2 Lactate detected via an enzymatic biosensor

Besides glucose, lactate is another important metabolite. In an anaerobic fermentation reaction that occurs in some bacteria and animal cells (i.e. muscle cells), glucose is converted into cellular energy and the metabolite lactate. Lactate can be detected amperometrically via the enzyme lactate oxidase. Since lactate oxidase is less accessible, thinner layers and better spatial control are needed to only coat the electrodes with the enzymatic layer. For that reason the functionalization has been performed by using electrochemically aided adsorption (EAA).

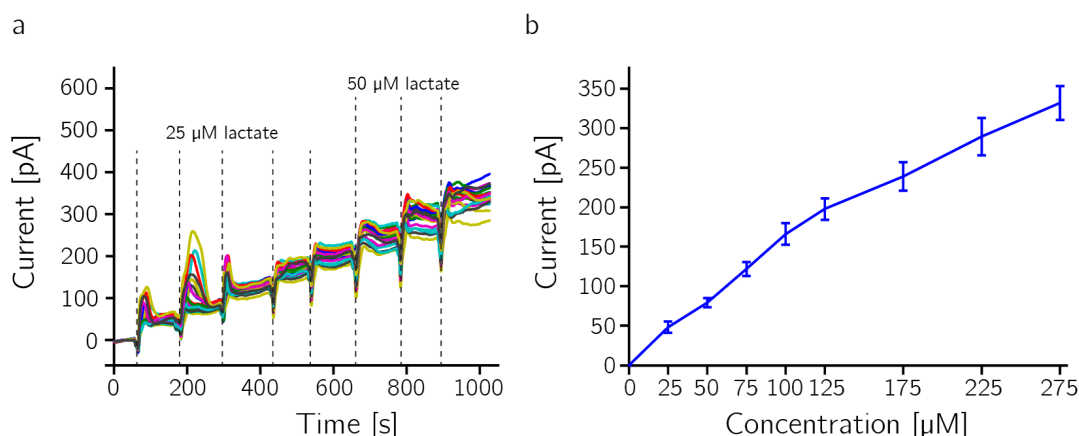


Figure 8.4: Lactate calibration - (a) Raw data from 32 sensors. Lactate concentration was increased in 25 μM steps for five times, then in 50 μM steps three times. (b) Calibration curve, mean and standard deviation of the 32 sensors used in (a).

Materials and methods

The experiments were performed on the concentric ring electrodes. The inner disk electrodes (135 μm diameter) were functionalized by EAA according to Section 7.2. All chemicals were bought from Sigma-Aldrich (Buchs, Switzerland). Lactate oxidase (30 U) was mixed with PBS (500 μl) and bovine serum albumin (10 mg). Glutaraldehyde (3 μl , 25%) was added just before the deposition. By applying a train of 25 pulses, (3 s at 1.8 V, followed by 6 s at 0.4 V), cross-linking was initiated.

For the enzymatic biosensor calibration, an external Pt counter and Ag/AgCl reference electrodes were used, and the working electrodes were set to 0.65 V vs. Ag/AgCl for amperometric detection of hydrogen peroxide.

Results

In Figure 8.4 a the raw data of the calibration are shown for 32 electrodes. Artifacts at the time of addition of lactate stem from manual stirring. The response time was approximately 5 seconds. In Figure 8.4 b the calibration curve is plotted. The sensors exhibit an average sensitivity of 1.2 nA/mM ($8.36 \mu\text{A mM}^{-1} \text{ cm}^{-2}$). The theoretical limit of detection is 1.4 μM .

Discussion

The 50 times lower sensitivity of lactate sensors as compared to glucose sensors can be attributed to a much thinner enzyme layer. The advantage of the thin layer lies in the response time, which is now in an acceptable range (5 s). The lactate sensor has been

prepared according to functionalization scheme (EAA) used for the choline sensor. However, the protocol for choline could not be directly transferred to the functionalization to detect lactate and had to be adapted. A protocol for successful lactate functionalization through EAA on small 25- μm diameter electrodes could not yet be established. In comparison to the choline sensors, the lactate sensors show higher sensitivity, a lower limit of detection, but longer response times.

The corresponding picture of the functionalized electrodes was shown before in Figure 7.1 a. As for the choline sensor functionalization, spatial control could be achieved.

8.3 ELECTROCHEMICAL IMAGES

One major feature of the measurement system is the possibility to acquire electrochemical images at high spatial and temporal resolution. The measurements in the previous sections were performed on individual electrodes, which were continuously connected to the readout channels. For acquiring electrochemical images, the electrodes were connected consecutively to the readout channels (i.e. time multiplexing). In between the electrodes were left floating.

8.3.1 Hydrogen peroxide

Hydrogen peroxide is an important molecule in living-organisms. However, more important for biosensing is the fact that H_2O_2 is a side product generated from biochemical reactions catalyzed by the enzyme class of oxidases and is extensively utilized in enzymatic biosensing. Therefore, measurement of H_2O_2 concentration was utilized to establish the fast acquisition of electrochemical images from the whole array.

Materials and methods

Electrochemical images have been acquired in PBS. An aliquot of H_2O_2 (1 μl of 30 mM into 3 ml of PBS) was injected with a microneedle into the liquid at the center of the array (~ 0.5 mm distance). Amperometric measurements to of H_2O_2 concentrations were done at 0.5 V vs. an external Ag/AgCl reference electrode and by using the on-chip platinum counter electrode.

A calibration experiment to assess sensitivity was performed by using a simple fluidic PDMS chamber placed on the array. A syringe pump was used to pump different concentrations of H_2O_2 in PBS at a flow rate of 10 $\mu\text{l/s}$ over the array. On-chip Pt counter and pseudo-reference electrodes were used with the working electrodes set to 700 mV.

Results

An amperometric electrochemical image sequence from all 1024 25- μm -diameter electrodes of the array was acquired at 89 frames per second (fps) (see Figure 8.5). The image sequence

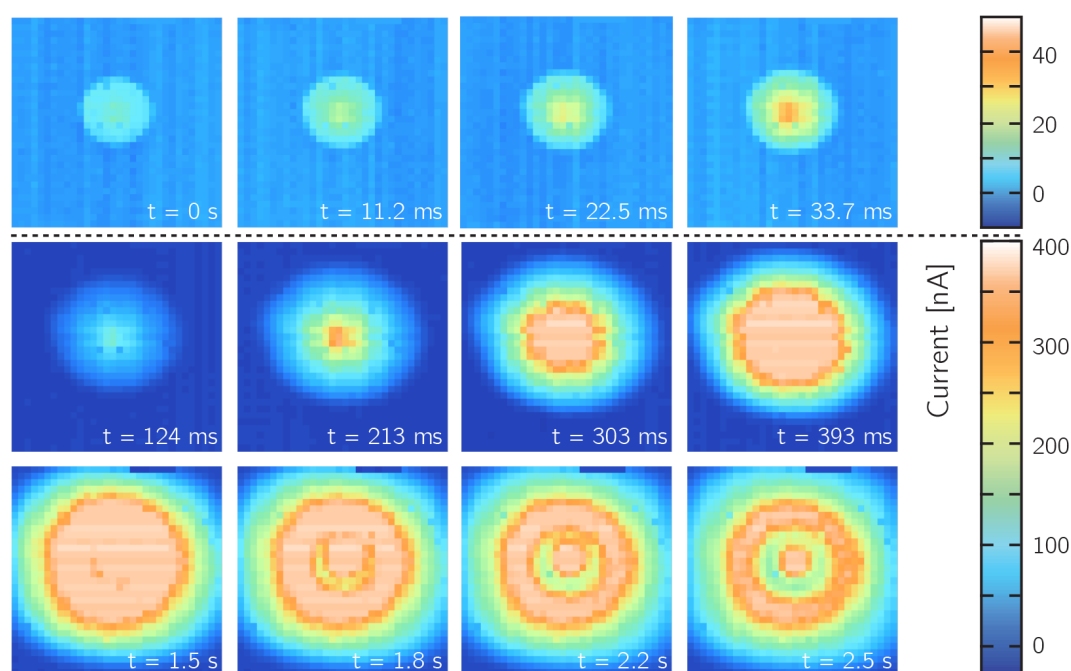


Figure 8.5: Electrochemical imaging - Image sequence of amperometric measurement at 0.5 V vs. an external Ag/AgCl reference electrode showing the distribution of an aliquot of H_2O_2 injected in the center of the liquid phase over the array, taken at a frame rate of 89 fps. Electrodes were modified by depositing Pt black. The image size corresponds to an area of 3.2 by 3.2 mm^2 .

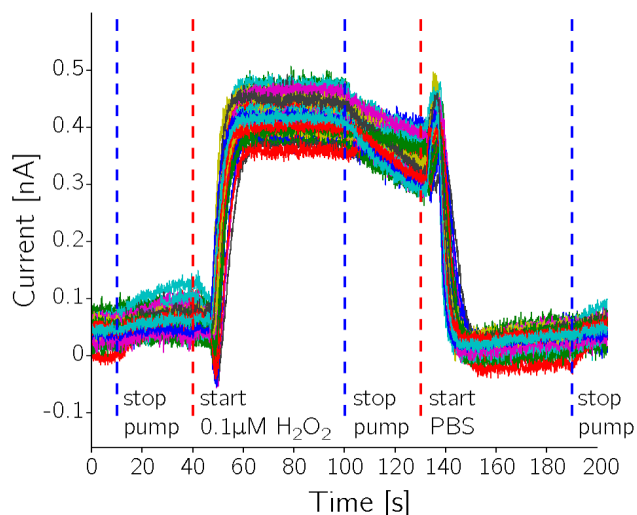


Figure 8.6: Sensitivity - Raw data of amperometric H_2O_2 calibration experiments, measured with 32 individual electrodes of $25\ \mu\text{m}$ diameter.

shows the injection of an aliquot of H_2O_2 ($1\ \mu\text{l}$, $30\ \text{mM}$) via a syringe into PBS ($3\ \text{ml}$) atop the electrode array and subsequent liquid-phase transport of the H_2O_2 -molecules across the array area. The first row in Figure 8.5 contains images from consecutive frames of the video showing the beginning of the injection of peroxide. The pictures in the following rows were extracted from the video at different points later in time.

The raw traces from the calibration experiment of 32 individual $25\text{-}\mu\text{m}$ electrodes can be seen in Figure 8.6. The mean sensor sensitivity to H_2O_2 was $4.5\ \text{nA}/\mu\text{M}$ ($917\ \mu\text{A}\ \mu\text{M}^{-1}\ \text{cm}^{-2}$), with a theoretical limit of detection of $13\ \text{nM}$ (calculated by using 3 times the background noise).

Discussion

The images were taken at $89\ \text{fps}$, which means that more than $91'000$ sensor current values have been read out per second from an area of $3.2\ \text{by}\ 3.2\ \text{mm}^2$. Compared to image sequences acquired by electrochemical CMOS microarrays shown in previous publications, this is more than twice the frame rate for 10 times more electrodes (10×10 electrodes at $40\ \text{fps}$ (Kim et al. 2013), and more than twice the number of electrodes at more than 15 times the frame rate (20×20 electrodes at $5\ \text{fps}$ (Inoue et al. 2012; Sen et al. 2013)).

The fast acquisition enables resolution of the wave of the H_2O_2 -molecules, traveling at a speed of $2.2\ \text{mm/s}$ to the corners of the array. The high temporal and spatial resolution allows for tracking liquid-phase diffusion and convection processes.

The low limit of detection is important for enzymatic biosensors, where the enzyme load of

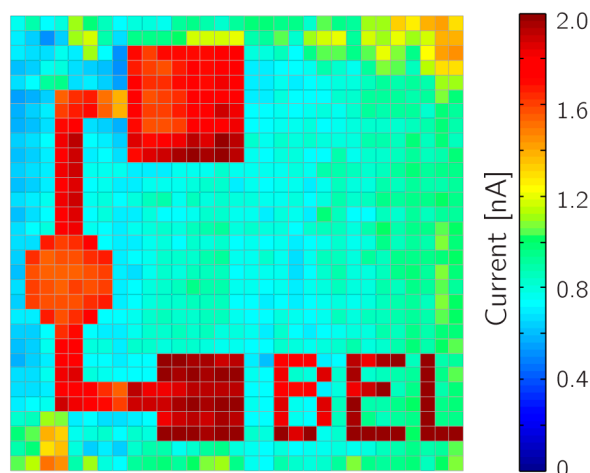


Figure 8.7: Specific glucose functionalization - Addition of 1 mM of glucose to an array, on which only a defined number of electrodes were functionalized with glucose oxidase to form the logo of our lab.

a functionalized electrode is limited, and hence, low amounts of peroxide are produced by the enzymatic reaction in response to the analyte of interest.

8.3.2 Specific functionalization to detect glucose

As an example biosensor application, an array with 1024 25- μm electrodes was modified to monitor glucose. The electrodeposition method allowed for functionalization of only selected electrodes, so as to display the logo of our lab. The amperometric detection of the analyte was combined with the fast acquisition of electrochemical images.

Materials and methods

Glucose oxidase (15 kU/ml; Sekisui Diagnostics, Lexington, USA) in 500 μl de-aerated PBS was mixed with o-phenylenediamine (100 mM; Sigma-Aldrich, Buchs, Switzerland) in 500 μl de-aerated PBS. An external Ag/AgCl reference electrode and an external platinum wire as counter electrode were used. The deposition was achieved by applying cyclic voltage signals in the range of 0 – 0.9 V vs. Ag/AgCl at 50 mV/s over 15 cycles.

For the enzymatic biosensor calibration, an external Pt counter electrode and an Ag/AgCl reference electrode were used. The working electrodes were set to 0.65 V vs. Ag/AgCl for amperometric detection of hydrogen peroxide.

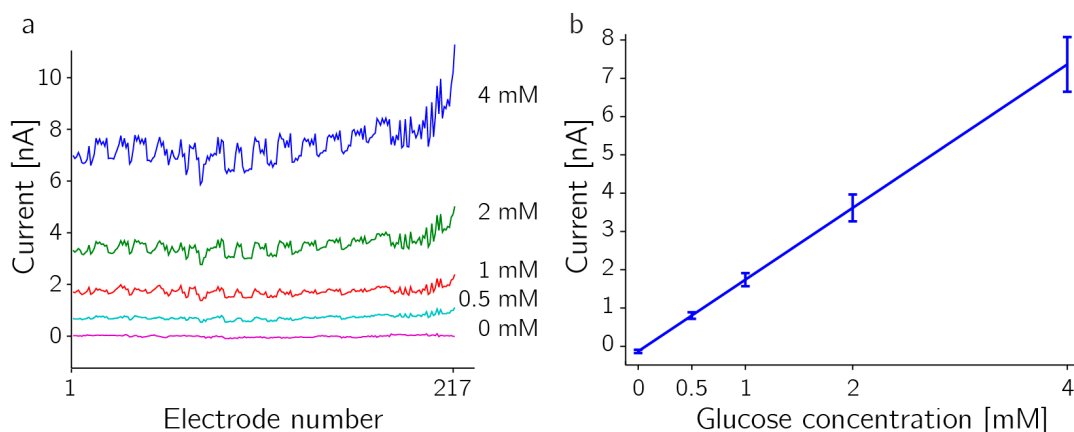


Figure 8.8: Glucose calibration - Calibration curve of the glucose biosensor. (a) response of all 217 functionalized electrodes to additions of glucose. (b) Mean response of the glucose sensors. Error bars denote the standard deviation. Sensitivity is $1.87 \text{ nA/mM} \pm 180 \text{ pA/mM}$ ($382 \mu\text{A mM}^{-1} \text{ cm}^{-2}$).

Results

Figure 8.7 shows that the amperometric current increases at the specifically functionalized electrodes upon addition of 1 mM glucose in the solution on top of the array.

The sensitivity was determined by a calibration measurement and is shown in Figure 8.8. The mean sensitivity of all functionalized electrodes was $1.87 \pm 0.18 \text{ nA/mM}$ (mean, \pm std, $n=217$), which is $382 \mu\text{A mM}^{-1} \text{ cm}^{-2}$. The theoretical limit of detection is $96 \mu\text{M}$.

The glucose sensors could be used for up to a week on average by storing them in PBS at room temperature.

Discussion

The excellent sensitivity is comparable to the sensitivities achieved by the thick layers of drop coating (see Section 8.2.1). The high sensitivity may be attributed to a better loading of the enzymatic layer and to a much larger concentration of the enzyme used for functionalization. The higher limit of detection compared to the measurement in Section 8.2.1, is due to higher noise levels, when fast multiplexing is applied and the corresponding bandwidth. The possibility of spatial controlled electrode modification or functionalization is an important issue for large arrays, especially when several electrodes have to be modified differently. The non-optimized deposition protocol also leads to some non-specific adsorption of the enzyme at non-functionalized electrodes, which, however, produce significantly lower signals.

8.3.3 Monitoring glucose on the whole array

The whole array was functionalized to acquire electrochemical images of glucose concentration at high temporal resolution.

Materials and methods

The monomer o-aminophenol (2-aminophenol 99%; Alfa Aesar, Karlsruhe, Germany) was first solubilized in 0.1 M acetate buffer via sonication to make a 10 mM stock solution that was then vortexed for 20 minutes with an equal volume of the enzyme stock solution (5000 U/ml in DI water) to achieve the desired monomer and enzyme concentrations. The biosensing films were electrochemically deposited via cyclic voltammetry (potential range 0 – 0.9 V vs. Ag/AgCl/KCl (3M) at 50 mV/s, 7 cycles) using an external Pt counter electrode and an external Ag/AgCl (3M) reference electrode.

The electrochemical images were acquired by using the internal Pt counter electrode, an external Ag/AgCl (3M) reference electrode and the working electrode set to 0.65 V vs. Ag/AgCl.

Results

The response resulting from an injection of an aliquot of 1 μ l (30 mM) glucose into 3 ml PBS with the help of a microneedle can be seen in Figure 8.9. The microneedle was located in the upper half of the array, close to the surface. The image sequence had a frame rate of 69 fps. The top row shows consecutive frames of the video showing the beginning of the injection of glucose. The subsequent rows were extracted from the video at different points later in time.

Discussion

The image sequence shows evidence of the excellent response times achieved by the sensitive layer produced by electrodeposition. Spreading of the wave occurs to the lower left of the array, since the needle atop the array used for injection was slightly tilted. Fast changes of glucose concentrations due to diffusion, convection, or fast changes in the metabolism can be monitored. If less temporal resolution is needed, the frame rate can be reduced and lower detection limits can be achieved.

8.4 DISCUSSION

The measurements in this chapter provided some specific examples chosen from a wide field of possible applications.

Different functionalization schemes were used, different analytes were measured and different detection techniques were performed. It was proven that the measurement system can be

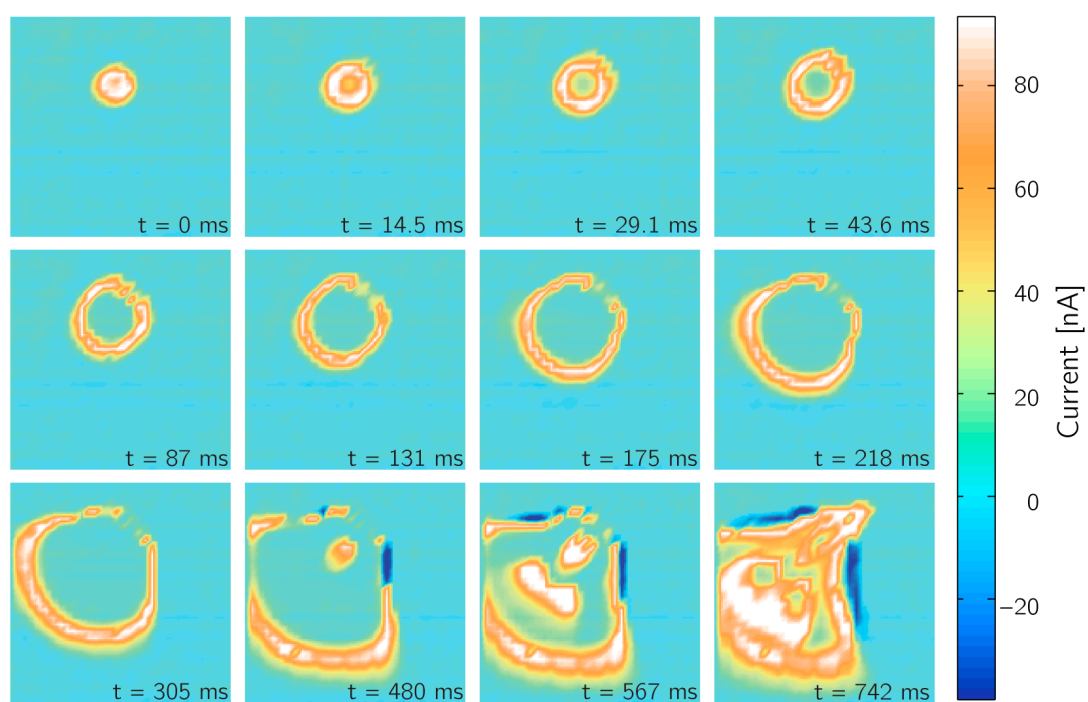


Figure 8.9: Glucose biosensor array - Response upon injection of an aliquot of glucose $1 \mu\text{l}$ (30 mM) glucose into 3 ml PBS. Recorded with 69 fps.

applied in very different scenarios.

In cases where the enzyme loading of the functionalized layer is low, sensitivities are low. The limit of detection is determined by the circuit noise and the electrochemical noise due to variations in the solution. The difference in sensitivities achieved for the detection of H_2O_2 and upon using enzymatic biosensors, based on oxidases, show that the efficiency of embedding enzymes could be improved. Many sophisticated biosensor schemes with promising properties were published, which may help to increase sensitivity (Hanefeld et al. 2009; Ronkainen et al. 2010; Wang 2008). One issue with biosensor functionalization methods is that they are usually established on millimeter-sized electrodes. Applying them on microelectrodes bears new challenges, as the protocols have to be adapted. Transferring microelectrode protocols to arrays is another challenge, since non-specific adsorption, limited diffusion and reduced spatial access play a major role in this setting. If the biosensitive layers can be improved, acquiring electrochemical images at high temporal resolution will be a great tool to monitor specific substances of interest in a cell culture or in tissue.

9

CONCLUSION

The design, fabrication, characterization and application of a CMOS microelectrode array chip for performing electrochemical measurements has been presented. The system integrates an array of 32x32 platinum electrodes, arranged with a pitch of 100 μm . 64 integrated direct-current sigma-delta converters allow for the detection of currents from 10 μA down to pA. The current is digitized by sigma-delta converters at a maximum resolution of 13.3 bits. The integrated noise is 220 fA for a bandwidth of 100 Hz, allowing for detection of pA currents. Currents can be continuously acquired at a bandwidth of up to 1 kHz, or the whole array can be read out rapidly at a frame rate of up to 90 Hz.

A flexible switch-matrix connects the electrodes to the ADCs. All necessary circuit blocks that are needed to perform electrochemical experiments were included in a monolithic implementation. All analog signals are generated and digitized on chip, and no external analog circuitry or digitization units are needed. This integration not only improves signal quality, since no weak analog signals have to be transmitted, but also helps to overcome the problem of routing many electrodes to their respective readout units, since digital multiplexing can be used.

A measurement system was built, which allows for conducting a broad variety of measurements with the very same system including amperometric images, voltammetric measurements, cyclic voltammetry, square wave voltammetry and differential pulse voltammetry, and the use of galvanostatic methods. Bi-potentiostatic or multi-potentiostatic (4 potential levels plus reference electrode) measurements can be performed by simultaneously using different sets of working electrodes.

The developed packaging scheme provides a biocompatible package that is viable for long-term measurements, and which protects the electronics against the harsh biological and chemical liquid environment. The packaging procedure is robust, and many chip systems can be packaged in parallel.

A new electrodeposition scheme, based on voltage pulses, has been developed. Uniform and reliable modifications of large microelectrode arrays can be performed. The electrodeposition scheme has been used to deposit different classes of materials, including metals and polymers.

9 CONCLUSION

9.1 CONSIDERATIONS FOR IMPROVEMENTS

The integrated circuits were designed to cover a large range of applications, from detection to functionalization. Several improvements could be implemented in the next generation design, while keeping the same requirements on the system level:

To provide the voltage range needed for electrochemical measurements, many of the circuits were required to have rail-to-rail characteristics. Removing the requirement for rail-to-rail characteristics would reduce area requirements and power consumption, since different amplifier architectures with lower power consumption (e.g. telescopic opamp) could be used. A simple way to circumvent the issue of the limited voltage range is to use an off-chip master potentiostat for controlling reference and counter electrodes. However, this would thwart the goal of a self-contained fully integrated system. If a high-voltage module of the CMOS process would be employed, the master potentiostat could be supplied with higher voltage, to provide the required voltage range for electrochemistry, while the current readouts would remain in the low-voltage domain. The working electrodes would remain at a fixed potential; the ability to perform bi-potentiostatic techniques would be limited.

Noise in the current design is dominated by the reference capacitors. Reducing the size of reference capacitors while increasing the clock frequency would improve the noise performance. One straightforward way to increase the frame rate would be to embed the multiplexing control logic on the chip, which would increase the fastest possible frame rate to up to 170 fps while using the same readout circuits.

The principle of using the electrode-electrolyte interface as a circuit element (like in SD1) for implementing a sigma-delta converter could be extended to the whole array, either by fast cycling through the array together with bit-wise decisions per electrode, or, in an incremental mode, by acquiring the bitstream to process one sample per electrode. The latter method would require only a fraction of the memory for implementing the decimation filters.

If the flexibility to perform various electroanalytical techniques and the ability to cover all scenarios with the integrated circuits should be kept, a hybrid system could be envisioned: a dedicated system for fast acquisition at low current levels and high channel count, another system covering larger currents (i.e. for electrodeposition) at low channel count, and the possibility to connect the sensing electrodes to a fixed potential to provide a path for fast polarization of the working electrodes.

The specifications were designed to cover the worst-case scenarios. Tailoring the design to a specific setting, including electrode size and functionalization, frame rate and signal bandwidth, voltage and current range, and the specific electroanalytical technique, would ease the design requirements. Passive circuit elements could be reduced in size, leading to smaller area and, due to a reduced load, to lower power consumption.

Keeping the voltage of the working electrodes constant would open the possibility for other circuit implementations. A sigma-delta-converter implementation based on inverters could be implemented. Using inverters would shrink area and power consumption, and channel count could be increased massively. In the extreme case, the sigma-delta converters may be

integrated into the pixel (Ignjatovic et al. 2012). A CMOS imager chip, based on incremental column-parallel sigma-delta converter with included decimation filters, was designed by Chae et al. (2011) and may be transferred to performing electroanalytical measurements.

One additional feature would be beneficial for performing experiments: measurement of the potentials of the reference electrode and counter electrode. Monitoring these voltages could immediately reveal problems during experiments, such as overload of the potentiostat, missing electrical contact to the electrolyte and large polarization of the counter electrode.

9.2 OUTLOOK

The developed measurement system has been characterized electrically and electrochemically. The system may be applied in the future to measure different analytes secreted from cells into the extracellular space using electroanalytical techniques. The CMOS chip allows for measuring of the concentrations of these analytes over the whole array multiple times per second. The spatial resolution is high enough to make a map of concentrations across a cell culture. Measurements of metabolites of individual cells in suspension or cell cultures grown on the chip may be performed, or changes in neurotransmitter levels in tissue slices upon electrical or chemical stimulation may be investigated. Different electroanalytical techniques may be employed together with novel sensor functionalizations to achieve selective and sensitive detection of the analyte of interest.

BIBLIOGRAPHY

- Amatore, C., S. Arbault, M. Guille, and F. Lemaître (2008). „Electrochemical monitoring of single cell secretion: vesicular exocytosis and oxidative stress.“ *Chemical reviews* 108.7, pp. 2585–621.
DOI: 10.1021/cr068062g (cit. on pp. 2, 26).
- Augustyniak, M., C. Paulus, R. Brederlow, N. Persike, G. Hartwich, D. Schmitt-Landsiedel, and R. Thewes (2006). „A 24x16 CMOS-Based Chronocoulometric DNA Microarray.“ in: *2006 IEEE International Solid State Circuits Conference - Digest of Technical Papers*. IEEE: New York, NY, pp. 59–68.
DOI: 10.1109/ISSCC.2006.1696034 (cit. on p. 33).
- Bakker, E. (2004). „Electrochemical sensors.“ *Analytical chemistry* 76.12, pp. 3285–98.
DOI: 10.1021/ac049580z (cit. on p. 1).
- Bard, A. J. and L. R. Faulkner (2001). *Electrochemical methods : fundamentals and applications*. 2nd. New York: Wiley-VCH Verlag GmbH & Co. KGaA, p. 833 (cit. on pp. 9, 53, 67).
- Bashir, R. (2004). „BioMEMS: state-of-the-art in detection, opportunities and prospects.“ *Advanced drug delivery reviews* 56.11, pp. 1565–86.
DOI: 10.1016/j.addr.2004.03.002 (cit. on p. 2).
- Bellin, D. L., H. Sakhtah, J. K. Rosenstein, P. M. Levine, J. Thimot, K. Emmett, L. E. P. Dietrich, and K. L. Shepard (2014). „Integrated circuit-based electrochemical sensor for spatially resolved detection of redox-active metabolites in biofilms.“ *Nature communications* 5, p. 3256.
DOI: 10.1038/ncomms4256 (cit. on pp. 33, 44, 45).
- Bobacka, J., A. Lewenstam, and A. Ivaska (2000). „Electrochemical impedance spectroscopy of oxidized poly(3,4-ethylenedioxythiophene) film electrodes in aqueous solutions.“ *Journal of Electroanalytical Chemistry* 489.1-2, pp. 17–27.
DOI: 10.1016/S0022-0728(00)00206-0 (cit. on p. 82).
- Bockris, J. O., A. K. Reddy, and M. E. Gamboa-Aldeco (2000). *Modern Electrochemistry 2A Fundamentals of Electrodics*. 2nd. Springer Berlin Heidelberg, p. 763 (cit. on pp. 9, 13, 26).
- Bond, A. M., D. Luscombe, K. B. Oldham, and C. G. Zoski (1988). „A comparison of the chronoamperometric response at inlaid and recessed disc microelectrodes.“ *Journal of Electroanalytical Chemistry and Interfacial Electrochemistry* 249.1-2, pp. 1–14.
DOI: 10.1016/0022-0728(88)80345-0 (cit. on p. 67).
- Chae, Y., J. Cheon, S. Lim, M. Kwon, K. Yoo, W. Jung, D.-H. Lee, S. Ham, and G. Han (2011). „A 2.1 M Pixels, 120 Frame/s CMOS Image Sensor With Column-Parallel Delta-

Bibliography

- Sigma ADC Architecture." *IEEE Journal of Solid-State Circuits* 46.1, pp. 236–247.
DOI: 10.1109/JSSC.2010.2085910 (cit. on p. 105).
- Cherry, J. A. and M. W. Snelgrove (1999). *Continuous-Time Delta-Sigma Modulators for High-Speed A/D Conversion*. Springer Netherlands, p. 280.
DOI: 10.1007/b117617 (cit. on p. 32).
- Clark, L. C. and C. Lyons (1962). „Electrode systems for continuous monitoring in cardiovascular surgery." *Annals of the New York Academy of Sciences* 102.1, pp. 29–45.
DOI: 10.1111/j.1749-6632.1962.tb13623.x (cit. on p. 2).
- Dharuman, V., T. Grunwald, E. Nebling, J. Albers, L. Blohm, and R. Hintsche (2005). „Label-free impedance detection of oligonucleotide hybridisation on interdigitated ultramicroelectrodes using electrochemical redox probes." *Biosensors & bioelectronics* 21.4, pp. 645–54.
DOI: 10.1016/j.bios.2004.12.020 (cit. on p. 3).
- Vo-Dinh, T. and B. Cullum (2000). „Biosensors and biochips: advances in biological and medical diagnostics." *Fresenius' journal of analytical chemistry* 366.6-7, pp. 540–51 (cit. on p. 2).
- Doña Rodríguez, J. M., J. A. Herrera Melián, and J. Pérez Peña (2000). „Determination of the Real Surface Area of Pt Electrodes by Hydrogen Adsorption Using Cyclic Voltammetry." *Journal of Chemical Education* 77.9, p. 1195.
DOI: 10.1021/ed077p1195 (cit. on p. 68).
- Drummond, T. G., M. G. Hill, and J. K. Barton (2003). „Electrochemical DNA sensors." *Nature biotechnology* 21.10, pp. 1192–9.
DOI: 10.1038/nbt873 (cit. on pp. 2, 11, 79).
- Franks, W., I. Schenker, P. Schmutz, and A. Hierlemann (2005). „Impedance characterization and modeling of electrodes for biomedical applications." *IEEE transactions on bio-medical engineering* 52.7, pp. 1295–302.
DOI: 10.1109/TBME.2005.847523 (cit. on pp. 13, 26, 51).
- Frey, A., M. Jenkner, M. Schienle, C. Paulus, B. Holzapfl, P. Schindler-Bauer, F. Hofmann, D. Kuhlmeier, J. Krause, J. Albers, W. Gumbrecht, D. Schmitt-Landsiedel, and R. Thewes (2003). „Design of an integrated potentiostat circuit for CMOS bio sensor chips." in: *Proceedings of the 2003 International Symposium on Circuits and Systems, 2003. ISCAS '03*. Vol. 5. IEEE, pages.
DOI: 10.1109/ISCAS.2003.1206159 (cit. on p. 25).
- Frey, O., T. Holtzman, R. M. McNamara, D. E. H. Theobald, P. D. van der Wal, N. F. de Rooij, J. W. Dalley, and M. Koudelka-Hep (2010). „Enzyme-based choline and L-glutamate biosensor electrodes on silicon microprobe arrays." *Biosensors & bioelectronics* 26.2, pp. 477–84.
DOI: 10.1016/j.bios.2010.07.073 (cit. on p. 89).
- Fritz, J., E. B. Cooper, S. Gaudet, P. K. Sorger, and S. R. Manalis (2002). „Electronic detection of DNA by its intrinsic molecular charge." *Proceedings of the National Academy of Sciences of the United States of America* 99.22, pp. 14142–6.
DOI: 10.1073/pnas.232276699 (cit. on p. 3).

- Guerrieri, A., G. De Benedetto, F. Palmisano, and P. Zambonin (1998). „Electrosynthesized non-conducting polymers as permselective membranes in amperometric enzyme electrodes: a glucose biosensor based on a co-crosslinked glucose oxidase/overoxidized polypyrrole bilayer.“ *Biosensors and Bioelectronics* 13.1, pp. 103–112.
DOI: 10.1016/S0956-5663(97)00064-X (cit. on p. 82).
- Guerrieri, A., R. Ciriello, and D. Centonze (2009). „Permselective and enzyme-entrapping behaviours of an electropolymerized, non-conducting, poly(o-aminophenol) thin film-modified electrode: a critical study.“ *Biosensors & bioelectronics* 24.6, pp. 1550–6.
DOI: 10.1016/j.bios.2008.08.004 (cit. on p. 77).
- Guo, J. and E. Lindner (2009). „Cyclic voltammograms at coplanar and shallow recessed microdisk electrode arrays: guidelines for design and experiment.“ *Analytical chemistry* 81.1, pp. 130–8.
DOI: 10.1021/ac801592j (cit. on p. 17).
- Hamann, C. H., A. Hamnett, and W. Vielstich (2007). *Electrochemistry*. 2nd. Wiley-VCH Verlag GmbH & Co. KGaA, p. 550 (cit. on pp. 9, 15).
- Hanefeld, U., L. Gardossi, and E. Magner (2009). „Understanding enzyme immobilisation.“ *Chemical Society reviews* 38.2, pp. 453–68.
DOI: 10.1039/b711564b (cit. on pp. 73, 101).
- Harrison, R. R., P. T. Watkins, R. J. Kier, R. O. Lovejoy, D. J. Black, B. Greger, and F. Solzbacher (2007). „A Low-Power Integrated Circuit for a Wireless 100-Electrode Neural Recording System.“ *IEEE Journal of Solid-State Circuits* 42.1, pp. 123–133.
DOI: 10.1109/JSSC.2006.886567 (cit. on p. 3).
- Hassibi, A. and T. H. Lee (2006). „A Programmable 0.18 μ m CMOS Electrochemical Sensor Microarray for Biomolecular Detection.“ *IEEE Sensors Journal* 6.6, pp. 1380–1388.
DOI: 10.1109/JSEN.2006.883904 (cit. on p. 59).
- Heer, F., M. Keller, G. Yu, J. Janata, M. Josowicz, and A. Hierlemann (2008). „CMOS Electro-Chemical DNA-Detection Array with On-Chip ADC.“ in: *2008 IEEE International Solid-State Circuits Conference - Digest of Technical Papers*. IEEE: New York, NY, pp. 168–604.
DOI: 10.1109/ISSCC.2008.4523110 (cit. on pp. 27, 33, 43, 44).
- Heien, M. L. A. V., M. A. Johnson, and R. M. Wightman (2004). „Resolving Neurotransmitters Detected by Fast-Scan Cyclic Voltammetry.“ *Analytical Chemistry* 76.19, pp. 5697–5704.
DOI: 10.1021/ac0491509 (cit. on pp. 2, 62).
- Heinze, J. (1993). „Ultramicroelectrodes in Electrochemistry.“ *Angewandte Chemie International Edition in English* 32.9, pp. 1268–1288.
DOI: 10.1002/anie.199312681 (cit. on pp. 2, 67).
- Herwik, S., S. Kisban, A. A. A. Aarts, K. Seidl, G. Girardeau, K. Benchenane, M. B. Zugaro, S. I. Wiener, O. Paul, H. P. Neves, and P. Ruther (2009). „Fabrication technology for silicon-based microprobe arrays used in acute and sub-chronic neural recording.“ *Journal*

Bibliography

- of Micromechanics and Microengineering* 19.7, p. 074008.
DOI: 10.1088/0960-1317/19/7/074008 (cit. on p. 3).
- Hierlemann, A. and H. Baltes (2003). „CMOS-based chemical microsensors.“ *The Analyst* 128.1, pp. 15–28.
DOI: 10.1039/b208563c (cit. on p. 51).
- Hoare, J. P. (1984). „A Cyclic Voltammetric Study of the Gold-Oxygen System.“ *Journal of The Electrochemical Society* 131.8, p. 1808.
DOI: 10.1149/1.2115966 (cit. on p. 81).
- Hochstetler, S. E., M. Puopolo, S. Gustincich, E. Raviola, and R. M. Wightman (2000). „Real-Time Amperometric Measurements of Zeptomole Quantities of Dopamine Released from Neurons.“ *Analytical Chemistry* 72.3, pp. 489–496.
DOI: 10.1021/ac991119x (cit. on p. 2).
- Hogenauer, E. (1981). „An economical class of digital filters for decimation and interpolation.“ *IEEE Transactions on Acoustics, Speech, and Signal Processing* 29.2, pp. 155–162.
DOI: 10.1109/TASSP.1981.1163535 (cit. on p. 46).
- Hogervorst, R., J. Tero, R. Eschauzier, and J. Huijsing (1994). „A compact power-efficient 3 V CMOS rail-to-rail input/output operational amplifier for VLSI cell libraries.“ *IEEE Journal of Solid-State Circuits* 29.12, pp. 1505–1513.
DOI: 10.1109/4.340424 (cit. on p. 24).
- Huang, X.-J., A. M. O'Mahony, and R. G. Compton (2009). „Microelectrode arrays for electrochemistry: approaches to fabrication.“ *Small (Weinheim an der Bergstrasse, Germany)* 5.7, pp. 776–88.
DOI: 10.1002/smll.200801593 (cit. on p. 51).
- Hudak, E. M., J. T. Mortimer, and H. B. Martin (2010). „Platinum for neural stimulation: voltammetry considerations.“ *Journal of neural engineering* 7.2, p. 26005.
DOI: 10.1088/1741-2560/7/2/026005 (cit. on p. 23).
- Hwang, S., C. N. LaFratta, V. Agarwal, X. (Yu, D. R. Walt, and S. Sonkusale (2009). „CMOS Microelectrode Array for Electrochemical Lab-on-a-Chip Applications.“ *IEEE Sensors Journal* 9.6, pp. 609–615.
DOI: 10.1109/JSEN.2009.2020193 (cit. on pp. 33, 51).
- Ignjatovic, Z., D. Maricic, and M. F. Bocko (2012). „Low Power, High Dynamic Range CMOS Image Sensor Employing Pixel-Level Oversampling Sigma-Delta Analog-to-Digital Conversion.“ *IEEE Sensors Journal* 12.4, pp. 737–746.
DOI: 10.1109/JSEN.2011.2158818 (cit. on p. 105).
- Ino, K., Y. Kanno, T. Nishijo, H. Komaki, Y. Yamada, S. Yoshida, Y. Takahashi, H. Shiku, and T. Matsue (2014). „Densified electrochemical sensors based on local redox cycling between vertically separated electrodes in substrate generation/chip collection and extended feedback modes.“ *Analytical chemistry* 86.8, pp. 4016–23.
DOI: 10.1021/ac500435d (cit. on p. 2).
- Inoue, K. Y., M. Matsudaira, R. Kubo, M. Nakano, S. Yoshida, S. Matsuzaki, A. Suda, R. Kunikata, T. Kimura, R. Tsurumi, T. Shioya, K. Ino, H. Shiku, S. Satoh, M. Esashi,

- and T. Matsue (2012). „LSI-based amperometric sensor for bio-imaging and multi-point biosensing.“ *Lab on a chip* 12.18, pp. 3481–90.
DOI: 10.1039/c2lc40323d (cit. on pp. 33, 44, 45, 59, 96).
- Johns, D. A. and K. Martin (1997). *Analog integrated circuit design*. John Wiley & Sons, p. 706 (cit. on p. 28).
- Johnson, K. W. (1991). „Reproducible electrodeposition of biomolecules for the fabrication of miniature electroenzymatic biosensors.“ *Sensors and Actuators B: Chemical* 5.1-4, pp. 85–89.
DOI: 10.1016/0925-4005(91)80225-9 (cit. on p. 74).
- Joo, S. and R. B. Brown (2008). „Chemical sensors with integrated electronics.“ *Chemical reviews* 108.2, pp. 638–51.
DOI: 10.1021/cr068113+ (cit. on p. 3).
- Jorcin, J.-B., M. E. Orazem, N. Pébère, and B. Tribollet (2006). „CPE analysis by local electrochemical impedance spectroscopy.“ *Electrochimica Acta* 51.8-9, pp. 1473–1479.
DOI: 10.1016/j.electacta.2005.02.128 (cit. on p. 13).
- Kalantari, R., R. Cantor, H. Chen, G. Yu, J. Janata, and M. Josowicz (2010). „Label-free voltammetric detection using individually addressable oligonucleotide microelectrode arrays.“ *Analytical chemistry* 82.21, pp. 9028–33.
DOI: 10.1021/ac102002k (cit. on p. 2).
- Kim, B. N., A. D. Herbst, S. J. Kim, B. A. Minch, and M. Lindau (2013). „Parallel recording of neurotransmitters release from chromaffin cells using a 10×10 CMOS IC potentiostat array with on-chip working electrodes.“ *Biosensors & bioelectronics* 41, pp. 736–44.
DOI: 10.1016/j.bios.2012.09.058 (cit. on pp. 33, 44, 45, 96).
- Kisler, K., B. N. Kim, X. Liu, K. Berberian, Q. Fang, C. J. Mathai, S. Gangopadhyay, K. D. Gillis, and M. Lindau (2012). „Transparent Electrode Materials for Simultaneous Amperometric Detection of Exocytosis and Fluorescence Microscopy.“ *Journal of biomaterials and nanobiotechnology* 3.2A, pp. 243–253 (cit. on p. 2).
- Kruppa, P., A. Frey, I. Kuehne, M. Schienle, N. Persike, T. Kratzmueller, G. Hartwich, and D. Schmitt-Landsiedel (2010). „A digital CMOS-based 24×16 sensor array platform for fully automatic electrochemical DNA detection.“ *Biosensors & bioelectronics* 26.4, pp. 1414–9.
DOI: 10.1016/j.bios.2010.07.070 (cit. on pp. 33, 43, 44, 59).
- Lavacchi, A., U. Bardi, C. Borri, S. Caporali, A. Fossati, and I. Perissi (2009). „Cyclic voltammetry simulation at microelectrode arrays with COMSOL Multiphysics®.“ *Journal of Applied Electrochemistry* 39.11, pp. 2159–2163.
DOI: 10.1007/s10800-009-9797-2 (cit. on p. 17).
- Levine, P. M., P. Gong, R. Levicky, and K. L. Shepard (2008). „Active CMOS Sensor Array for Electrochemical Biomolecular Detection.“ *IEEE Journal of Solid-State Circuits* 43.8, pp. 1859–1871.
DOI: 10.1109/JSSC.2008.925407 (cit. on pp. 33, 43, 44).
- Li, L., X. Liu, W. A. Qureshi, and A. J. Mason (2011). „CMOS Amperometric Instrumentation and Packaging for Biosensor Array Applications.“ *IEEE Transactions on Biomedical*

Bibliography

- Circuits and Systems* 5.5, pp. 439–448.
DOI: 10.1109/TBCAS.2011.2171339 (cit. on p. 59).
- Liu, X., S. Barizuddin, W. Shin, C. J. Mathai, S. Gangopadhyay, and K. D. Gillis (2011). „Microwell device for targeting single cells to electrochemical microelectrodes for high-throughput amperometric detection of quantal exocytosis.“ *Analytical chemistry* 83.7, pp. 2445–51.
DOI: 10.1021/ac1033616 (cit. on pp. 2, 59).
- Lowry, J. P., K. McAteer, S. S. El Atrash, A. Duff, and R. D. O'Neill (1994). „Characterization of Glucose Oxidase-Modified Poly(phenylenediamine)-Coated Electrodes in vitro and in vivo: Homogeneous Interference by Ascorbic Acid in Hydrogen Peroxide Detection.“ *Analytical Chemistry* 66.10, pp. 1754–1761.
DOI: 10.1021/ac00082a025 (cit. on p. 83).
- Lyons, R. G. (2010). *Understanding Digital Signal Processing*. 3rd. Prentice Hall, p. 984 (cit. on p. 46).
- Madangopal, R., M. Stensberg, M. Porterfield, J. Rickus, and N. Pulliam (2012). „Directed enzyme deposition via electroactive polymer-based nanomaterials for multi-analyte amperometric biosensors.“ in: *2012 IEEE Sensors*. IEEE, pp. 1–4.
DOI: 10.1109/ICSENS.2012.6411166 (cit. on p. 81).
- Malitesta, C., F. Palmisano, L. Torsi, and P. G. Zambonin (1990). „Glucose fast-response amperometric sensor based on glucose oxidase immobilized in an electropolymerized poly(o-phenylenediamine) film.“ *Analytical chemistry* 62.24, pp. 2735–40 (cit. on p. 83).
- Manickam, A., R. Singh, N. Wood, B. Li, A. Ellington, and A. Hassibi (2012). „A fully-electronic charge-based DNA sequencing CMOS biochip.“ in: *2012 Symposium on VLSI Circuits (VLSIC)*. IEEE: New York, NY, pp. 126–127.
DOI: 10.1109/VLSIC.2012.6243822 (cit. on p. 33).
- Mann, M. a., J. C. Helfrick, and L. a. Bottomley (2014). „Diagnostic Criteria for the Characterization of Quasireversible Electron Transfer Reactions by Cyclic Square Wave Voltammetry.“ *Analytical chemistry* 1.
DOI: 10.1021/ac501550j (cit. on p. 64).
- Martin, S., F. Gebara, B. Larivee, and R. Brown (2005). „A CMOS-integrated microinstrument for trace detection of heavy metals.“ *IEEE Journal of Solid-State Circuits* 40.12, pp. 2777–2786.
DOI: 10.1109/JSSC.2005.858478 (cit. on pp. 25, 33).
- Martins, R. P. (2011). „Two Stage Operational Amplifiers: Power and Area Efficient Frequency Compensation for Driving a Wide Range of Capacitive Load.“ *IEEE Circuits and Systems Magazine* 11.1, pp. 26–42.
DOI: 10.1109/MCAS.2010.939783 (cit. on p. 25).
- Mason, A., Y. Huang, C. Yang, and J. Zhang (2007). „Amperometric Readout and Electrode Array Chip for Bioelectrochemical Sensors.“ in: *2007 IEEE International Symposium on Circuits and Systems*. IEEE: New York, NY, pp. 3562–3565.
DOI: 10.1109/ISCAS.2007.378452 (cit. on p. 33).

- Mazhab-Jafari, H., L. Soleymani, and R. Genov (2012). „16-Channel CMOS impedance spectroscopy DNA analyzer with dual-slope multiplying ADCs.“ *IEEE transactions on biomedical circuits and systems* 6.5, pp. 468–78.
DOI: 10.1109/TBCAS.2012.2226334 (cit. on p. 33).
- Meitzen, J., K. R. Pflepsen, C. M. Stern, R. L. Meisel, and P. G. Mermelstein (2011). „Measurements of neuron soma size and density in rat dorsal striatum, nucleus accumbens core and nucleus accumbens shell: differences between striatal region and brain hemisphere, but not sex.“ *Neuroscience letters* 487.2, pp. 177–81.
DOI: 10.1016/j.neulet.2010.10.017 (cit. on p. 21).
- Mollazadeh, M., K. Murari, G. Cauwenberghs, and N. V. Thakor (2009). „Wireless Micropower Instrumentation for Multimodal Acquisition of Electrical and Chemical Neural Activity.“ *IEEE Transactions on Biomedical Circuits and Systems* 3.6, pp. 388–397.
DOI: 10.1109/TBCAS.2009.2031877 (cit. on p. 33).
- Nazari, M. H., H. Mazhab-Jafari, L. Leng, A. Guenther, and R. Genov (2013). „CMOS neurotransmitter microarray: 96-channel integrated potentiostat with on-die microsenors.“ *IEEE transactions on biomedical circuits and systems* 7.3, pp. 338–48.
DOI: 10.1109/TBCAS.2012.2203597 (cit. on pp. 33, 43, 44).
- Newman, J. (1966). „Resistance for Flow of Current to a Disk.“ *Journal of The Electrochemical Society* 113.5, p. 501.
DOI: 10.1149/1.2424003 (cit. on p. 18).
- Odenthal, K. J. and J. J. Gooding (2007). „An introduction to electrochemical DNA biosensors.“ *The Analyst* 132.7, pp. 603–10.
DOI: 10.1039/b701816a (cit. on p. 11).
- Ohnuki, Y., H. Matsuda, T. Ohsaka, and N. Oyama (1983). „Permselectivity of films prepared by electrochemical oxidation of phenol and amino-aromatic compounds.“ *Journal of Electroanalytical Chemistry and Interfacial Electrochemistry* 158.1, pp. 55–67.
DOI: 10.1016/S0022-0728(83)80338-6 (cit. on pp. 77, 83).
- Pavan, S. (2011). „Alias Rejection of Continuous-Time Delta Sigma Modulators With Switched-Capacitor Feedback DACs.“ *IEEE Transactions on Circuits and Systems I: Regular Papers* 58.2, pp. 233–243.
DOI: 10.1109/TCSI.2010.2071930 (cit. on p. 32).
- Petrovic, S. (2000). „Cyclic Voltammetry of Hexachloroiridate(IV): An Alternative to the Electrochemical Study of the Ferricyanide Ion.“ *The Chemical Educator* 5.5, pp. 231–235.
DOI: 10.1007/s00897000416a (cit. on p. 67).
- Piccolo, F., S. Gosso, E. Vittone, A. Pasquarelli, E. Carbone, P. Olivero, and V. Carabelli (2013). „A new diamond biosensor with integrated graphitic microchannels for detecting quantal exocytic events from chromaffin cells.“ *Advanced materials (Deerfield Beach, Fla.)* 25.34, pp. 4696–700.
DOI: 10.1002/adma.201300710 (cit. on p. 2).
- Pourbaix, B. M. J. N., J. V. Muylder, and N. D. Zoubov (1959). „Electrochemical Properties of the Platinum Metals.“ *Platinum Metals Review* 3.2, pp. 47–53 (cit. on p. 76).

Bibliography

- Raba, J. and H. A. Mottola (2006). „Glucose Oxidase as an Analytical Reagent.“ *Critical Reviews in Analytical Chemistry* 25.1, pp. 1–42.
DOI: 10.1080/10408349508050556 (cit. on p. 91).
- Reddy, S., S. Higson, and P. Vadgama (1994). „Enzyme and other biosensors: evolution of a technology.“ *Engineering Science & Education Journal* 3.1, pp. 41–48.
DOI: 10.1049/esej:19940105 (cit. on p. 2).
- Robinson, D. L., A. Hermans, A. T. Seipel, and R. M. Wightman (2008). „Monitoring rapid chemical communication in the brain.“ *Chemical reviews* 108.7, pp. 2554–84.
DOI: 10.1021/cr068081q (cit. on p. 2).
- Roham, M., D. P. Daberkow, E. S. Ramsson, D. P. Covey, S. Pakdeeronachit, P. A. Garriss, and P. Mohseni (2008). „A Wireless IC for Wide-Range Neurochemical Monitoring Using Amperometry and Fast-Scan Cyclic Voltammetry.“ *IEEE transactions on biomedical circuits and systems* 2.1, pp. 3–9.
DOI: 10.1109/TBCAS.2008.918282 (cit. on p. 33).
- Ronkainen, N. J., H. B. Halsall, and W. R. Heineman (2010). „Electrochemical biosensors.“ *Chemical Society reviews* 39.5, pp. 1747–63.
DOI: 10.1039/b714449k (cit. on pp. 2, 61, 101).
- Rothe, J., O. Frey, A. Stettler, Y. Chen, and A. Hierlemann (2012). „CMOS chip for electrochemical monitoring of the metabolic activity of biological cells.“ in: *2012 IEEE Sensors*. IEEE: New York, NY, pp. 1–4.
DOI: 10.1109/ICSENS.2012.6411351 (cit. on p. 5).
- Rothe, J., O. Frey, A. Stettler, Y. Chen, and A. Hierlemann (2014). „Fully Integrated CMOS Microsystem for Electrochemical Measurements on 32×32 Working Electrodes at 90 Frames Per Second.“ *Analytical chemistry* 86.13, pp. 6425–32.
DOI: 10.1021/ac500862v (cit. on p. 5).
- Rothe, J., M. K. Lewandowska, F. Heer, O. Frey, and A. Hierlemann (2011). „Multi-target electrochemical biosensing enabled by integrated CMOS electronics.“ *Journal of Micromechanics and Microengineering* 21.5, p. 054010.
DOI: 10.1088/0960-1317/21/5/054010 (cit. on p. 5).
- Rothe, J., R. Madangopal, O. Frey, J. Rickus, and A. Hierlemann (2014). „A robust voltage-pulse based scheme for electrodeposition on large platinum microelectrode arrays.“ *in preparation* (cit. on p. 5).
- Saito, Y. (1968). „A Theoretical Study on the Diffusion Current at the Stationary Electrodes of Circular and Narrow Band Types.“ *Review of Polarography* 15.6, pp. 177–187.
DOI: 10.5189/revpolarography.15.177 (cit. on p. 16).
- Samba, R., K. Fuchsberger, I. Matychyn, S. Epple, L. Kiesel, A. Stett, W. Schuhmann, and M. Stelzle (2014). „Application of PEDOT-CNT Microelectrodes for Neurotransmitter Sensing.“ *Electroanalysis*, n/a–n/a.
DOI: 10.1002/e1an.201300547 (cit. on pp. 81, 89).

- Sassolas, A., B. D. Leca-Bouvier, and L. J. Blum (2008). „DNA biosensors and microarrays.“ *Chemical reviews* 108.1, pp. 109–39.
DOI: 10.1021/cr0684467 (cit. on pp. 2, 79).
- Schienze, M., C. Paulus, A. Frey, F. Hofmann, B. Holzapfl, P. Schindler-Bauer, and R. Thewes (2004). „A fully electronic DNA sensor with 128 positions and in-pixel A/D conversion.“ *IEEE Journal of Solid-State Circuits* 39.12, pp. 2438–2445.
DOI: 10.1109/JSSC.2004.837084 (cit. on pp. 33, 43, 44).
- Schreier, R. and G. Temes (2004). *Understanding Delta-Sigma Data Converters*. 1st ed. Wiley-IEEE Press, p. 464 (cit. on p. 47).
- Sen, M., K. Ino, K. Y. Inoue, T. Arai, T. Nishijo, A. Suda, R. Kunikata, H. Shiku, and T. Matsue (2013). „LSI-based amperometric sensor for real-time monitoring of embryoid bodies.“ *Biosensors & bioelectronics* 48, pp. 12–8.
DOI: 10.1016/j.bios.2013.03.069 (cit. on p. 96).
- Spiro, M. (1964). „Standard exchange current densities of redox systems at platinum electrodes.“ *Electrochimica Acta* 9.11, pp. 1531–1537.
DOI: 10.1016/0013-4686(64)85032-5 (cit. on p. 15).
- Srinorakutara, T. (1998). „Determination of yeast cell wall thickness and cell diameter using new methods.“ *Journal of Fermentation and Bioengineering* 86.3, pp. 253–260.
DOI: 10.1016/S0922-338X(98)80002-0 (cit. on p. 21).
- Stanacevic, M., K. Murari, A. Rege, G. Cauwenberghs, and N. V. Thakor (2007). „VLSI Potentiostat Array With Oversampling Gain Modulation for Wide-Range Neurotransmitter Sensing.“ *IEEE Transactions on Biomedical Circuits and Systems* 1.1, pp. 63–72.
DOI: 10.1109/TBCAS.2007.893176 (cit. on p. 33).
- Thewes, R. (2007). „CMOS chips for bio molecule sensing purposes.“ in: *2007 2nd International Workshop on Advances in Sensors and Interface*. IEEE, pp. 1–6.
DOI: 10.1109/IWASI.2007.4420000 (cit. on p. 51).
- Vidal, J.-C., E. Garcia-Ruiz, and J.-R. Castillo (2003). „Recent Advances in Electropolymerized Conducting Polymers in Amperometric Biosensors.“ *Microchimica Acta* 143.2-3, pp. 93–111.
DOI: 10.1007/s00604-003-0067-4 (cit. on pp. 75, 81).
- Wang, J. (2002). „Electrochemical nucleic acid biosensors.“ *Analytica Chimica Acta* 469.1, pp. 63–71.
DOI: 10.1016/S0003-2670(01)01399-X (cit. on pp. 2, 79).
- Wang, J. (2006). „Electrochemical biosensors: towards point-of-care cancer diagnostics.“ *Biosensors & bioelectronics* 21.10, pp. 1887–92.
DOI: 10.1016/j.bios.2005.10.027 (cit. on p. 2).
- Wang, J. (2008). „Electrochemical glucose biosensors.“ *Chemical reviews* 108.2, pp. 814–25.
DOI: 10.1021/cr068123a (cit. on pp. 92, 101).
- Warsinke, a., a. Benkert, and F. W. Scheller (2000). „Electrochemical immunoassays.“ *Fresenius' journal of analytical chemistry* 366.6-7, pp. 622–34 (cit. on p. 2).

Bibliography

- Wightman, R. M. (2006). „Detection technologies. Probing cellular chemistry in biological systems with microelectrodes.“ *Science (New York, N.Y.)* 311.5767, pp. 1570–4.
DOI: 10.1126/science.1120027 (cit. on pp. 2, 63).
- Wise, K., D. Anderson, J. Hetke, D. Kipke, and K. Najafi (2004). „Wireless Implantable Microsystems: High-Density Electronic Interfaces to the Nervous System.“ *Proceedings of the IEEE* 92.1, pp. 76–97.
DOI: 10.1109/JPROC.2003.820544 (cit. on p. 3).
- Yang, X., J. Kirsch, E. V. Olsen, J. W. Fergus, and A. L. Simonian (2013). „Anti-fouling PE-DOT:PSS modification on glassy carbon electrodes for continuous monitoring of tricresyl phosphate.“ *Sensors and Actuators B: Chemical* 177, pp. 659–667.
DOI: 10.1016/j.snb.2012.11.057 (cit. on p. 81).
- Yotter, R. and D. Wilson (2004). „Sensor Technologies for Monitoring Metabolic Activity in Single Cells—Part II: Nonoptical Methods and Applications.“ *IEEE Sensors Journal* 4.4, pp. 412–429.
DOI: 10.1109/JSEN.2004.830954 (cit. on p. 2).
- Zhang, B., K. L. Adams, S. J. Lubner, D. J. Eves, M. L. Heien, and A. G. Ewing (2008). „Spatially and temporally resolved single-cell exocytosis utilizing individually addressable carbon microelectrode arrays.“ *Analytical chemistry* 80.5, pp. 1394–400.
DOI: 10.1021/ac702409s (cit. on p. 2).

ACKNOWLEDGMENTS

First, I would like to show my gratitude to Prof. Andreas Hierlemann for giving me the opportunity to pursue my PhD thesis at the Bio Engineering Laboratory (BEL). I would like to acknowledge the considerable input from Prof. Andreas Hierlemann with his professional advice and for granting so much freedom to the members of his group. I would like to thank Prof. Roland Thewes for being co-referee, working through the thesis and his valuable input. Olivier Frey served not only as a co-referee, but also as a guide and tutor to me for the second half of my thesis. I would especially like to thank him for his company as my "uncle", for the very in-depth cogitation of my problems. He set an impressive example of how to work with endless endurance, while keeping the quality of work at a very high level.

It was a pleasure to work at BEL with so many talented and motivated people. I would like to point out some of them which were more involved in my efforts of pursuing the PhD:

I would like to thank Marta Lewandowska, with whom I was working together in the beginning of my PhD. She always had an open ear and was helpful in proof reading. I appreciated her open mind, especially giving constructive criticism. Alexander Stettler not only carried out the post-processing work, but also offered his huge experience and knowledge base for various inherent problems. Thanks to my office mate Paolo Livi for sharing all the good and tedious times and some good advice in Italian-style presentations. Thanks to Jan Müller for encouraging coffee breaks and sharing his skills in digital design and software programming. Yihui Chen was giving me support during the circuit design phase with his in-depth knowledge in analog circuit design. I want to thank Marco Ballini, Niels Haandbaek, YongHong Tao and Felix Franke for many fruitful technical discussions, Michele Fiscella, Ian Jones, Wei Gong, David Jäckel, Tom Russell and Douglas Bakkum for giving me support and teaching me some skills in biological lab work. I would like to thank Sandra Leber and Steven Preisig for pursuing their Semester projects with me. I am very grateful to Sadik Hafizovic and Flavio Heer for bringing me to the BEL, and Urs Frey for the enjoyable atmosphere sharing the office and later for the fruitful collaboration. It was great luck of having met Tarun Madangopal from Purdue University: his visit and the team work on transferring experimental protocols onto the CMOS chip was very encouraging. I would like to thank my collaborators Giulio Navarra, for his trials on recognizing bacteria strands with the system and Florent Seichepine for using the system with his experiments on carbon nanotubes. I am grateful to Prof. Jiri Janata and Mira Josowicz from Georgia Tech for their hospitality during the visit in Atlanta and for teaching me first steps in practical electrochemistry. I would like to thank the technical and administrative stuff at the D-BSSE, which provide a great infrastructure by their work.

Finally, I am very grateful for the support of my family; to my parents, who supported me during all my life, and to Anna my love.

Bibliography

To all the people mentioned above, I am very grateful in their assistance in my PhD endeavor and remain indebted to them in the future.

ACRONYMS

AA	ascorbic acid. 82–84
ADC	analog-to-digital converter. 4
CE	counter or auxiliary electrode. 13, 14, 18, 23, 25, 52–54
CIC	cascaded integrator-comb filter. 46, 47
CMOS	complementary-metal-oxide semiconductor. 3, 4, 21
CPE	constant-phase element. 13, 18
CV	cyclic voltammogram. 26, 62–64, 67, 69, 70, 75, 81, 82
DA	dopamine. 82–84
DAC	digital-to-analog converter. 71
DL	double layer. 12, 18, 22, 23, 26, 62–64, 68, 78
DPV	differential pulse voltammetry. 63, 65
EAA	electrochemically aided adsorption. 74, 75, 89, 92–94
EMA	exponential moving average filter. 46, 47
fps	frames per second. 42, 94, 96, 100
FSCV	fast-scan cyclic voltammogram. 62
IHP	inner Helmholtz plane. 12
MEA	microelectrode array. 43
OCP	open circuit potential. 11, 76
OHP	outer Helmholtz plane. 12
OSR	oversampling ratio. 26, 32, 43
OTA	operational transconductance amplifier. 24, 28
PBS	phosphate-buffered saline. 88, 90, 91
PEDOT	poly(3,4-ethylenedioxythiophene). 76, 81, 82, 84, 85
PPD	poly(phenylenediamine). 76, 83–85
RE	reference electrode. 11, 13, 14, 23, 26, 52, 53, 61, 62, 70

Acronyms

SDC	sigma-delta converter. 43
SHE	standard hydrogen electrode. 10
SNR	signal-to-noise ratio. 26, 32
SWV	square wave voltammetry. 63, 65, 87, 89
WE	working electrode. 11, 13, 14, 23, 52–54, 61, 62, 66, 70, 71

CURRICULUM VITAE

Jörg Rothe was born 1978 in Stuttgart, Germany. After passing the entry exam and studying for one year electrical engineering at ETH Zurich, in 2000 he co-founded a company for developing database driven websites. In 2002 he went back to ETH Zurich for studying electrical engineering, where he received his Master of Science degree in Electrical Engineering and Information Technology in 2008. During his master thesis he worked on "Single-Cell Impedance Spectroscopy" at the Bio Engineering Laboratory, ETH Zurich. This motivated him to pursue his PhD studies in 2008 in the same group.

The focus of his research has been on the design and application of CMOS-based microelectrode arrays for electrochemical measurements.